

THE EFFECT OF HEAT TREATMENT ON DISSOLUTION BEHAVIOR,  
PHYSICAL PROPERTIES AND ELECTRICAL PROPERTIES OF  
MAGNESIUM OXIDE THIN FILM IN MAGNETIC SENSORS



A Thesis Submitted in Partial Fulfillment of the Requirements for the  
Degree of Doctor of Philosophy in Material Engineering  
Suranaree University of Technology  
Academic Year 2021

ผลของการบำบัดด้วยความร้อนต่อพฤติกรรมการละลาย สมบัติทางกายภาพ  
และสมบัติทางไฟฟ้าของฟิล์มบางแมกนีเซียมออกไซด์ในอุปกรณ์ตรวจวัด  
ทางแม่เหล็ก



วิทยานิพนธ์นี้เป็นส่วนหนึ่งของการศึกษาตามหลักสูตรปริญญาวิศวกรรมศาสตรดุษฎีบัณฑิต  
สาขาวิชาวิศวกรรมวัสดุ  
มหาวิทยาลัยเทคโนโลยีสุรนารี  
ปีการศึกษา 2564

THE EFFECT OF HEAT TREATMENT ON DISSOLUTION BEHAVIOR,  
PHYSICAL PROPERTIES AND ELECTRICAL PROPERTIES OF MAGNESIUM  
OXIDE THIN FILM IN MAGNETIC SENSORS

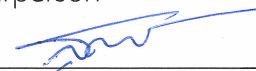
Suranaree University of Technology has approved this thesis submitted in partial fulfillment of the requirements for the Degree of Doctor of Philosophy.

Thesis Examining Committee



(Dr. Somchai Tancharakorn)

Chairperson



(Assoc. Prof. Dr. Soodket Pojprapai)

Member (Thesis Advisor)



(Dr. Worasom Kundhikanjana)

Member (Thesis Co-Advisor)



(Dr. Laddawan Supadee)

Member



(Dr. Pattanaphong Janphuang)

Member



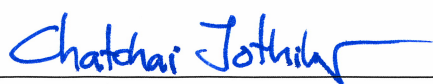
(Assoc. Prof. Dr. Sirirat Tubsungnoen Rattanachan)

Member



(Assoc. Prof. Dr. Sukanda Jiansirisomboon)

Member



(Assoc. Prof. Dr. Chatchai Jothityangkoon)

Vice Rector for Academic Affairs  
and Quality Assurance

(Assoc. Prof. Dr. Pornsiri Jongkol)

Dean of Institute of Engineering

มงคล กองทุ่งมน : ผลของการบำบัดด้วยความร้อนต่อพฤติกรรมการละลาย สมบัติทางกายภาพ และสมบัติทางไฟฟ้าของฟิล์มบางแมกนีเซียมออกไซด์ในอุปกรณ์ตรวจวัดทางแม่เหล็ก (THE EFFECT OF HEAT TREATMENT ON DISSOLUTION BEHAVIOR, PHYSICAL PROPERTIES AND ELECTRICAL PROPERTIES OF MAGNESIUM OXIDE THIN FILM IN MAGNETIC SENSORS) อาจารย์ที่ปรึกษา : รองศาสตราจารย์ ดร.สุตเชตต์ พจน์ประไพ, 100 หน้า.

คำสำคัญ: ฟิล์มบาง/แมกนีเซียมออกไซด์/พฤติกรรมการละลาย/สภาวะการบำบัดทางความร้อน/ฮาร์ดดิสก์ไดรฟ์ (HDD)

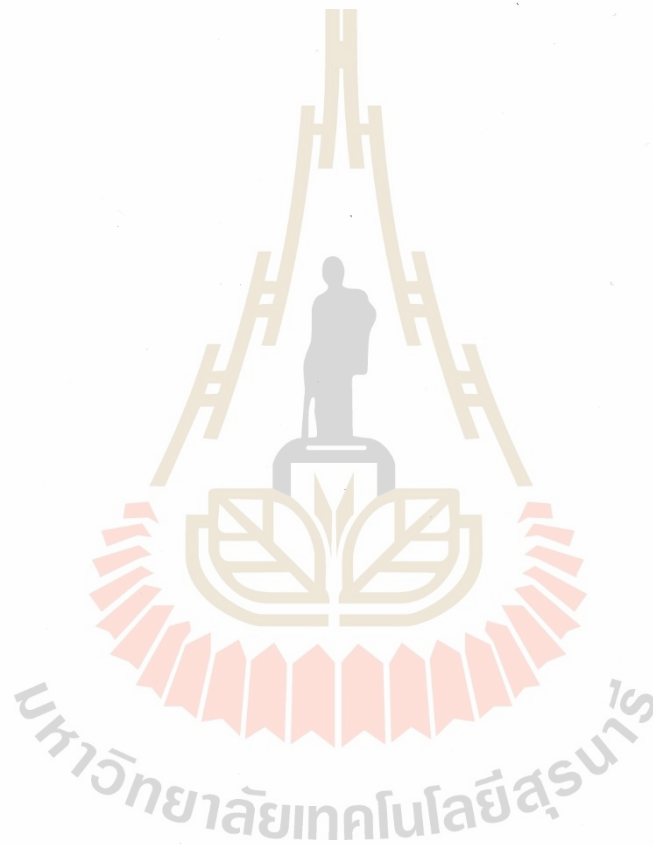
ชั้นฟิล์มแบบบางที่ทำจากแมกนีเซียมออกไซด์ (Magnesium oxide thin films) ในอุปกรณ์จัดเก็บข้อมูลแบบแม่เหล็ก (Magnetic data storage devices) ซึ่งถูกใช้ทำชั้นเป็นเกราะป้องกัน (Shield) สานามแม่เหล็กจากภายนอกและเป็นชั้นแบริเออร์ (Barrier) สำหรับโครงสร้างรอยต่อแบบทะลุผ่าน (Magnetic Tunneling Junction, MTJ) อีกด้วย แต่ในระหว่างกระบวนการผลิตนั้น ชั้นฟิล์มมักจะสัมผัสกับน้ำจากกระบวนการผลิต การสูญเสียเนื้อฟิล์มจากการละลายของชั้นฟิล์มส่งผลต่อประสิทธิภาพของอุปกรณ์เก็บข้อมูลแบบแม่เหล็ก ดังนั้น ความรู้ความเข้าใจในพฤติกรรมการละลายของฟิล์มบางแมกนีเซียมออกไซด์จึงมีความจำเป็นอย่างยิ่ง โดยในการศึกษานี้ได้ทำการศึกษาพฤติกรรมการละลายของชั้นฟิล์มแมกนีเซียมออกไซด์ด้วยด้วยเครื่องวัดการนำไฟฟ้าในสารละลาย (Electrical conductivity meter) ในช่วงเวลาการละลาย 2-15 ชั่วโมงที่อุณหภูมิห้อง จากผลการทดลอง พบว่าความเสียหายของฟิล์มที่ถูกละลายในน้ำจะเพิ่มขึ้นเมื่อระยะเวลาของการละลายเพิ่มขึ้น นอกจากนี้ค่าการนำไฟฟ้าที่วัดได้ตามช่วงเวลาของการละลายถูกนำมาใช้ในการสร้างเป็นโมเดลแสดงพฤติกรรมการละลายของชั้นฟิล์ม

ในระหว่างการผลิต ไม่เพียงแต่อาจพบความขึ้นบนพื้นผิวของฟิล์มซึ่งส่งผลให้เกิดการตกตะกอนของแมกนีเซียมไฮดรอกไซด์ ความเครียดตกค้างยังสามารถเกิดขึ้นได้อีกด้วย โดยทั่วไปแล้วผู้ผลิตฮาร์ดดิสก์จะใช้วิธีบำบัดด้วยความร้อน (Heat treatment) เพื่อกำจัดความขึ้นและความเครียดตกค้างจากกระบวนการผลิต ซึ่งการบำบัดด้วยความร้อนในกระบวนการผลิตที่อุณหภูมิและบรรยากาศของก๊าซต่าง ๆ อาจส่งผลต่อประสิทธิภาพของอุปกรณ์ได้ ในส่วนของการศึกษาผลของการบำบัดทางความร้อนต่อคุณสมบัติของแผ่นฟิล์มบางแมกนีเซียมออกไซด์ นั้น การทดลองจะทำภายใต้สภาวะก๊าซและอุณหภูมิที่แตกต่างกัน ซึ่งพบว่าสภาวะก๊าซและอุณหภูมิส่งผลต่อคุณสมบัติทางกายภาพ ทางเคมีและทางไฟฟ้าอย่างมีนัยสำคัญ

นอกจากนี้ ยังมีการศึกษาผลของก๊าซชนิดต่าง ๆ ในการปรับปรุงทางความร้อนต่อการเกิดไฮดรอกไซด์ ( $Mg(OH)_2$ ) ของฟิล์มบางที่ถูกเก็บในสภาวะที่มีการควบคุมความชื้น โดยอุณหภูมิการ

ปรับปรุงทางความร้อนถูกควบคุมที่ 450 องศาเซลเซียส จากนั้น จึงวิเคราะห์ความหนาผิว สัมฐาน  
วิทยาและการเกิดปฏิกิริยาไฮเดรชันในชั้นฟิล์มบางแมกนีเซียมออกไซด์ พบว่าความลึกของการ  
เกิดปฏิกิริยาไฮเดรชัน ความหนาผิว และความหนาของฟิล์มเปลี่ยนแปลงไปตามสภาวะของการ  
บำบัดด้วยความร้อน นอกจากนี้ หากมีความจำเป็นต้องเก็บชิ้นงานในตู้ควบคุมความชื้นเป็น  
เวลานานการใช้ก๊าซอาร์กอนในการอบอ่อนจะเหมาะสมที่สุด

ซึ่งผลการศึกษาในครั้งนี้อาจเป็นข้อมูลที่เป็นประโยชน์ในการหาสภาวะที่เหมาะสมที่ใช้ใน  
กระบวนการผลิตเซ็นเซอร์หัวอ่าน/เขียนฮาร์ดดิสก์ได้



สาขาวิชา วิศวกรรมเซรามิก

ปีการศึกษา 2564

ลายมือชื่อนักศึกษา

ลายมือชื่ออาจารย์ที่ปรึกษา

ลายมือชื่ออาจารย์ที่ปรึกษาร่วม

MONGKOL KONGTUNGMON : THE EFFECT OF HEAT TREATMENT ON DISSOLUTION BEHAVIOR, PHYSICAL PROPERTIES AND ELECTRICAL PROPERTIES OF MAGNESIUM OXIDE THIN FILM IN MAGNETIC SENSORS. THESIS ADVISOR : ASSOC. PROF. SOODKHET POJPRAPAI, Ph.D., 100 PP.

Keyword: thin film, MgO/dissolution behavior/heat treatment environment/hard disk drive (HDD)

Magnesium oxide (MgO) thin films are used as magnetic shields and barriers for magnetic tunneling junctions in magnetic data storage devices. During the fabrication process, these films could be exposed to water. The films can be lost by the dissolution process which can directly affect the performance of the magnetic data storage devices. Therefore, the dissolution behavior of MgO thin films in deionized water was investigated in this study. The dissolution of the material was determined using an electrical conductivity meter (EC) to measure the dissolved MgO over a period of 2–15 hours in deionized water at room temperature and a model describing the reaction rate is created based on electrical conductivity measurements of dissolved MgO as a function of time. The results showed the dissolution of the film left the damaged area with different surface structures depending on the time of dissolution.

During the manufacturing, not only moisture traps on the surface of the film can be found which result in magnesium hydroxide precipitation, residual stress can also occur. Generally, heat treatment is used by hard disk manufacturers to remove moisture and residual stress from the manufacturing process. The thermal treatment conditions under which thin films are manufactured, both in terms of temperature and gas atmosphere, may affect the device performance. Thus, the heat treatment condition with various treatment temperatures and gas atmospheres were examined in this study. The results showed that treatment temperatures and gas atmospheres directly affected the physical, chemical, and electrical properties of the films.

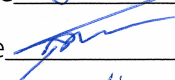
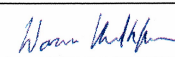
Moreover, the hydroxide ( $\text{Mg}(\text{OH})_2$ ) formation of the MgO thin films was studied by treating it with various gas atmospheres. The temperature of heat treatment was controlled at 450 °C. Then, the films were stored in controlled humidity. The surface roughness, morphology and hydration reaction of the films were investigated. The

results showed that a hydration reaction occurred deeply into the film layer. The depth of the hydration reaction and its surface roughness were based on heat treatment conditions. Moreover, if the film is stored for a long period of time in the humidity control cabinet, argon gas annealing is recommended.

The result of this study might be helpful to estimate the better optimization process of read/write sensor head of HDD production.



School of Ceramic Engineering  
Academic Year 2021

Student's Signature   
Advisor's Signature   
Co-Advisor's Signature 

## ACKNOWLEDGEMENT

There are many people whom I would like to thank for their contributions, both directly and indirectly. My deep gratitude goes first to my advisor Assoc. Prof. Dr. Soodkhet Pojprapai and co-advisor Dr. worasom kundhikanjana, who guided me through my graduation. Their guidance and advise carried me through all the stages of my research project.

I also would like to thank my committee members Dr. Somchai Tancharakorn, Assoc Prof. Dr. Sukanda Jiansirisomboon, Assoc. Prof. Dr. Sirirat Tubsungnoen Rattanachan, Dr. Pattanaphong Janphuang, and Dr. Laddawan Supadee for letting my defense be an interesting moment and for their brilliant comments and discussions.

In addition, I would like to express my appreciation to Western Digital (Thailand) Co., Ltd for financial support over the years of my Ph.D. program.

My completion of this project could not have been accomplished without the support of my lab colleges, as well as all my fellows, for their courteous help, cooperation, and good friendship during my research.

Finally, I extremely grateful to my family for their continuous support and understanding during my study period. The Ph.D. thesis would not have been finished or made feasible without the kindness and care of everyone who has stood by my side.

Mongkol Kongtungmon



# TABLE OF CONTENTS

	Page
ABSTRACT (THAI).....	I
ABSTRACT (ENGLISH).....	III
ACKNOWLEDGEMENT.....	V
TABLES OF CONTENT.....	VI
LIST OF TABLES.....	IX
LIST OF FIGURES.....	X
LIST OF ABBREVIATIONS.....	XIV
<b>CHAPTER</b>	
<b>1 INTRODUCTION.....</b>	<b>1</b>
1.1 Rationale and background.....	1
1.2 Research objectives.....	6
1.3 Hypotheses.....	6
1.4 Scope and limitation of the study.....	6
1.5 Thesis Contents.....	7
<b>2 LITERATURE REVIEW.....</b>	<b>12</b>
2.1 MgO in MTJs.....	12
2.1.1 MgO dissolution.....	15
2.1.2 Dissolution rate.....	18
2.2 MgO heat treatment.....	21
2.3 Characterization of MgO thin films.....	22
2.3.1 Electrical conductivity (EC).....	22
2.3.2 Ellipsometer.....	25
2.3.3 Atomic force microscopy (AFM).....	28
2.3.4 Focused ion beam (FIB).....	29
2.3.5 X-ray photoelectron spectroscopy (XPS).....	30

## TABLE OF CONTENTS (Continued)

	Page
<b>3 DISSOLUTION MECHANISM OF MGO THIN FILM SHIELDING LAYER IN TUNNELING MAGNETORESISTANCE HARD DISK DRIVE READ HEAD....</b>	<b>39</b>
3.1 Introduction.....	39
3.2 Experimental procedure.....	39
3.3 Results and discussions .....	41
3.3.1 AFM surface roughness .....	41
3.3.2 Electrical conductivity (EC).....	44
3.3.3 Ellipsometry.....	46
3.3.4 XPS chemical analysis .....	48
3.3.5 Dissolution mechanism of MgO.....	49
3.4 Conclusions .....	51
<b>4 EFFECT OF ANNEALING ATMOSPHERE ON PHYSICAL AND ELECTRICAL PROPERTIES OF MGO THIN FILM IN TUNNELING MAGNETORESISTANCE SENSOR .....</b>	<b>54</b>
4.1 Introductions.....	54
4.2 Experimental procedure.....	55
4.3 Results and discussions .....	57
4.3.1 AFM roughness.....	57
4.3.2 FIB-SEM analysis.....	58
4.3.3 Dielectric break down analysis .....	60
4.3.4 XPS analysis of MgO films .....	63
4.3.5 Grain expansion mechanism.....	65
4.4 Conclusions .....	66
<b>5 EFFECT OF ANNEALING ATMOSPHERE ON HYDRATION BEHAVIOR OF MGO THIN FILM IN TUNNELING MAGNETORESISTANCE SENSOR..</b>	<b>70</b>
5.1 Introductions.....	70
5.2 Experimental procedure.....	70

## TABLE OF CONTENTS (Continued)

	Page
5.3 Results and discussions .....	72
5.3.1 Microstructure analysis by SEM imaging .....	72
5.3.2 Surface roughness analysis by AFM.....	73
5.3.3 Chemical composition analysis by XPS.....	74
5.3.4 Mechanism of MgO thin films hydration .....	79
5.4 Conclusions .....	80
<b>6 CONCLUSION AND FUTURE PERSPECTIVES.....</b>	<b>83</b>
6.1 General Conclusions.....	83
6.2 Recommendations for Future Work.....	85
APPENDIX.....	86
BIOGRAPHY.....	100

## LIST OF TABLES

Table	Page
2.1	Advantages and disadvantages of SE.....27
3.1	Comparison of MgO mass loss from the experimental AAS results and with dissolution model calculations for various time scales.....47



## LIST OF FIGURES

Figure	Page
1.1 (a) typical hard disk drive components (b) Schematic illustration of the HDD slider (c) cross-section of a typical thin-film multilayer stack used in a hard disk drive reader head.....	2
1.2 Schematic diagram of the TMR effect in a MTJs reader head (Xuyang et al., 2019).....	3
2.1 MTJ read head in an HDD (Zhu & Park, 2006).....	14
2.2 TMR ratios over a few past decades for amorphous AlOx-based MTJs (blue triangles) and crystalline MgO-based MTJs (red circles) (Zhu & Park, 2006).....	15
2.3 (a) SEM micrograph (b) AFM topography of MgO thin film surface after being exposed to DI water 6 hours at room temperature.....	16
2.4 Surface morphology of the 5-day-hydrated MgO (a) (001) Sputtered thin films (b) (111) Sputtered thin films (Lee et al., 2003). ....	18
2.5 Mg(OH) <sub>2</sub> concentration as a function of time at various temperatures. (Birchal et al., 2001).....	19
2.6 MgO dissolution rate obtained by measuring conductivity of water as a function of time. Plateau after long-term exposure indicates saturation. The inset shows a needle-like crystal on the surface, which is Mg(OH) <sub>2</sub> precipitation (Fruhirth et al., 1985).....	20
2.7 Electrolytic conduction of MgO in aqueous solution.....	23
2.8 Simplified conductivity meter diagram.....	25
2.9 The ellipsometry measurement uses linearly polarized light with both p and s components. As a result of contact with the sample, elliptically polarized light is produced (Tompkins & Hilfiker, 2015). ....	26

## LIST OF FIGURES (Continued)

Figure	Page
2.10	A schematic setup of a rotating analyzer ellipsometer (RAE) (Tompkins & Hilfiker, 2015). .....27
2.11	Various AFM modes have been developed, including contact mode, noncontact mode, and tapping mode (Asmatulu & Khan, 2019).....28
2.12	A dual-beam FIB–SEM instrument is represented in a schematic diagram. The interaction between the electron and ion beam samples is shown in greater detail inside this image (Volkert & Minor, 2007).....29
2.13	Schematic drawing of an XPS instrument (Watts & Wolstenholme, 2019).....31
2.14	XPS spectra MgO survey scan (Peng et al., 2020) .....31
2.15	schematic of XPS depth profiling (Taketa et al., 2020).....32
3.1	Schematic view (left) and photograph (right) of the custom-built test cell.....40
3.2	(a)–(e) AFM images at $5 \times 5 \mu\text{m}$ scan size and (f)–(j) SEM images at $\times 50000$ magnification on MgO dissolved surfaces in deionized water for 2, 4, 6, 10, and 15 hours respectively.....43
3.3	Film roughness ( $R_a$ ) and $\text{Mg}(\text{OH})_2$ cluster size on MgO thin film as a function of dissolution time in deionized water derived from AFM images of the surface.....44
3.4	Electrical conductivity (EC) and Mg concentration as a function of dissolution time. Red dashed line is the curve fit to the experimental data. The inset depicts the linear relationship between Mg concentration and EC.....45
3.5	(a) Thickness profile of the MgO thin film after dissolution, as measured by ellipsometry. (b-d) SEM-FIB cross section of the film (b) outside the exposed area, (c) inside the exposed area (near O-ring), and (d) at the center of the exposed area.....48

## LIST OF FIGURES (Continued)

Figure		Page
3.6	(a,b) SEM micrographs and (c,d) O 1s XPS spectra of as-received MgO (a and c, respectively), and MgO immersed in deionized water for 10 hours (b and d, respectively).....	49
3.7	The mechanism of MgO dissolution (a) surface is protonated by H <sup>+</sup> ions from water (H <sub>2</sub> O), (b) OH <sup>-</sup> negative ions absorbed on the surface to form MgOH <sup>+</sup> •OH <sup>-</sup> , (c) dissolution of the MgO film into Mg <sup>2+</sup> and OH <sup>-</sup> ions, and (d) magnesium hydroxide (MgOH) <sub>2</sub> cluster.....	50
4.1	(a) schematic representation of custom-built in-house annealing setup and (b) actual image of the annealing gas chamber.....	56
4.2	a schematic diagram of the MgO thin film prepared for dielectric breakdown measurement.....	57
4.3	surface roughness of MgO films at different gas atmospheric temperatures. Figures (a-c) depict the Ar gas annealing, figures (d-f) depict the N <sub>2</sub> gas annealing, and figures (g-i) depict the normal air annealing. Here annealing temperatures are 250, 350, 450°C.....	58
4.4	SEM-FIB cross-section of (a) as-received, (b-d) argon, (e-g) nitrogen, and (h-j) normal air 250-450 °C samples, respectively.....	60
4.5	(a-c) I-V curve of the Ar, N <sub>2</sub> and normal air annealed MgO films. Current jump indicates the dielectric breakdown voltage.....	62
4.6	(a) Schematic drawing of MgO layer structure (b) XPS depth profile of as-received MgO/Ru/Si film to determine the atomic concentration of Mg as a function of film depth.....	63
4.7	Ion depth profile of MgO thin film with different annealing environments. High-resolution peak intensity of Mg2p, O1s, and Ru3d as a function of etching time for the fresh sample, N <sub>2</sub> and Ar. Rising of the Ru peak intensity is used to calculate the etch.....	64
4.8	Mechanism of gas annealed MgO thin films grain expansion.....	66

## LIST OF FIGURES (Continued)

Figure	Page
5.1 shows the annealing set-up of MgO films. (a) Schematic drawing and (b) actual image of the custom-made gas annealing chamber.....	72
5.2 SEM-FIB cross-section of (a) as-received, (b) argon 450 °C, (c) nitrogen 450 °C and (d) air 450 °C annealed samples, respectively.....	73
5.3 AFM surface images of (a)-(c) the Ar, N <sub>2</sub> and Air 450 °C annealed MgO films after being hydrated (stored in a 50% relative humidity control cabinet for 30 days). The inset numbers are the roughness of the films.....	74
5.4 comparative O 1s XPS spectra after 2 minutes [(a) – (d)] and 10 minutes [(e) – (h)] of sputter time of un-hydrated (as-received) MgO thin film and hydrated MgO films that were stored in a 50% relative humidity-controlled cabinet for 30 days.....	76
5.5 XPS sputter time of MgO thin films annealed at different gas environments.....	77
5.6 hydration reaction depth profile of MgO thin films annealed at different environments.....	78
5.7 Mechanism of gas annealed MgO thin films hydration.....	80



## LIST OF ABBREVIATIONS

AAS	=	atomic absorption spectrometer
AFM	=	atomic force microscope
AMR	=	anisotropic magneto resistive
Ar	=	argon
BE	=	binding energy
CoFeB	=	cobalt-iron-boron
DI	=	deionized
EC	=	Electrical conductivity meter
FIB-SEM	=	focused ion beam scanning electron microscopy
GMR	=	giant magnetoresistance
HDD	=	Hard disk drives
IrMn	=	Iridium-manganese
Mg(OH) <sub>2</sub>	=	magnesium hydroxide
MgO	=	Magnesium oxide
MR	=	magnetoresistance
MTJ	=	magnetic tunneling junctions
N <sub>2</sub>	=	nitrogen
PtMn	=	Manganese Platinum Alloy
RH	=	relative humidity
RMS	=	root mean square
Ru	=	ruthenium
SE	=	spectrometry ellipsometer
SEM	=	scanning electron microscopy
TMR	=	Tunneling magnetoresistance
XPS	=	X-ray photoelectron spectroscopy
a-C:H	=	Hydrogenated amorphous carbon
BE	=	Binding energy

## LIST OF ABBREVIATIONS (Continued)

$h\nu$	=	Photon
KE	=	Kinetic energy
kV	=	Kilo voltage



# CHAPTER 1

## INTRODUCTION

### 1.1 Rationale and Background

Hard disk drives (HDDs) are magnetic storage devices that use high-speed rotating disks (platters) coated with magnetic materials to store and retrieve digital information. Above and below each platter are magnetic read/write heads, which are positioned to control their movement on the disk surface as well as provide access to the appropriate data track (Figure 1.1 (a)). The read and write heads are used to detect and modify the magnetization of a ferromagnetic thin film on a disk that serves as a representation of binary data bits, as shown in Figure 1.1 (b).

Many years ago, anisotropic magnetoresistive (AMR) heads were the first generation of magnetoresistive reader heads. The working principle of AMR is that the electrical resistance of a ferromagnetic material changes in response to the direction of magnetization caused by an applied magnetic field relative to the direction of current flow. When a ferromagnetic material is magnetized in the same direction as the current flow, the resistance decreases. On the other hand, the resistance increases when magnetized perpendicular to the direction of current flow. Therefore, magnetoresistance (MR) represents the change in resistance corresponding to an applied electric field. In a giant magnetoresistance (GMR) element, which consists of a nonmagnetic metal (Cu, for example) sandwiched between two ferromagnetic layers, electrons flow through metal conduction. The MR ratios of typical AMR and GMR elements are around 3% and 12%, respectively (Jungwirth et al., 2013; Yuasa & Djayaprawira, 2007). Electron flow happens through the quantum mechanical tunnel effect in a TMR element.

When the pin layer and the free layer are antiparallel, a TMR element exhibits an extreme characteristic in which electrons "cannot move almost at all," in contrast to the characteristics of a GMR element in which "electron movement is difficult." This

results in a TMR element having an extraordinarily high MR ratio; this is also why TMR elements are used as highly sensitive reading elements in modern hard disk drives. Tunneling magnetoresistance (TMR) is a specific MR effect which is applied to a high-density disk drive (HDD) read heads and is the primary focus of this research. In the TMR reader, two ferromagnetic layers (a free layer and a pinned layer) are separated by an insulator. Typically, the antiferromagnetic layer is composed of IrMn, PtMn, or FeMn, while the free and pinned layers are composed of CoFeB or CoFe, and the insulation layer is composed of  $\text{Al}_2\text{O}_3$  or  $\text{MgO}$ , as illustrated in Figure 1.1 (c).

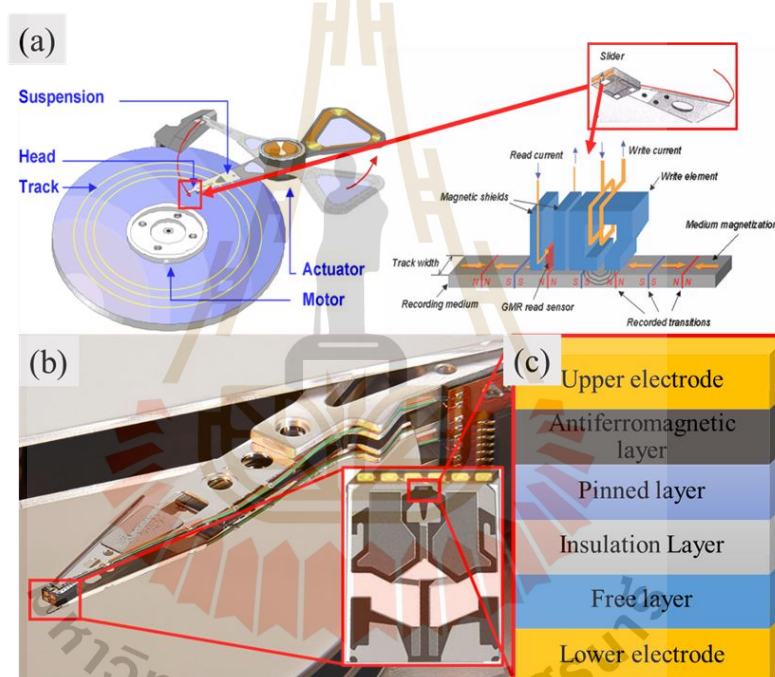


**Figure 1.1** (a) typical hard disk drive components (b) Schematic illustration of the HDD slider (c) cross-section of a typical thin-film multilayer stack used in a hard disk drive reader head

In magnetic sensor read heads, magnetic tunneling junctions (MTJs) are considered the heart of TMR. The MTJ operates on the principle of creating a high and low resistance state based on the magnetic moment's orientation. The structure of the MTJ includes (1) a pinned magnetization layer; (2) a free rotating magnetization layer;

and (3) an insulation or a barrier layer. The term magnetoresistance is important because it represents the magnitude of the differential between the high and low resistance states of a particular device. These states are used as logic states for computer memory, allowing a clear distinction to be made between the "ON" and "OFF" states of the computer memory. When the two magnetizations are parallel, the resistance of the MTJ is minimal; when they are anti-parallel, the resistance of the MTJ is maximal. This results in the TMR read head's output having a distinct character, such as "yes or no" or "1 or 0," which correlates to digital information when this occurs (Figure 1.2)

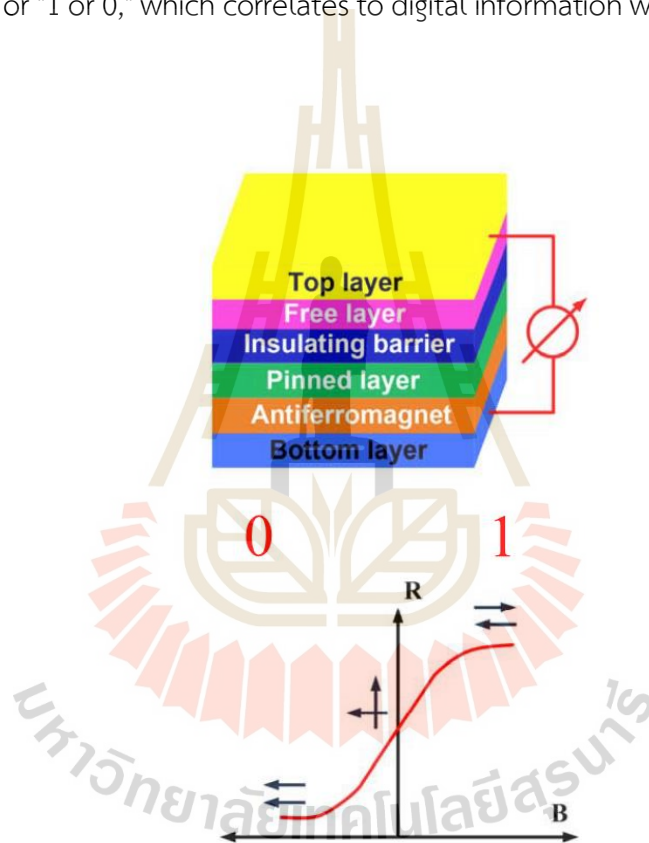


**Figure 1.2** Schematic diagram of the TMR effect in a MTJs reader head (Xuyang et al., 2019).

Aluminum oxide ( $\text{Al}_2\text{O}_3$ ) was used as a tunnel barrier in early MTJ devices due to its suitability for thin forming ( $\sim 10 \text{ \AA}$ ),  $\text{Al}_2\text{O}_3$ . Dexin et al (Dexin et al., 2004) reported that the CoFeB/ $\text{AlOx}$ /CoFeB junction exhibited MR values of up to 70%. Regrettably, oxidation of the Al layer frequently results in a significant decrease in the TMR ratio.

MgO is a typical rock salt structure that is strongly ionic insulating with a band gap of around 7.77 eV (Roessler & Walker, 1967). MgO is an excellent insulator material because of its high dielectric constant (9.8) and high breakdown voltage (Browder et al., 1991). Additionally, MgO may be used as a template for ferroelectric materials, where the ferroelectric property enhances the capacitance value (Chen et al., 1989; Lide, 2004). In TMR sensors, magnesium oxide thin film insulators were used as a magnetic shielding/insulator layer. The discovery and development by HDD manufacturers found that magnesium oxide thin film insulators could improve signal quality while additionally reducing the side reading effect of HDD read heads (Haginoya et al., 2004; Zheng et al., 2006).

The critical problem facing MgO in a read/write head is the cleaning and polishing process, which involves in contacting with water. MgO reacts quickly and easily with water, including ambient moisture (Carrasco et al., 2010; Holt et al., 1997; Jones et al., 1984), resulting in irreversible hydration and the precipitation of magnesium hydroxide ( $\text{Mg(OH)}_2$ ) (Amaral et al., 2011). Dissolution of a magnesium oxide thin film results in material loss and the change of the film properties, which can finally affect device performance. The dissolution rate of magnesium oxide thin films is typically determined by the amount of film dissolved in the solution. The hydration process can cause film swelling and cracking due to the density difference between MgO ( $3.5 \text{ g/cm}^3$ ) and  $\text{Mg(OH)}_2$  ( $2.4 \text{ g/cm}^3$ ), which precipitates in proportion to the amount of water/moisture available and the duration of exposure time. The concentration of  $\text{Mg(OH)}_2$  is proportional to the amount of magnesium oxide dissolved in water. Various recent experiments have investigated the MgO dissolution mechanism and rate as a function of pH (Fruhirth et al., 1985), crystal orientations (Geysersmans et al., 2009; Holt et al., 1997), temperature (Amaral et al., 2010), and kinetic mechanisms (Blaha, 1995b; Kato et al., 1996; L. & N., 1969; Mejias et al., 1999)

Additionally, mechanical forces also cause the development of residual stress in a thin layer. As a result, hard disk manufacturers have introduced a pre-heating technique to remove moisture and decrease residual stress from the film. According to some research, thermal annealing enhances the dielectric strength, porosity, and defects of the material and decreases the leakage current (Cheng et al., 2016; Furukawa

et al., 1997; Jo & Park, 1998; Keiji et al., 2010; Tanigaki et al., 1988). Thermal annealing (also known as calcination) of magnesium oxide films can eliminate surface absorbents such as water, hydroxyl (OH<sup>-</sup>), and carbonyl (CO<sup>-</sup>) groups (Kumari et al., 2009; Park et al., 2006; Peng & Barteau, 1990; Rheinheimer et al., 2017). The effect of annealing magnesium oxide (MgO) films used in magnetic tunnel junctions (MTJs) has become an attractive topic in recent years. It has been observed that annealing can improve the crystallinity and structure at the MgO/CoFeB interface, therefore enhancing the magnetoresistance (Hayakawa et al., 2006; Ikeda et al., 2008; Park et al., 2006).

The annealing temperature, annealing environment, and relative humidity maintained in the processing room seem to have a significant effect on the film's properties (chemical and structural stability, density, porosity, and roughness). In the HDD manufacturing process, the production room regulates the humidity at approximately 50% RH, which could initiate the hydration reaction with MgO thin films. The physical and chemical properties of the magnesium oxide thin film might affect the magnetic sensitivity of a read/write sensor head (Balcells et al., 2010). However, most of these reports were performed on bulk MgO specimens (Amaral et al., 2011; Blaha, 1995a, 1995b; Dimitrios et al., 1999; Kato et al., 1996; L. & N., 1969; Santamaria et al., 2007). Even though these thin films are very important in HDD manufacturing, the dissolution mechanism, and the effect of dissolution behavior of the MgO thin film shielding layer of TMR devices are not yet well comprehensible. In this study, the author investigated the kinetics of MgO hydration with different exposure times to deionized water (DI water) at room temperature. To study the combined effect of both atmospheric annealing and humidity control reaction effects, the MgO films were annealed at different gas atmospheres and temperatures (250-450 °C) and stored in a 50% humidity control chamber for 30 days. The changes in surface roughness and surface morphology will be discussed in the framework of the atomic force microscope (AFM), X-ray photoelectron spectroscopy (XPS), and focused ion beam scanning electron microscopy (FIB-SEM). In this thesis, a kinetic model is proposed, and its validity is verified using electrical conductivity (EC) measurements on MgO thin films exposed to DI water for varied periods of time. The mathematical model is used to

predict material loss during the production process and might be helpful to estimate the better optimization process of read/write sensor head of HDD production.

## 1.2 Research objectives

- 1) To determine the dissolution behavior of MgO in DI water by investigating:
  - a. The material loss during dissolved in DI water.
  - b. The remaining film thickness.
  - c. The roughness as a function of time.
- 2) To determine the effect of annealing temperature and gas environment on MgO electrical, chemical, and physical properties including electric breakdown, XPS sputter rate and surface morphology.

## 1.3 Hypotheses

- 1) The dissolution behavior of the MgO thin film can be verified using an EC meter in solution comparable to a chemical instrument, and the dissolution rate equation as a function of time can also be generated directly from the thin film's dissolution behavior.
- 2) After exposure to water, MgO thin films may exhibit the changes in physical and chemical properties such as thickness and roughness, as well as a hydroxide precipitation, which may result in film degradation.
- 3) The heat treatment conditions including annealing gasses and temperatures will affect MgO thin film properties such as structure, dielectric breakdown, chemical properties, and film roughness.

## 1.4 Scope and limitation of the study

The purpose of this research was to design a series of experiments to investigate the dissolution behavior and material loss effects of MgO thin films. The dissolution of the MgO films was determined using an EC meter over a period of 2–15 hours in DI water at room temperature. The author decided not to investigate the dissolution behavior as a function of temperature because the author aimed to simulate an actual manufacturing environment in which the production room temperature was already



regulated. In this investigation, MgO thin film heat treatment experiment was conducted at temperatures of 250, 350, and 450 °C in an environment of argon, nitrogen, and normal gasses inside a custom-built double-heating chamber. The furnace heating system regulated the temperature within the furnace.

## 1.5 Thesis Contents

This thesis is divided into six chapters.

**Chapter 1** includes problems and rationale, research objectives, scope of work, and research methodology.

**Chapter 2** presents the literature review including theoretical backgrounds of tunneling magnetoresistance (TMR) in the hard disk drives. Additionally, this chapter has discussed the dissolution and heat treatment effects of MgO thin films and the principles underlying the characterization techniques used in this study.

**Chapter 3** describes experiments on the dissolution mechanism of a magnesium oxide thin film shielding layer in a tunneling magnetoresistance hard disk drive read head. The kinetics of magnesium oxide hydration were investigated at room temperature using different exposure times to the deionized water (DI water). Atomic force microscopy (AFM) and scanning electron microscopy (SEM) were used to study the changes in surface roughness and morphology. The kinetic model of magnesium oxide hydration was proposed and validated by using electrical conductivity (EC) measurements on samples exposed to DI water for various periods of time.

**Chapter 4** reports the effect of the annealing atmosphere on the film thickness and surface roughness of the MgO thin film. The XPS depth profile technique was employed to determine the chemical composition and sputter rate of the film.

**Chapter 5** presents the effects of annealing atmosphere on hydration behavior of MgO thin film to study the combined effects of both atmospheric annealing and humidity control reaction. The XPS depth profile technique was used to determine the depth to which hydroxide penetrates into the film layer.

**Chapter 6** provides discussions and conclusions.

## 1.6 References

- Amaral, L. F., Oliveira, I. R., Bonadia, P., Salomão, R., & Pandolfelli, V. C. (2011). Chelants to inhibit magnesia (MgO) hydration. *Ceramics International*, 37(5), 1537-1542. doi:10.1016/j.ceramint.2011.01.030
- Amaral, L. F., Oliveira, I. R., Salomão, R., Frollini, E., & Pandolfelli, V. C. (2010). Temperature and common-ion effect on magnesium oxide (MgO) hydration. *Ceramics International*, 36(3), 1047-1054. doi:10.1016/j.ceramint.2009.12.009
- Balcells, L., Beltrán, J. I., Martínez-Boubeta, C., Konstantinović, Z., Arbiol, J., Martínez, B., T., D., H., O., F., M., J., C., & D., F. (2010). Aging of magnetic properties in MgO films. *Applied Physics Letters*, 97(25), 252503. doi:10.1063/1.3527963
- Blahá, J. (1995a). Kinetics of hydration of magnesium oxide in aqueous suspension. *Ceramics- Silikaty*, 39(2), 45-51.
- Blahá, J. (1995b). Kinetics of hydration of magnesium oxide in aqueous suspension. *Ceramics- Silikaty*, 39(2), 45-51.
- Browder, J., Ballard, S., & Klocek, P. (1991). Handbook of infrared optical materials. *Handbook of Infrared Optical Materials*. New York: Marcel Dekker.
- Carrasco, E., Brown, M. A., Sterrer, M., Freund, H.-J., Kwapien, K., Sierka, M., & Sauer, J. (2010). Thickness-Dependent Hydroxylation of MgO(001) Thin Films. *The Journal of Physical Chemistry C*, 114(42), 18207-18214. doi:10.1021/jp105294e
- Chen, C., Ryder Jr, D. F., & Spurgeon, W. A. (1989). Synthesis and microstructure of highly oriented lead titanate thin films prepared by a sol-gel method. *Journal of the American Ceramic Society*, 72(8), 1495-1498.
- Cheng, Y.-L., Kao, K.-C., Chen, G.-S., Fang, J.-S., Sun, C.-R., & Lee, W.-H. (2016). Effect of annealing temperature on electrical and reliability characteristics of HfO<sub>2</sub>/porous low-k dielectric stacks. *Microelectronic Engineering*, 162 (Supplement C), 34-39. doi:https://doi.org/10.1016/j.mee.2016.04.013.
- Dexin, W., Nordman, C., Daughton, J. M., Zhenghong, Q., & Fink, J. (2004). 70% TMR at room temperature for SDT sandwich junctions with CoFeB as free and reference Layers. *IEEE Transactions on Magnetics*, 40(4), 2269-2271. doi:10.1109/TMAG.2004.830219

- Dimitrios, F., Nikolaos, K., Nymphodora, P., & Katerina, A. (1999). On the kinetics of magnesia hydration in magnesium acetate solutions. *Journal of Chemical Technology & Biotechnology*, 74(4), 322-328. doi:10.1002/(SICI)1097-4660(199904)74:4<322::AID-JCTB35>3.0.CO;2-L
- Fruhwith, O., Herzog, G. W., Hollerer, I., & Rachetti, A. (1985). Dissolution and hydration kinetics of MgO. *Surface Technology*, 24(3), 301-317. doi:10.1016/0376-4583(85)90080-9
- Furukawa, T., Yuuki, A., & Ono, K. (1997). Recovery of time-dependent dielectric breakdown lifetime of thin oxide films by thermal annealing. *Journal of Applied Physics*, 82(7), 3462-3468. doi:10.1063/1.365662
- Geysersmans, P., Finocchi, F., Goniakowski, J., Hacquart, R., & Jupille, J. (2009). Combination of (100), (110) and (111) facets in MgO crystals shapes from dry to wet environment. *Physical Chemistry Chemical Physics*, 11(13), 2228-2233. doi:10.1039/B812376D
- Haginoya, C., Hatatani, M., Meguro, K., Ishikawa, C., Yoshida, N., Kusakawa, K., & Watanabe, K. (2004). Side-shielded tunneling magnetoresistive read head for high-density recording. *IEEE Transactions on Magnetics*, 40(4), 2221-2223. doi:10.1109/TMAG.2004.829157
- Hayakawa, J., Ikeda, S., Lee, Y. M., Matsukura, F., & Ohno, H. (2006). Effect of high annealing temperature on giant tunnel magnetoresistance ratio of CoFeB/MgO/CoFeB magnetic tunnel junctions. *Applied Physics Letters*, 89(23), 232510. doi:10.1063/1.2402904
- Holt, S. A., Jones, C. F., Watson, G. S., Crossley, A., Johnston, C., Sofield, C. J., & Myhra, S. (1997). Surface modification of MgO substrates from aqueous exposure: an atomic force microscopy study. *Thin Solid Films*, 292(1), 96-102. doi:10.1016/S0040-6090(96)08955-9
- Ikeda, S., Hayakawa, J., Ashizawa, Y., Lee, Y. M., Miura, K., Hasegawa, H., Tsunoda, M., Matsukura, F., & Ohno, H. (2008). Tunnel Magnetoresistance of 604% at 300 K by Suppression of Ta Diffusion in CoFeB/MgO/CoFeB Pseudo-Spin-Valves Annealed at High Temperature (Vol. 93).

- Jo, M.-H., & Park, H.-H. (1998). Leakage current and dielectric breakdown behavior in annealed SiO<sub>2</sub> aerogel films. *Applied Physics Letters*, 72(11), 1391-1393. doi:10.1063/1.121065
- Jones, C. F., Reeve, R. A., Rigg, R., Segall, R. L., Smart, R. S. C., & Turner, P. S. (1984). Surface area and the mechanism of hydroxylation of ionic oxide surfaces. *Journal of the Chemical Society, Faraday Transactions 1: Physical Chemistry in Condensed Phases*, 80(10), 2609-2617. doi:10.1039/F19848002609
- Jungwirth, T., Wunderlich, J., Novak, V., Olejnik, K., Gallagher, B., Campion, R., Edmonds, K., Rushforth, A., Ferguson, A., & Nemeč, P. (2013). Spin-dependent phenomena and device concepts explored in (Ga,Mn) As. *Reviews of Modern Physics*, 86. doi:10.1103/RevModPhys.86.855
- Kato, Y., Yamashita, N., Kobayashi, K., & Yoshizawa, Y. (1996). Kinetic study of the hydration of magnesium oxide for a chemical heat pump. *Applied Thermal Engineering*, 16(11), 853-862. doi:10.1016/1359-4311(96)00009-9
- Keiji, H., Makoto, N., Tomomasa, U., Hisanori, A., Sumio, I., Yoshiaki, A., Hiroaki, Y., & Akihiro, N. (2010). Effect of Self-Heating on Time-Dependent Dielectric Breakdown in Ultrathin MgO Magnetic Tunnel Junctions for Spin Torque Transfer Switching Magnetic Random Access Memory. *Japanese Journal of Applied Physics*, 49(4S), 04DD15. Retrieved from <http://stacks.iop.org/1347-4065/49/i=4S/a=04DD15>
- Kumari, L., Li, W. Z., Vannoy, C. H., Leblanc, R. M., & Wang, D. Z. (2009). Synthesis, characterization and optical properties of Mg(OH)<sub>2</sub> micro-/nanostructure and its conversion to MgO. *Ceramics International*, 35(8), 3355-3364. doi:<https://doi.org/10.1016/j.ceramint.2009.05.035>
- L., S. G., & N., B. N. (1969). The kinetics and mechanism of the hydration of magnesium oxide in a batch reactor. *The Canadian Journal of Chemical Engineering*, 47(6), 508-513. doi:doi:10.1002/cjce.5450470602
- Lide, D. R. (2004). *CRC handbook of chemistry and physics* (Vol. 85): CRC press.
- Mejias, J. A., Berry, A. J., Refson, K., & Fraser, D. G. (1999). The kinetics and mechanism of MgO dissolution. *Chemical Physics Letters*, 314(5-6), 558-563. doi:10.1016/S0009-2614(99)00909-4

- Park, C., Zhu, J.-G., Moneck, M. T., Peng, Y., & Laughlin, D. E. (2006). Annealing effects on structural and transport properties of rf-sputtered CoFeB/MgO/CoFeB magnetic tunnel junctions. *Journal of Applied Physics*, 99(8), 08A901. doi:10.1063/1.2165141
- Peng, X. D., & Barteau, M. A. (1990). Dehydration of carboxylic acids on the MgO(100) surface. *Catalysis Letters*, 7(5), 395-402. doi:10.1007/bf00764930
- Rheinheimer, V., Unluer, C., Liu, J., Ruan, S., Pan, J., & Monteiro, P. (2017). XPS Study on the Stability and Transformation of Hydrate and Carbonate Phases within MgO Systems. *Materials*, 10(1), 75. Retrieved from <http://www.mdpi.com/1996-1944/10/1/75>
- Roessler, D. M., & Walker, W. C. (1967). Electronic Spectrum and Ultraviolet Optical Properties of Crystalline MgO. *Physical Review*, 159(3), 733-738. doi:10.1103/PhysRev.159.733
- Santamaria, M., di quarto, F., Zanna, S., & Marcus, P. (2007). *Initial surface film on magnesium metal: A characterization by X-ray photoelectron spectroscopy (XPS) and photocurrent spectroscopy (PCS)* (Vol. 53).
- Tanigaki, Y., Moribe, S., & Itagaki, T. (1988, 13-14 June 1988). *The effects of annealing ambients on dielectric strength of gate oxides with tungsten polycide gate*. Paper presented at the 1988. Proceedings., Fifth International IEEE VLSI Multilevel Interconnection Conference.
- Xuyang, L., Lam, K. H., Zhu, P. K., Zheng, C., Li, X., Du, Y., Chunhua, L., & Pong, P. (2019). Overview of Spintronic Sensors With Internet of Things for Smart Living. *IEEE Transactions on Magnetics*, PP. doi:10.1109/TMAG.2019.2927457
- Yuasa, S., & Djayaprawira, D. D. (2007). Giant tunnel magnetoresistance in magnetic tunnel junctions with a crystalline MgO(0 0 1) barrier. *Journal of Physics D: Applied Physics*, 40(21), R337. Retrieved from <http://stacks.iop.org/0022-3727/40/i=21/a=R01>
- Zheng, Y. K., Han, G. C., Li, K. B., Guo, Z. B., Qiu, J. J., Tan, S. G., Liu, Z. Y., Liu, B., & Wu, Y. H. (2006). Side Shielded TMR Reader With Track-Width-Reduction Scheme. *IEEE Transactions on Magnetics*, 42(10), 2303-2305. doi:10.1109/TMAG.2006.880463

## CHAPTER 2

### LITERATURE REVIEW

This chapter presents related research works and focuses on the dissolution and heat treatment effects of MgO thin films, as well as the principles underlying the characterization techniques used in this study. This chapter is divided into the following sections. Section 2.1 describes hard disk drives and their key components, including MTJs hard disk reader heads as well as the MgO thin film in MTJs hard disk reader heads. Section 2.1.1 describes the reaction that occurs when magnesium oxide (MgO) is exposed to moisture or water, as well as the variety of chemical reactions that take place when magnesium oxide is dissolved in water. Section 2.1.2 explains the method to measure the dissolution rate of MgO in water, including several experimental techniques for measuring the dissolution rate as a function of time. The internal factors of the thermal treatment process that influences the properties of magnesium oxide thin films are discussed in Section 2.2. The followings are the principles of film characterization instruments, which are covered in Section 2.3: Instruments used in this thesis include an electrical conductivity meter (EC), spectrometry ellipsometer (SE), focused Ion Beam Scanning Electron Microscopes (SEM-FIB), atomic force microscope (AFM), and X-ray photoelectron spectroscopy (XPS).

#### 2.1 MgO in MTJs

Hard disk drives (HDDs) are currently the most common type of storage media, and they are widely used due to their high capacity-to-cost ratio. They are made up of high-speed rotating disks (platters) coated with magnetic materials. They are mounted on a moving actuator arm that reads and writes data to the platter surfaces. The read and write heads are used to detect and modify the magnetization of a thin film of ferromagnetic materials on a disk, which is used to represent binary data bits. Anisotropic magneto resistive (AMR) heads were introduced many decades ago and were the first generation of magneto resistive heads that operated on the principle of

the resistance change of a ferromagnetic material based on the magnetization direction of an applied magnetic field relative to the direction of current flow. When a ferromagnetic material is magnetized in the same direction as the current flow, the resistance decreases. However, it exhibits an increase in resistance when magnetized perpendicular to the direction of current flow. Magnetoresistance (MR) is the term most commonly used to define this resistance change. It is typically calculated as a percentage. (see Equation (2.1)).

$$MR\% = \frac{R_H - R_L}{R_L} \times 100 \quad (2.1)$$

Where  $R_H$  and  $R_L$  are the electrical resistivities when current and magnetization are parallel and perpendicular, respectively.

Tunneling magnetoresistance (TMR) is the current stage of HDD read head development and the primary focus of this research. The TMR reader used in hard disk drives consists of two ferromagnetic layers (free layer and pin layer) separated by an insulator. Typically, the antiferromagnetic layer is made of IrMn, PtMn, or FeMn, while the free layer and pinned layer are made of CoFeB or CoFe, and the insulation layer is made of  $Al_2O_3$  or MgO, as shown in Figure 2.1.

Magnetic tunneling junctions (MTJs) are at the heart of TMR. The MTJ operates on the principle of generating a high and a low resistance state dependent on the magnetic moment's orientation. The structure of the MTJ includes one ferromagnetic layer with pinned magnetization as a reference, while the other ferromagnetic layer is free to rotate in the presence of an external magnetic field. When the two magnetizations are parallel, the MTJ's resistance is minimal; in anti-parallel, the resistance is maximal. When this occurs, the TMR read head's output has a particular character, such as "yes or no" or "1 or 0," which corresponds to digital information.

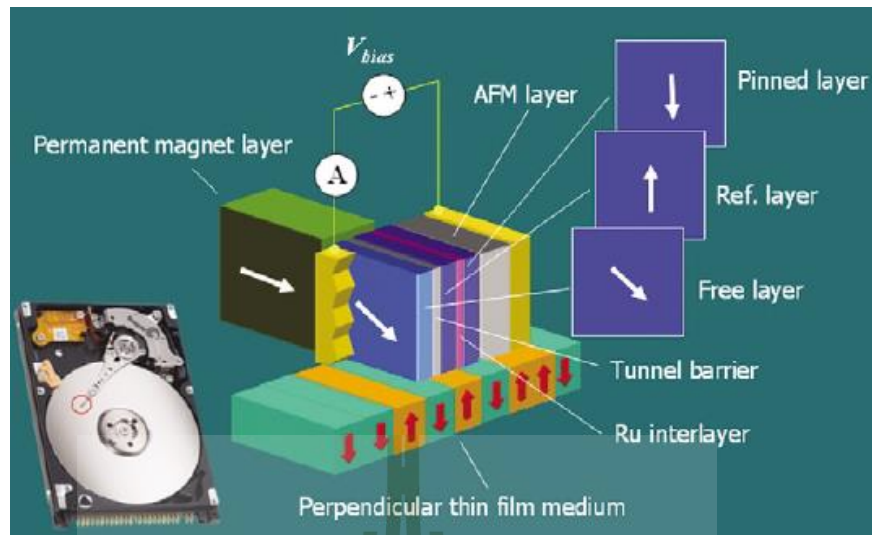
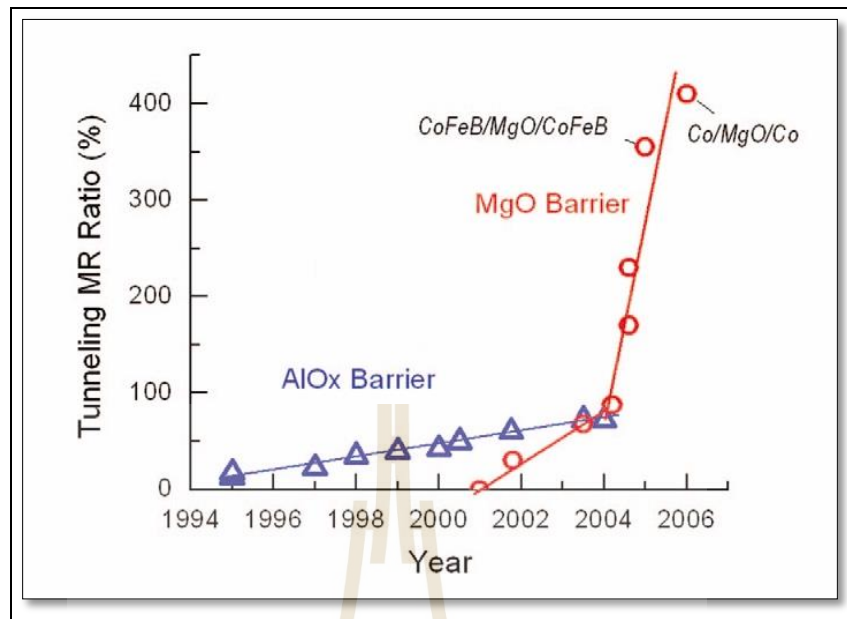


Figure 2.1 MTJ read head in an HDD (Zhu & Park, 2006)

Due to the suitability of thin forming, aluminum oxide ( $\text{Al}_2\text{O}_3$ ) was used as a tunnel barrier for early MTJ devices as a tunnel barrier, a thin ( $\sim 10 \text{ \AA}$ ), smooth, and dense barrier layer. Unfortunately, the oxidation of the Al layer usually leads to a significant decrease in the TMR ratio. The MR values of the  $\text{Al}_2\text{O}_3$  device were reported accurately up to 70% by using the  $\text{CoFeB}/\text{AlO}_x/\text{CoFeB}$  junction (Dexin et al., 2004). Recently, magnesium oxide (MgO) has also become the primary element of MTJ tunnel barriers because of the great improvement in performance. The earliest stage of MgO resulted in MR values of 220% at room temperature (Parkin et al., 2004). Recently, researchers have demonstrated room temperature MR values exceeding 600%, using variations of the stacks (Ikeda et al., 2010). The impact of these two-research works has led to a lot of studies that significantly increase the TMR values, as shown in Figure 2.2.





**Figure 2.2** TMR ratios over a few past decade for amorphous AlO<sub>x</sub>-based MTJs (blue triangles) and crystalline MgO-based MTJs (red circles) (Zhu & Park, 2006).

In addition, the hard drive manufacturers have explored a way to increase the quality of the HDD reader head by creating a soft magnetic side shield for improved sensor stability from MgO (Haginoya et al., 2004; Zheng et al., 2006) to reduce side reading effect, which can improve the signal-to-noise ratio. The manufacturing of an MTJ device consists of 3 primary steps which: 1) depositing the various films to make up the stack, 2) annealing to set the crystal structure of the films in the active region, and 3) etching the desired device's pattern. One of the essential steps in magnetic sensor fabrication is the annealing step associated with the variables including temperature, and environment such as gas environments, which may improve the device performance, such as the TMR ratio.

### 2.1.1 MgO dissolution

Magnesium oxide (MgO) thin film is used as a barrier for magnetic tunneling junction and magnetic shielding in magnetic data storage devices. During the fabrication process, the film is inevitably exposed to water during certain operations such as polishing, cutting and cleaning, these processes cause an expansive hydration

reaction that originates a soluble product such as  $\text{Mg}(\text{OH})_2$  (Amaral et al., 2011).  $\text{MgO}$  film is easily dissolved in water (86 ppm at 30 °C (Patnaik, 2003)) and reacts very easily with moisture in the air (Jones et al., 1984). Furthermore, chemical instability of  $\text{MgO}$  film due to the easy hydration and formation of  $\text{Mg}(\text{OH})_2$  under atmospheric conditions is a crucial issue. According to (Patnaik, 2003), the dissolution rate of  $\text{Mg}(\text{OH})_2$  is approximately 14 times lower than that of  $\text{MgO}$ . Therefore, the  $\text{Mg}(\text{OH})_2$  layer acts as a protective layer, slowing the decreasing  $\text{MgO}$  dissolution rate. In addition, the hydration process also increases the film volume, which leads to the residual stress in the device (Razouk & Mikhail, 1958) as shown in Figure 2.3.

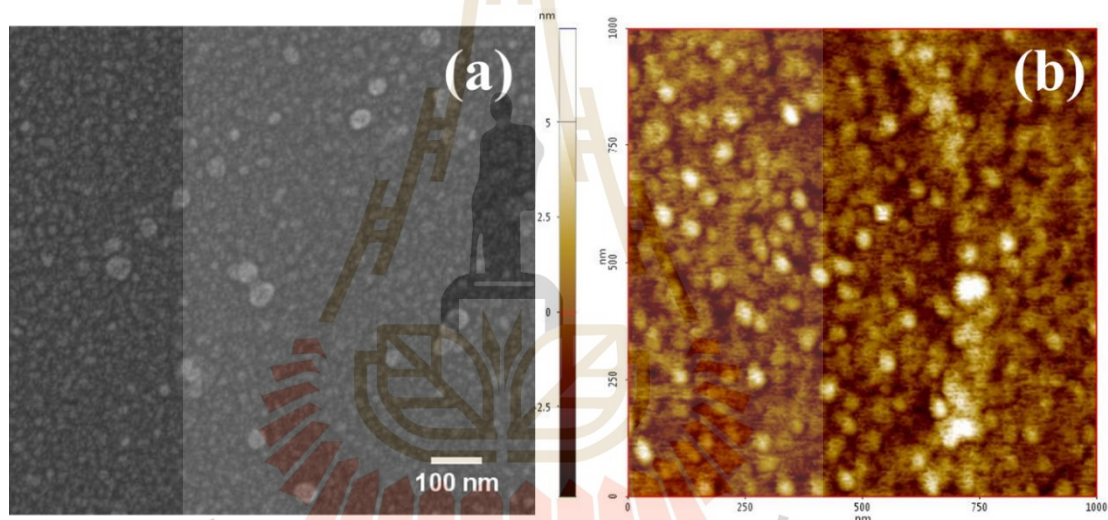
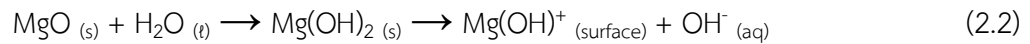


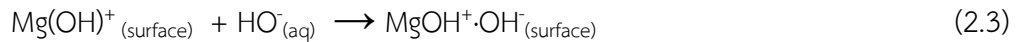
**Figure 2.3** (a) SEM micrograph (b) AFM topography of  $\text{MgO}$  thin film surface after being exposed to DI water 6 hours at room temperature.

The dissolution rate of magnesium oxide during hydration is one of the important factors involved in the mechanism of  $\text{MgO}$  hydration. The kinetics and hydration mechanisms of  $\text{MgO}$  comprises of the following steps:

a) The water vapor is chemically on  $\text{MgO}$ , then this reaction forms a liquid layer on the  $\text{MgO}$  surface as the following equation (2.2) (Rocha et al., 2004).



b) The liquid layer is formed then reacts with MgO to form a  $\text{Mg(OH)}_2$  layer (see equation (2.3)) (Holt et al., 1997).



c) The  $\text{Mg(OH)}_2$  is subsequently dissolved in this water layer as the following equation (2.4) (Rocha et al., 2004).



d) The layer saturated with  $\text{Mg(OH)}_2$  and precipitation occurs according to the following equation (2.5) (Kato et al., 1996).



The rate of hydration may be limited by the rate of  $\text{Mg(OH)}_2$  which is removed from the MgO surface. Very rapid hydration of MgO may result in the formation of large aggregation of hydroxide clusters. Such a surface condition may be unacceptable for thin film applications (Dimitrios et al., 1999). The dissolution rate also depends on temperature (Blaha, 1995c; Fedoročková & Raschman, 2008) and the exposed area (L. & N., 1969; Rocha et al., 2004). The 001 surface is the least susceptible to hydration as shown in Figure 2.4.

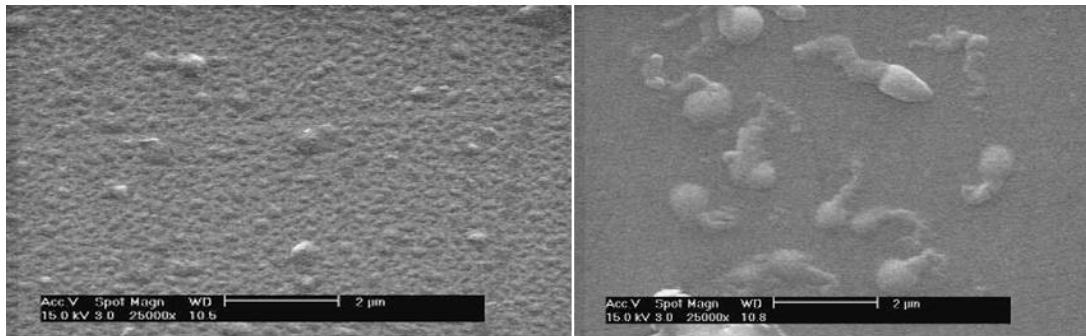


**Figure 2.4** Surface morphology of the 5-day--hydrated MgO (a) (001) Sputtered thin films (b) (111) Sputtered thin films (Lee et al., 2003).

It was found that after the MgO film was kept in a humid environment (relative humidity 60 – 70%), the crystal step gradually hydrated. Therefore, the environmental process must be carefully controlled to keep the humidity below 30%. (Holt et al., 1997). The hydration of MgO in water at different exposure times and temperatures make the thickness of MgO films decrease continuously during hydration despite the increase in mass loss due to hydration and reduction Hydration layer or  $\text{Mg(OH)}_2$  is formed during the hydration process; this definitely changes the properties of the film, hence a large effect on devices performance. For example, the thickness of the hydration layer ( $\text{Mg(OH)}_2$ ) could be 5 nm, which is approximately 50% of the thickness of MgO barrier or shielding in magnetic sensors. This may result in the decrease of the read sensitivity of the reader head.

### 2.1.2 Dissolution rate

The dissolution rate of magnesium oxide thin films is typically controlled by the quantity of the film dissolved in the water.  $\text{Mg(OH)}_2$  precipitation is influenced by the amount of water or moisture available as well as the exposure time. Additionally, the concentration is proportional to the amount of magnesium oxide dissolved in water. The following reaction rate equation can be used to explain the mass loss of MgO as a function of time. (Equation (2.6)).

$$R(t) = kC_1(t)C_2(t) \quad (2.6)$$

Where  $k$  denotes the reaction rate and  $C_1(t)$  and  $C_2(t)$  denote the amount of water and magnesium oxide, respectively, in this research, the researcher used MgO thin films, which were dissolved in a considerable volume of water. As a result, the concentration of MgO becomes the rate-limiting step, and equation (2.7) then becomes.

$$R(t) = kC_2(t) \quad (2.7)$$

In reality, either the reactant or the solution becomes saturated with  $Mg(OH)_2$  byproducts. As a result, the rate of dissolution decreases and eventually stops. Thus,  $Mg(OH)_2$  concentration as a function of time rapidly increases during the initial state followed by a plateau at an increasing time. Therefore, the plot of the product concentration as a function of time would show highly increases at the beginning and reach a tableland after some times. Dissolution of MgO crystals follows this trend, as shown in Figure 2.5.

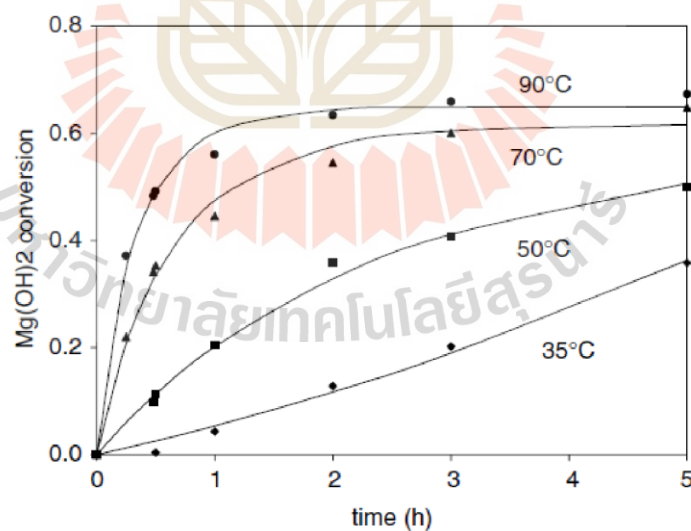


**Figure 2.5**  $Mg(OH)_2$  concentration as a function of time at various temperatures. (Birchal et al., 2001)

The reaction rate,  $k$ , from the product concentration as a function of time can be calculated by evaluating the slope of the graph. Arrhenius equations are widely used to describe reaction rates as the following equation:

$$k = Ae^{-E_A/k_B T} \quad (2.8)$$

where  $E_A$  is the activation energy,  $k_B$  denotes Boltzmann's constant, and  $A$  denotes the collision rate, which is strongly dependent on the surface area. The slope is proportional to  $E_A$  when  $k$  and  $1/T$  are shown on a logarithmic scale (Thomas et al., 2008). A method for evaluating the dissolution rate is represented in Figure 2.5. (Fruhirth et al., 1985). MgO conducted at a rate proportional to its concentration in water. MgO concentration measurements are obtained over an extended period of time with high resolution on a single sample.

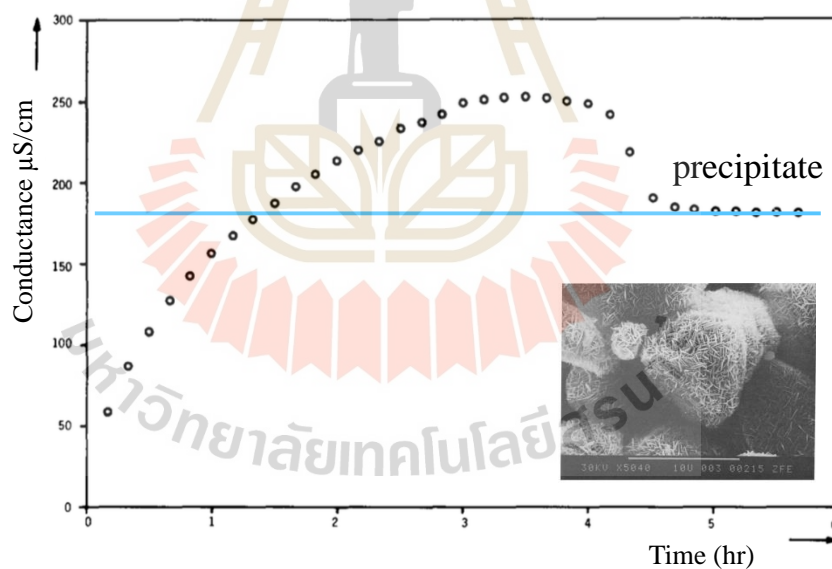


**Figure 2.6** MgO dissolution rate obtained by measuring conductivity of water as a function of time. Plateau after long-term exposure indicates saturation. The inset shows a needle-like crystal on the surface, which is  $Mg(OH)_2$  precipitation (Fruhirth et al., 1985).

The dissolution rate of MgO can be determined the mass lost during dissolution or by determining the concentration of MgO in water, which is time dependent. To evaluate the activation energy, it is essential to define the magnesium oxide concentration as a function of time and temperature. In this research, both mass loss and the discrete concentration measurement methods are inefficient. Therefore, the MgO should be measured in concentration in the water by monitoring the solution conductivity. If the dissolution could be measured in real time, it would be able to study the dissolution behavior as a function of time. Finally, the mass loss of the film during the manufacturing process may be evaluated due to dissolving in water solution.

## 2.2 MgO heat treatment

Many studies have found that thermal annealing improves the dielectric strength and lifetime of oxides while also decreasing leakage current (Cheng et al., 2016; Jo & Park, 1998; Keiji et al., 2010; Tanigaki et al., 1988). Thermal annealing can reduce the porosity (Cheng et al., 2016) and defects (Furukawa et al., 1997), and change the dielectric constant (Cheng et al., 2016). However, the annealing process has undesirable outcomes such as oxide degradation (Tanigaki et al., 1988), changes in chemical composition (Kang et al., 2004), structural changes (Kang et al., 2004; Wang et al., 2016), or migration of material from another layer (Bae et al., 2006; Wang et al., 2008).

The temperature of annealing is typically between 300 and 800 °C, in a vacuum, Ar, N<sub>2</sub>, or O<sub>2</sub> gas environment. Thermal annealing (also known as calcination) of magnesium oxide can remove surface absorbents such as water, hydroxyl (OH<sup>-</sup>) groups, (Kumari et al., 2009; Peng & Barteau, 1990), and carbonyl (CO<sup>-</sup>) groups (Rheinheimer et al., 2017). Recently, it has been discovered that vacuum annealing Al-doped MgO nanoparticles increased the number of oxygen vacancies in the materials, altering the material's magnetic properties (Mishra et al., 2013).

The annealing effect on MgO in MJT is an interesting subject. In MJT, the MgO barrier is placed adjacent to the CoFeB layer. It was shown that the annealing process improved the crystallinity of the structure at the interface of the MgO and CoFeB; due

to the increasing magnetoresistance (Park et al., 2006). However, the annealing process may decrease the breakdown voltage of the MJT (Khan et al., 2008). Many researchers found the boron atom (B) in this layer diffuse into the MgO layer during the annealing process, resulting in a lower magnetoresistance and dielectric lifetime (Bae et al., 2006; Hayakawa et al., 2006; Komagaki et al., 2009; Read et al., 2007). The annealing process may also change the interfacial structures of the MJT (Bae et al., 2006; Wang et al., 2008). A study suggested a way to stop boron diffusion by inserting a Mo buffer layer before the Ta layer (Liu et al., 2014). It was also found that the increase in annealing temperature also increased MgO surface roughness (Aswal et al., 2002; L. Platt et al., 2002). Over annealing temperature always changes MgO thin film properties, especially, in terms of physical properties, because it reduces the magnetic sensitivity of the magnetic sensor and increases surface roughness related to the magnetic sensor, which maintains the distance between the reader and the magnetic plate (Marchon et al., 2013).

## 2.3 Characterization of MgO thin films

### 2.3.1 Electrical conductivity (EC)

Electrolysis is the process by which solutions decompose when exposed to an electric current. Acids and bases are generally composed of two types of ions: cations and anions. Figure 2.7. illustrates the electrolysis of the MgO in solution. To begin with, MgO is decomposed in water into Mg and O ions.



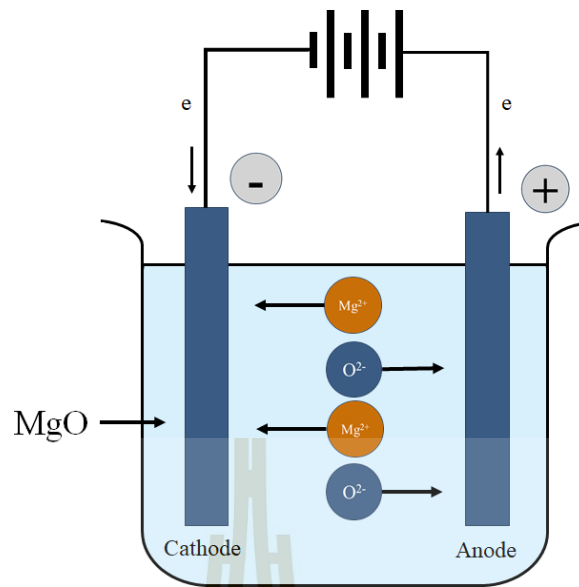


**Figure 2.7** Electrolytic conduction of MgO in aqueous solution

Conductance is a measure of how easily an electric current flows through a material. It is caused by electron movement in metallic conductors, whereas it is induced by ion flow in electrolytic solutions. A medium electrolytic conductance,  $G$ , is equal to the reciprocal of its electrical resistance,  $R$ , in ohms.

$$G = \frac{1}{R} \quad (2.9)$$

The actual resistance depends on the electrode spacing ( $l$ ) and area ( $A$ ). In such a condition, the resistance of a solution is directly proportional to the distance between the electrodes ( $l$ ) and inversely proportional to the electrode cross-sectional area ( $A$ ). When these numbers are combined using equation 2.9, the following result is obtained:

$$R = \rho \frac{l}{A} \quad (2.10)$$

Where  $\rho$  is the resistivity of the electrolytic solution, measured in  $\Omega \cdot \text{m}$ . The conductivity ( $\sigma$ ) is the reciprocal of the resistivity ( $\rho$ ) and is measured in  $\text{mS/cm}$  or  $\mu\text{S/cm}$ .

$$\rho = \frac{l}{\sigma} \quad (2.11)$$

The cell constant ( $K$ ) is defined as the ratio of the distance ( $l$ ) between the electrodes to their area ( $A$ ).

$$k = \frac{l}{A} \quad (2.12)$$

Where  $K$  = cell constant ( $\text{cm}^{-1}$ )  $A$  = effective area of the electrodes ( $\text{cm}^2$ ). Conductivity refers to a solution, a metal, or a gas's ability to conduct an electric current. Current is carried by electrons in metals, whereas it is carried by cations and anions in solutions.

### The conductivity meters

Alternating current ( $I$ ) is applied to two electrodes at an appropriate frequency, and the potential ( $P$ ) is measured as a function of time ( $V$ ). Using both current and potential, the conductance ( $I/V$ ) can be calculated. The conductivity meter then calculates the conductivity using the conductance and cell constant (equation 2.13). The simplified conductivity meter diagram is shown in Figure 2.8.

$$\text{Conductivity} = \text{cell constant} \times \text{conductance} \quad (2.13)$$

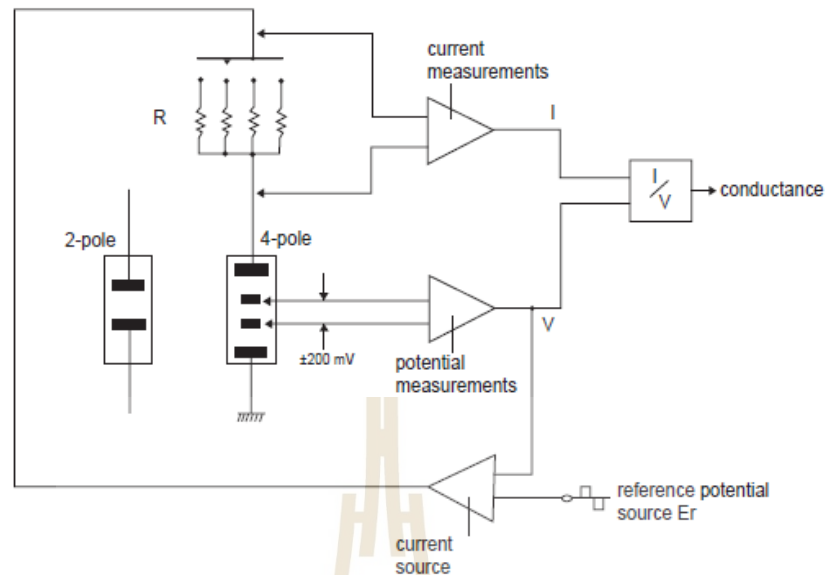


Figure 2.8 Simplified conductivity meter diagram

Conductivity is determined by several factors:

1. Concentration
2. Ion mobility
3. Ion valence
4. Temperature

Conductivity is a characteristic of all materials. Conductivity ranges from ultrapure water to concentrated chemical samples in aqueous solutions, depending on their ionic strengths.

### 2.3.2 Ellipsometer

Ellipsometry is a technique for determining the polarization change caused by light reflecting or transmitting through a material structure. An amplitude ratio (psi:  $\Psi$ ), and a phase difference (delta:  $\Delta$ ) are used to indicate the polarization shift. Therefore, ellipsometry is widely used to determine the thickness of films as well as their optical constants. However, it is also used to describe the composition, crystallinity, roughness, and doping concentration of materials that exhibit a shift in

optical responses. The reflected light exhibits amplitude and phase shifts, which are quantified using ellipsometry as shown in Figure 2.9.

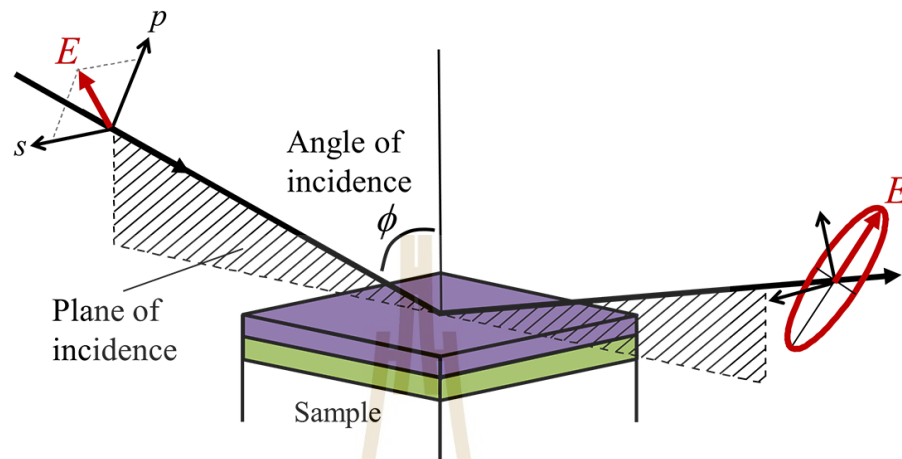


**Figure 2.9** The ellipsometry measurement uses linearly polarized light with both p and s components. As a result of contact with the sample, elliptically polarized light is produced (Tompkins & Hilfiker, 2015).

The shift in polarization is referred to the ellipsometry measurement (Fujiwara, 2007), which is typically represented as equation 2.13:

$$\rho = \tan(\psi)e^{i\Delta} \quad (2.13)$$

To obtain ellipsometry data, the author researcher used the primary instruments, including the light source, polarization generator, sample, polarization analyzer, and detector... A polarization generator and analyzer are composed of optical components modifying polarization: polarizers, compensators, and phase modulators. The rotating analyzer (RAE), the rotating polarizer (RPE), the rotating compensator (RCE), and phase modulation (PME) are all common ellipsometer setups.

The measured data are compared to the input light source with known polarization data for evaluating the polarization change of the sample. The Psi and Delta ellipsometry measurement is illustrated in Figure 2.10.

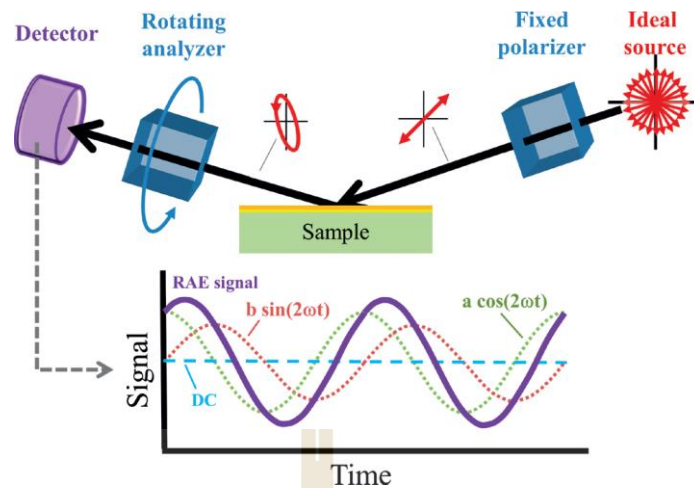


**Figure 2.10** A schematic setup of a rotating analyzer ellipsometer (RAE) (Tompkins & Hilfiker, 2015).

A model is created to define the sample after the measurement. Comparisons are made between the calculated values and experimental data. To measure the difference between curves, an estimator such as the Mean Squared Error (MSE) is utilized. Variation of the unknown parameters is allowed until the minimum MSE is reached. The optimal approach is the one that has the smallest MSE.

**Table 2.1** Advantages and disadvantages of SE

Advantages	disadvantages
No contact with the films is required	indirect method characterization (necessity of an optical model)
No references or standard is required	Data analysis tends to be complicated
High precision (sensitivity: $\sim 0.1\text{\AA}$ )	Spatial resolution is limited (spot size: several mm)
It is possible to monitor in real time (feedback control)	Difficulty in characterizing absorption coefficients less than $100\text{ cm}^{-1}$

### 2.3.3 Atomic force microscopy (AFM)

AFM is a high-resolution scanning probe microscope with a resolution of fractions of Angstroms that has a resolution 11,000 times greater than that of a conventional optical microscope. AFM utilizes a micro- and nanoscale cantilever equipped with a sharp silicon or silicon nitride tip (probe) to scan the specimen surface at the nanoscale level. Applied forces between the tip and the surface can be quantified to detect mechanical contact, magnetic, van der Waals interaction, electrostatic, capillary, chemical, and electrostatic forces, depending on the application (Ishida & Craig, 2019). Typically, an AFM unit can operate in three separate modes: contact mode, noncontact mode, and tapping mode.

Figure 2.11 illustrates the various modes of AFM. The most frequently used technique for surface force measurements is the contact mode, in which the cantilever tip scans the sample in close contact with the surface. In noncontact mode, the tip typically hovers approximately 5-15 nm above the substrate's surface. On the other hand, tapping mode AFM addresses issues such as friction, tip contact with rough surfaces, electrostatic forces, adhesion, and other difficulties encountered during the tapping process.

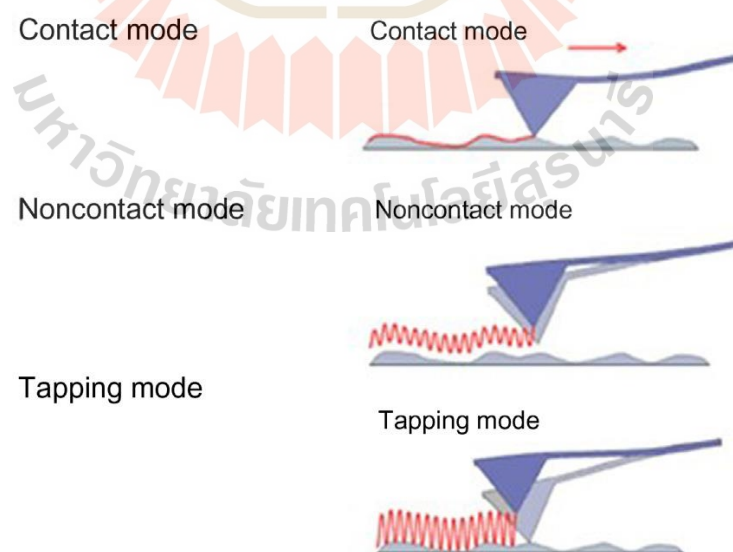


**Figure 2.11** Various AFM modes have been developed, including contact mode, noncontact mode, and tapping mode (Asmatulu & Khan, 2019).

### 2.3.4 Focused ion beam (FIB)

Typically, the FIB is used to create extremely fine cross sections (less than 100 nm precision) of a material in preparation for further imaging by SEM, STEM, or TEM. The dual beam FIB combines these two techniques into a single piece of equipment, allowing for sample preparation using the FIB and SEM imaging without exchanging the specimen, as shown in Figure 2.12.

The focused ion beam (FIB) column is an optical instrument that focuses and scans an accelerated ion beam on a sample in a vacuum chamber. Such a column can be used for two main purposes:

- 1) To form scanning ion images by collecting the secondary electrons (SE) generated by the interaction of the incident ions with the sample surface.
- 2) To locally sputter the material surface to directly fabricate arbitrary nanostructures.

The most commercially available FIB systems use gallium (Ga) ions for micromachining of the surfaces (Giannuzzi, 2005). FIB uses a strong electric field to speed up gallium ions to a typical speed of 10–50 keV (Giannuzzi et al., 2005). The basic functions of the FIB, namely, imaging and sputtering with an ion beam (meaning milling or etching), require a highly focused beam for high resolution.

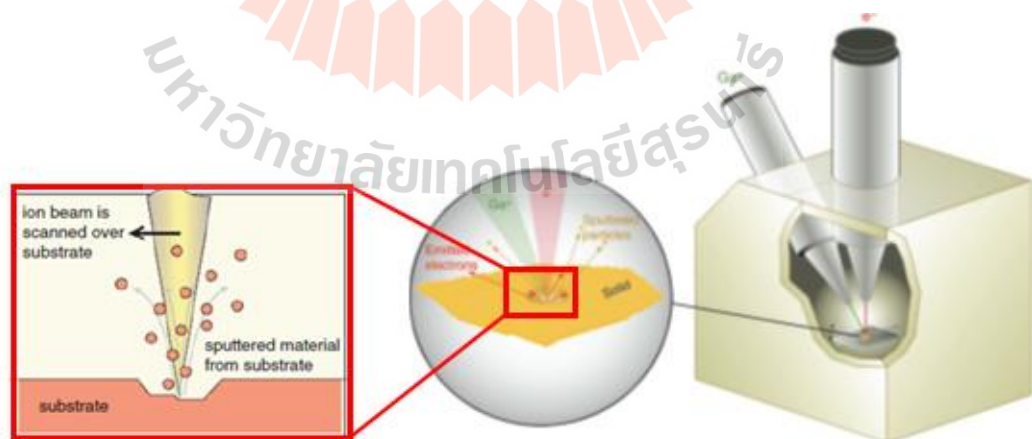


**Figure 2.12** dual-beam FIB–SEM instrument is represented in a schematic diagram.

The interaction between the electron and ion beam samples is shown in greater detail inside this image (Volkert & Minor, 2007)

### 2.3.5 X-ray photo electron spectroscopy (XPS)

XPS, also known as electron spectroscopy for chemical analysis, is commonly used to analyze the chemical composition of surfaces (Mather, 2009). XPS works on the principle of the photoelectric effect. Typically, Mg  $k\alpha$  (1253.6 eV), Al  $k\alpha$  (1486.6 eV), or monochromatic Al  $K\alpha$  (1486.7 eV) X-rays are employed as the monoenergetic source. These photons have a limited penetration depth of around 1-10 nanometers in a solid material. They can only interact with the atoms on the material's surface, resulting in the emission of electrons through the photoelectric effect. The measured kinetic energy of the emitted electrons is determined by the following equation:

$$KE = h\nu - BE - \theta_s \quad (2.14)$$

Where  $h\nu$  denotes the photon's energy, BE denotes the binding energy of the atomic orbital from which the electron originates, and  $\theta_s$  denotes the work function of the spectrometer.

Figure 2.13 illustrates the fundamental operation of an XPS instrument. A precise energy photon is employed to excite the electronic states of atoms under the sample's surface. Emitted from the surface, the electron of which the intensity for a specific energy level is recorded by a detector after being filtered for energy by a hemispherical analyzer (HSA).



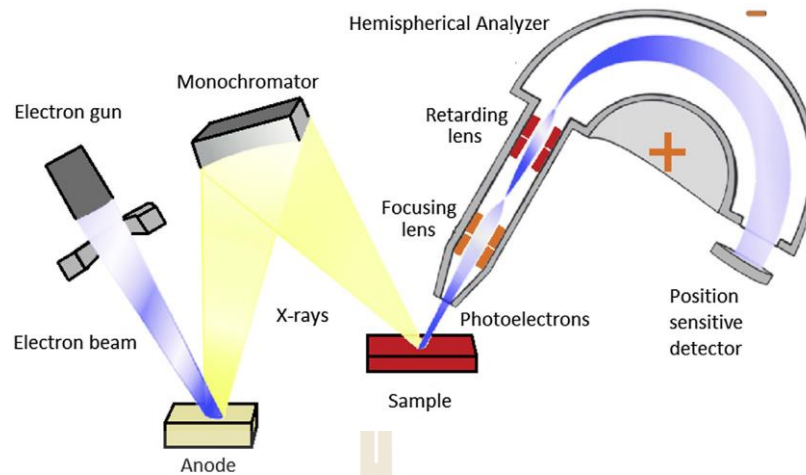


**Figure 2.13** Schematic drawing of an XPS instrument (Watts & Wolstenholme, 2019)

An XPS spectrum is a graph of the number of electrons detected (sometimes per unit time) (Y-axis) versus the binding energy of the electrons detected (X-axis). Each element exhibits a specific set of XPS peaks exhibiting unique binding energies that directly identify the element present in or on the surface of the material being investigated, as shown in Figure 2.14.

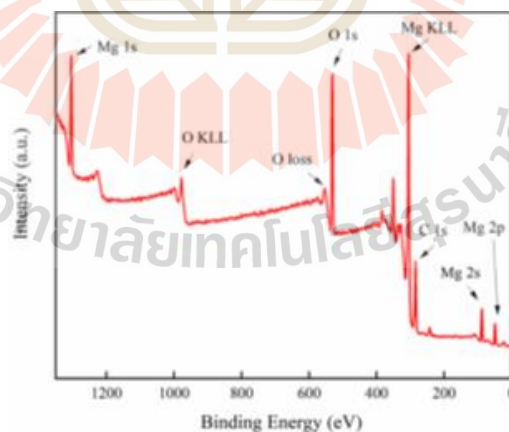


**Figure 2.14** XPS spectra MgO survey scan (Peng et al., 2020)

## Sputter Depth Profiling

It is a surface-sensitive quantitative technique that combines ion gun etching with XPS chemical composition analysis to provide a sample's depth profile. In this experiment, an ion gun is used to etch the material for a period of time before being switched off and the XPS spectra are acquired. A fresh surface is exposed after each ion gun etching cycle, and the XPS spectra provide the analytical method to determine the composition of the surfaces that are currently operating as shown in Figure 2.15.

Sputter rates are the rate at which a surface is etched (removed) as a result of an energetic ion collision. From less than a monolayer per minute to levels of more than 10 nm/min, this process may be achieved.

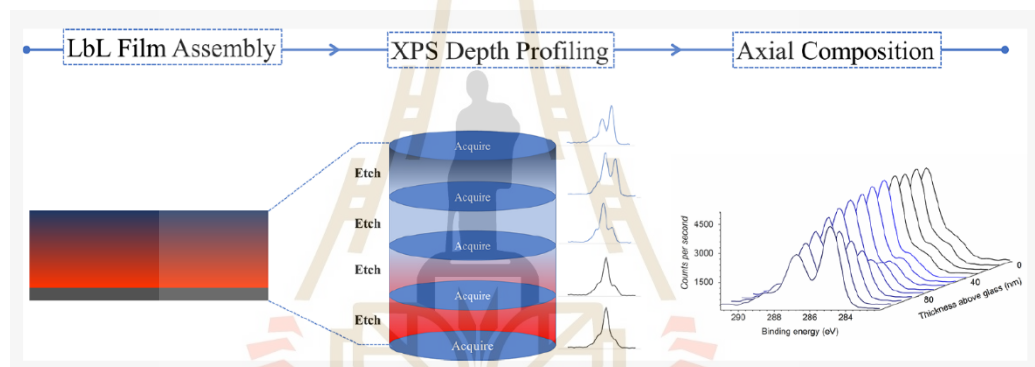


Figure 2.15 schematic of XPS depth profiling (Taketa et al., 2020)

## 2.4 References

- Amaral, L. F., Oliveira, I. R., Bonadia, P., Salomão, R., & Pandolfelli, V. C. (2011, 7//). Chelants to inhibit magnesia (MgO) hydration. *Ceramics International*, 37(5), 1537-1542. <https://doi.org/http://dx.doi.org/10.1016/j.ceramint.2011.01.030>
- Asmatulu, R., & Khan, W. S. (2019). Chapter 13 - Characterization of electrospun nanofibers. In R. Asmatulu & W. S. Khan (Eds.), *Synthesis and Applications of Electrospun Nanofibers* (pp. 257-281). Elsevier. <https://doi.org/> <https://doi.org/10.1016/B978-0-12-813914-1.00013-4>

- Aswal, D. K., Muthe, K. P., Tawde, S., Chodhury, S., Bagkar, N., Singh, A., Gupta, S. K., & Yakhmi, J. V. (2002, 2002/03/01/). XPS and AFM investigations of annealing induced surface modifications of MgO single crystals. *Journal of Crystal Growth*, 236(4), 661-666. [https://doi.org/https://doi.org/10.1016/S0022-0248\(02\)00852-7](https://doi.org/https://doi.org/10.1016/S0022-0248(02)00852-7)
- Bae, J. Y., Lim, W. C., Kim, H. J., Lee, T. D., Kim, K. W., & Kim, T. W. (2006). Compositional change of MgO barrier and interface in CoFeB/MgO/CoFeB tunnel junction after annealing. *Journal of Applied Physics*, 99(8), 08T316. <https://doi.org/doi:http://dx.doi.org/10.1063/1.2170591>
- Birchal, V. S., Rocha, S. D. F., Mansur, M. B., & Ciminelli, V. S. T. (2001). A simplified mechanistic analysis of the hydration of magnesia. *The Canadian Journal of Chemical Engineering*, 79(4), 507-511. <https://doi.org/10.1002/cjce.5450790406>
- Blaha, J. (1995). KINETICS OF HYDRATION OF MAGNESIUM OXIDE IN AQUEOUS SUSPENSION. PT. 1. METHOD OF MEASUREMENT AND EVALUATION OF EXPERIMENTAL DATA. *Ceramics- Silikaty*, 39(2), 45-51.
- Cheng, Y.-L., Kao, K.-C., Chen, G.-S., Fang, J.-S., Sun, C.-R., & Lee, W.-H. (2016, 2016/08/16/). Effect of annealing temperature on electrical and reliability characteristics of HfO<sub>2</sub>/porous low-k dielectric stacks. *Microelectronic Engineering*, 162 (Supplement C), 34-39. <https://doi.org/https://doi.org/10.1016/j.mee.2016.04.013>
- Dexin, W., Nordman, C., Daughton, J. M., Zhenghong, Q., & Fink, J. (2004). 70% TMR at room temperature for SDT sandwich junctions with CoFeB as free and reference Layers. *IEEE Transactions on Magnetics*, 40(4), 2269-2271. <https://doi.org/10.1109/TMAG.2004.830219>
- Dimitrios, F., Nikolaos, K., Nymphodora, P., & Katerina, A. (1999). On the kinetics of magnesia hydration in magnesium acetate solutions. *Journal of Chemical Technology & Biotechnology*, 74(4), 322-328. [https://doi.org/doi:10.1002/\(SICI\)1097-4660\(199904\)74:4<322::AID-JCTB35>3.0.CO;2-L](https://doi.org/doi:10.1002/(SICI)1097-4660(199904)74:4<322::AID-JCTB35>3.0.CO;2-L)
- Fedorocková, A., & Raschman, P. (2008, 9/15/). Effects of pH and acid anions on the dissolution kinetics of MgO. *Chemical Engineering Journal*, 143(1-3), 265-272. <https://doi.org/http://dx.doi.org/10.1016/j.cej.2008.04.029>

- Fruhwith, O., Herzog, G. W., Hollerer, I., & Rchetti, A. (1985, 1985/03/01). Dissolution and hydration kinetics of MgO. *Surface Technology*, 24(3), 301-317. [https://doi.org/http://dx.doi.org/10.1016/0376-4583\(85\)90080-9](https://doi.org/http://dx.doi.org/10.1016/0376-4583(85)90080-9)
- Fujiwara, H. (2007). Spectroscopic ellipsometry : principles and applications. <http://public.ebib.com/choice/publicfullrecord.aspx?p=315058>
- Furukawa, T., Yuuki, A., & Ono, K. (1997, 1997/10/01). Recovery of time-dependent dielectric breakdown lifetime of thin oxide films by thermal annealing. *Journal of Applied Physics*, 82(7), 3462-3468. <https://doi.org/10.1063/1.365662>
- Haginoya, C., Hatatani, M., Meguro, K., Ishikawa, C., Yoshida, N., Kusukawa, K., & Watanabe, K. (2004). Side-shielded tunneling magnetoresistive read head for high-density recording. *IEEE Transactions on Magnetics*, 40(4), 2221-2223. <https://doi.org/10.1109/TMAG.2004.829157>
- Hayakawa, J., Ikeda, S., Lee, Y. M., Matsukura, F., & Ohno, H. (2006). Effect of high annealing temperature on giant tunnel magnetoresistance ratio of CoFeB/MgO/CoFeB magnetic tunnel junctions. *Applied Physics Letters*, 89(23), 232510. <https://doi.org/10.1063/1.2402904>
- Holt, S. A., Jones, C. F., Watson, G. S., Crossley, A., Johnston, C., Sofield, C. J., & Myhra, S. (1997, 1997/01/05). Surface modification of MgO substrates from aqueous exposure: an atomic force microscopy study. *Thin Solid Films*, 292(1), 96-102. [https://doi.org/http://dx.doi.org/10.1016/S0040-6090\(96\)08955-9](https://doi.org/http://dx.doi.org/10.1016/S0040-6090(96)08955-9)
- Ikeda, S., Miura, K., Yamamoto, H., Mizunuma, K., Gan, H. D., Endo, M., Kanai, S., Hayakawa, J., Matsukura, F., & Ohno, H. (2010, 09//print). A perpendicular-anisotropy CoFeB–MgO magnetic tunnel junction [10.1038/nmat2804]. *Nat Mater*, 9(9), 721-724. <http://dx.doi.org/10.1038/nmat2804>
- Ishida, N., & Craig, V. (2019, 01/10). Direct Measurement of Interaction Forces between Surfaces in Liquids Using Atomic Force Microscopy. *KONA Powder and Particle Journal*, 36. <https://doi.org/10.14356/kona.2019013>
- Jo, M.-H., & Park, H.-H. (1998). Leakage current and dielectric breakdown behavior in annealed SiO<sub>2</sub> aerogel films. *Applied Physics Letters*, 72(11), 1391-1393. <https://doi.org/10.1063/1.121065>

- Jones, C. F., Reeve, R. A., Rigg, R., Segall, R. L., Smart, R. S. C., & Turner, P. S. (1984). Surface area and the mechanism of hydroxylation of ionic oxide surfaces [10.1039/F19848002609]. *Journal of the Chemical Society, Faraday Transactions 1: Physical Chemistry in Condensed Phases*, 80(10), 2609-2617. <https://doi.org/10.1039/F19848002609>
- Kang, H. S., Kang, J. S., Kim, J. W., & Lee, S. Y. (2004). Annealing effect on the property of ultraviolet and green emissions of ZnO thin films. *Journal of Applied Physics*, 95(3), 1246-1250. <https://doi.org/10.1063/1.1633343>
- Kato, Y., Yamashita, N., Kobayashi, K., & Yoshizawa, Y. (1996, 1996/11/01/). Kinetic study of the hydration of magnesium oxide for a chemical heat pump. *Applied Thermal Engineering*, 16(11), 853-862. [https://doi.org/http://dx.doi.org/10.1016/1359-4311\(96\)00009-9](https://doi.org/http://dx.doi.org/10.1016/1359-4311(96)00009-9)
- Keiji, H., Makoto, N., Tomomasa, U., Hisanori, A., Sumio, I., Yoshiaki, A., Hiroaki, Y., & Akihiro, N. (2010). Effect of Self-Heating on Time-Dependent Dielectric Breakdown in Ultrathin MgO Magnetic Tunnel Junctions for Spin Torque Transfer Switching Magnetic Random Access Memory. *Japanese Journal of Applied Physics*, 49(4S), 04DD15. <http://stacks.iop.org/1347-4065/49/i=4S/a=04DD15>
- Khan, A. A., Schmalhorst, J., Thomas, A., Schebaum, O., & Reiss, G. (2008). Dielectric breakdown in Co-Fe-B/MgO/Co-Fe-B magnetic tunnel junction. *Journal of Applied Physics*, 103(12), 123705. <https://doi.org/10.1063/1.2939571>
- Komagaki, K., Hattori, M., Noma, K., Kanai, H., Kobayashi, K., Uehara, Y., Tsunoda, M., & Takahashi, M. (2009). Influence of Diffused Boron Into MgO Barrier on Pinhole Creation in CoFeB/MgO/CoFeB Magnetic Tunnel Junctions. *IEEE Transactions on Magnetics*, 45(10), 3453-3456. <https://doi.org/10.1109/TMAG.2009.2022189>
- Kumari, L., Li, W. Z., Vannoy, C. H., Leblanc, R. M., & Wang, D. Z. (2009, 12/). Synthesis, characterization and optical properties of Mg(OH)<sub>2</sub> micro-/nanostructure and its conversion to MgO. *Ceramics International*, 35(8), 3355-3364. <https://doi.org/http://dx.doi.org/10.1016/j.ceramint.2009.05.035>

- L. Platt, C., Wierman, K. W., B. Svedberg, E., van de Veerdonk, R., K. Howard, J., Roy, A., & Laughlin, D. (2002). *L-1 0 ordering and microstructure of FePt thin films with Cu, Ag, Au additive* (Vol. 92). <https://doi.org/10.1063/1.1516870>
- L., S. G., & N., B. N. (1969). The kinetics and mechanism of the hydration of magnesium oxide in a batch reactor. *The Canadian Journal of Chemical Engineering*, 47(6), 508-513. <https://doi.org/doi:10.1002/cjce.5450470602>
- Lee, J. H., Eun, J. H., Kim, S. G., Park, S. Y., Lee, M. J., & Kim, H. J. (2003, 2003/12/001). Hydration behavior of MgO single crystals and thin films. *Journal of Materials Research*, 18(12), 2895-2903. <https://doi.org/10.1557/JMR.2003.0404>
- Liu, T., Zhang, Y., Cai, J. W., & Pan, H. Y. (2014, 07/31 03/20/received 07/14/accepted). Thermally robust Mo/CoFeB/MgO trilayers with strong perpendicular magnetic anisotropy. *Scientific Reports*, 4, 5895. <https://doi.org/10.1038/srep05895>
- Marchon, B., Pitchford, T., Hsia, Y.-T., & Gangopadhyay, S. (2013). The Head-Disk Interface Roadmap to an Areal Density of Tbit/in<sup>2</sup>. *Advances in Tribology*, 2013, 8, Article 521086. <https://doi.org/10.1155/2013/521086>
- Mather, R. R. (2009). Surface modification of textiles by plasma treatments. In Q. Wei (Ed.), *Surface Modification of Textiles* (pp. 296-317). Woodhead Publishing. <https://doi.org/https://doi.org/10.1533/9781845696689.296>
- Mishra, D., Mandal, B. P., Mukherjee, R., Naik, R., Lawes, G., & Nadgorny, B. (2013). Oxygen vacancy enhanced room temperature magnetism in Al-doped MgO nanoparticles. *Applied Physics Letters*, 102(18), 182404. <https://doi.org/doi:10.1063/1.4804425>
- Park, C., Zhu, J.-G., Moneck, M. T., Peng, Y., & Laughlin, D. E. (2006). Annealing effects on structural and transport properties of rf-sputtered CoFeB/MgO/CoFeB magnetic tunnel junctions. *Journal of Applied Physics*, 99(8), 08A901. <https://doi.org/10.1063/1.2165141>
- Parkin, S. S. P., Kaiser, C., Panchula, A., Rice, P. M., Hughes, B., Samant, M., & Yang, S.-H. (2004, 10/31/online). Giant tunnelling magnetoresistance at room temperature with MgO (100) tunnel barriers. *Nature Materials*, 3, 862. <https://doi.org/10.1038/nmat1256>

- Patnaik, P. (2003). *Handbook of Inorganic Chemicals*. McGraw-Hill.
- Peng, Q., Dai, Y., Liu, K., Luo, X., He, D., Tang, X., & Huang, G. (2020, 2020/09/01). A novel carbon nanotube–magnesium oxide composite with excellent recyclability to efficiently activate peroxymonosulfate for Rhodamine B degradation. *Journal of Materials Science*, *55*(25), 11267-11283. <https://doi.org/10.1007/s10853-020-04822-0>
- Peng, X. D., & Barteau, M. A. (1990, September 01). Dehydration of carboxylic acids on the MgO(100) surface [journal article]. *Catalysis Letters*, *7*(5), 395-402. <https://doi.org/10.1007/bf00764930>
- Razouk, R. I., & Mikhail, R. S. (1958, 1958/08/01). The Hydration of Magnesium Oxide from the Vapor Phase. *The Journal of Physical Chemistry*, *62*(8), 920-925. <https://doi.org/10.1021/j150566a006>
- Read, J. C., Mather, P. G., & Buhrman, R. A. (2007). X-ray photoemission study of CoFeB/MgO thin film bilayers. *Applied Physics Letters*, *90*(13), 132503. <https://doi.org/doi:http://dx.doi.org/10.1063/1.2717091>
- Rheinheimer, V., Unluer, C., Liu, J., Ruan, S., Pan, J., & Monteiro, P. (2017). XPS Study on the Stability and Transformation of Hydrate and Carbonate Phases within MgO Systems. *Materials*, *10*(1), 75. <http://www.mdpi.com/1996-1944/10/1/75>
- Rocha, S. D. F., Mansur, M. B., & Ciminelli, V. S. T. (2004). Kinetics and mechanistic analysis of caustic magnesia hydration. *Journal of Chemical Technology & Biotechnology*, *79*(8), 816-821. <https://doi.org/10.1002/jctb.1038>
- Taketa, T. B., Rocha Neto, J. B. M., dos Santos, D. M., Fiamingo, A., Beppu, M. M., Campana-Filho, S. P., Cohen, R. E., & Rubner, M. F. (2020, 2020/05/12). Tracking Sulfonated Polystyrene Diffusion in a Chitosan/Carboxymethyl Cellulose Layer-by-Layer Film: Exploring the Internal Architecture of Nanocoatings. *Langmuir*, *36*(18), 4985-4994. <https://doi.org/10.1021/acs.langmuir.0c00544>
- Tanigaki, Y., Moribe, S., & Itagaki, T. (1988, 13-14 June 1988). The effects of annealing ambients on dielectric strength of gate oxides with tungsten polycide gate. 1988. Proceedings., Fifth International IEEE VLSI Multilevel Interconnection Conference,

- Thomas, A., Drewello, V., Schäfers, M., Weddemann, A., Reiss, G., Eilers, G., Münzenberg, M., Thiel, K., & Seibt, M. (2008). Direct imaging of the structural change generated by dielectric breakdown in MgO based magnetic tunnel junctions. *Applied Physics Letters*, *93*(15), 152508. <https://doi.org/10.1063/1.3001934>
- Tompkins, H. G., & Hilfiker, J. N. (2015). *Spectroscopic Ellipsometry: Practical Application to Thin Film Characterization*. Momentum Press. <https://books.google.co.th/books?id=Cj81CwAAQBAJ>
- Volkert, C. A., & Minor, A. M. (2007). Focused Ion Beam Microscopy and Micromachining. *MRS Bulletin*, *32*(5), 389-399. <https://doi.org/10.1557/mrs2007.62>
- Wang, W. G., Ni, C., Rumaiz, A., Wang, Y., Fan, X., Moriyama, T., Cao, R., Wen, Q. Y., Zhang, H. W., & Xiao, J. Q. (2008). Real-time evolution of tunneling magnetoresistance during annealing in CoFeB/MgO/CoFeB magnetic tunnel junctions. *Applied Physics Letters*, *92*(15), 152501. <https://doi.org/doi:http://dx.doi.org/10.1063/1.2903147>
- Wang, Z., Saito, M., McKenna, K. P., Fukami, S., Sato, H., Ikeda, S., Ohno, H., & Ikuhara, Y. (2016, Mar 9). Atomic-Scale Structure and Local Chemistry of CoFeB-MgO Magnetic Tunnel Junctions. *Nano Lett*, *16*(3), 1530-1536. <https://doi.org/10.1021/acs.nanolett.5b03627>
- Watts, J. F., & Wolstenholme, J. (2019). *An Introduction to Surface Analysis by XPS and AES*. Wiley. <https://books.google.co.th/books?id=kDy5DwAAQBAJ>
- Zheng, Y. K., Han, G. C., Li, K. B., Guo, Z. B., Qiu, J. J., Tan, S. G., Liu, Z. Y., Liu, B., & Wu, Y. H. (2006). Side Shielded TMR Reader With Track-Width-Reduction Scheme. *IEEE Transactions on Magnetics*, *42*(10), 2303-2305. <https://doi.org/10.1109/TMAG.2006.880463>
- Zhu, J.-G., & Park, C. (2006, 2006/11/01/). Magnetic tunnel junctions. *Materials Today*, *9*(11), 36-45. [https://doi.org/https://doi.org/10.1016/S1369-7021\(06\)71693-5](https://doi.org/https://doi.org/10.1016/S1369-7021(06)71693-5)



## CHAPTER 3

# DISSOLUTION MECHANISM OF MGO THIN FILM SHIELDING LAYER IN TUNNELING MAGNETORESISTANCE HARD DISK DRIVE READ HEAD

### 3.1 Introduction

As discussed in **chapter 1** the dissolution of a magnesium oxide thin film results in material loss as well as changes in the film properties. The dissolution mechanism and dissolution rates in thin films, especially MgO thin film shielding layers of MTJs devices, are not yet well understood. In this chapter, MgO thin film was exposed to room temperature DI water for 2, 4, 6, 8, 10, and 15 hours, and the water's electrical conductivity was measured by using an EC meter. The quantity of magnesium dissolved in water was determined by flame AAS, and the change in surface roughness and surface morphology was investigated by using atomic force microscopy (AFM) and scanning electron microscopy (SEM). These results were applied to the mathematical model of the dissolution rate of magnesium oxide as a function of time. The model can be used to predict material loss during the production process and identify promising candidates for manufacturing.

This chapter is divided into the following sections: Section 3.2 presents the experimental procedure and instruments used in this study; Section 3.3 reports the data obtained using a variety of analysis techniques, including FIB-SEM cross-sectional and AFM microscopy (section 3.3.1), electrical conductivity (section 3.3.2), ellipsometry (section 3.3.3), and XPS chemical analysis (section 3.3.4). Section 3.3.5 proposes a model for the MgO thin film's dissolution in water. Finally, section 3.4 brings this chapter to a conclusion.

### 3.2 Experimental procedure

Specially sputtered 50 nm MgO thin film shielding insulators (i.e., for TMR sensors of HDD) on silicon substrates (provided by Western Digital, LLC, Fremont, CA, US) were cut into 15 mm × 15 mm coupons for experimental flexibility. These samples

were fixed to custom-built test cells (Figure 3.1). The surface area of the MgO films exposed to the solvent was controlled by a 10 mm diameter O-ring fixed to the test cell. Thus, only the encircled film surface was exposed to the 20 mL of DI water, allowing for good control of the environment and the properties of the solution.

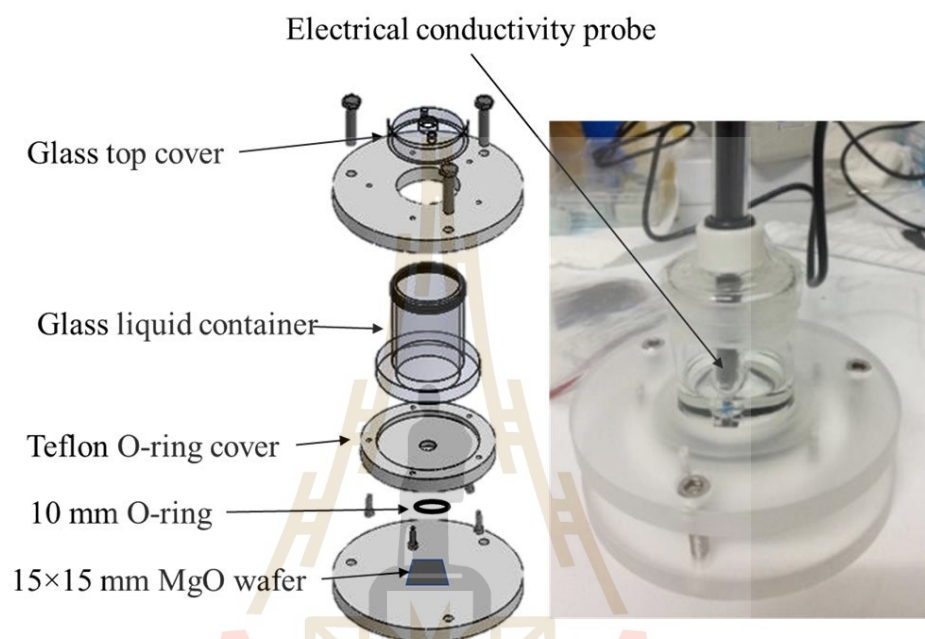


**Figure 3.1** Schematic view (left) and photograph (right) of the custom-built test cell.

The EC measurements of the samples as a function of immersion time were carried out at room temperature using an electrode linked to a data acquisition system (Lutron CD-4319SD). The EC data were acquired at a rate of 6 samples per minute and stored in an SD card. A PinAAcle-900F (PerkinElmer, Germany) atomic absorption spectrometer (AAS) was used to determine the magnesium (Mg) concentration in the dissolved solution. Tapping mode AFM (XE-120 Park Systems, scan frequency 0.2 Hz, 512 lines) was used to scan  $5 \times 5 \mu\text{m}^2$  sample areas. AFM images were analyzed by using XEI software (Park Systems) to extract the roughness and particle size information from the sample surface. Focused ion beam-SEM (FIB-SEM) measurements (Auriga dual-beam FIB-SEMM, Zeiss) were used to investigate the topography and microstructures of the surface (SE detector, 5 kV) as well as the cross-sections (Gallium Ion source,

5 kV). The processing of the SEM images using ImageJ (NIH Image) and thickness measurements using an ellipsometer (M-2000, JA Woollam) was used to extract the  $\text{Mg}(\text{OH})_2$  cluster sizes and left-over film profiles, respectively. X-ray photoelectron spectroscopy (XPS) spectra were obtained using a commercial PHI VersaProbe III XPS (ULVAC-PHI, Inc.). The source was monochromatic Al  $K\alpha$  radiation (1486.6 eV) and a pass energy of 23.5 eV was used. The analysis of the XPS spectra was performed using CasaXPS (Casa Software Ltd).

### 3.3 Results and discussions

#### 3.3.1 AFM surface roughness

When the MgO thin film was in contact with water, reactions such as hydration, dissolution, and precipitation occurred immediately. These reactions affected the physical properties of the thin film surface. Figure 3.2 (a) and (f) represent the AFM image of the surface roughness and the topographic SEM image of the MgO film surface after immersion in DI water for 2 hours, respectively. The hydration reaction is initiated as tiny groups of 50 nm hydration clusters on the film surface. This indicates the presence of a hydroxide reaction occurred in some areas on the thin film surface. Immersion of the MgO films for 4 hours resulted in the expansion of hydration clusters to a wider area and larger  $\text{Mg}(\text{OH})_2$  clusters with a size of approximately 80-100 nm. This indicated that the hydration process had covered the entire exposure area, resulting in an increase in surface roughness to 1.9 nm, as shown in Figure 3.2 (b) and (g). After 6 hours of immersion, the  $\text{Mg}(\text{OH})_2$  cluster sizes increased to 200 nm, and some parts of the film peeled off at approximately  $0.5\text{-}1\text{ nm}^2$ , which is a great indicator that the MgO thin film has begun to dissolve during this period, as -shown in Figure 3.2(c) and (h). With an immersion time of 10 hours, the AFM micrograph shows the surface roughness was increased to a maximum of 3.7 nm. (Figure 3.2(d)). The SEM image (Figure 3.2(i)) reveals the increased peeling of the surface film, leaving behind deeper areas and small traces of scattered holes spread throughout the film. After 15 hours of immersion, the precipitated hydroxide filled in holes caused by peeling, reducing roughness to 2.1 nm. (Figure 3.2(j)) and hydroxide precipitated all over the film, increasing the size of hydroxide clusters to about 500 nm (Figure 3.2(e)),

The surface of the MgO layer was almost insoluble due to Mg(OH)<sub>2</sub> precipitation because the Mg(OH)<sub>2</sub> layer possibly acts as a protective layer that blocked further dissolution. Figure 3.3 is a plot of the Mg(OH)<sub>2</sub> cluster size as a function of dissolution time to compare the surface roughness measured from the AFM pictures to the cluster size of the hydroxide formed on the film surface, measured using ImageJ software to illustrate how the film surface morphology changes over time when immersed in water. The Mg(OH)<sub>2</sub> cluster size increases with dissolution time due to the increasing aggregation of hydroxide precipitation over time. On the other hand, the film roughness increases initially with dissolution times of up to 10 hours, then decreased at 15 hours of dissolution time. These observations suggest that Mg<sup>2+</sup> ions from the MgO thin film dissolved in the first phase. After 10 hours, Mg(OH)<sub>2</sub> clusters nearly covered the entire surface area of the dissolved film, which inhibited the further dissolution of the MgO film. The roughness of the film surface decreases as the Mg(OH)<sub>2</sub> coverage becomes more universal.

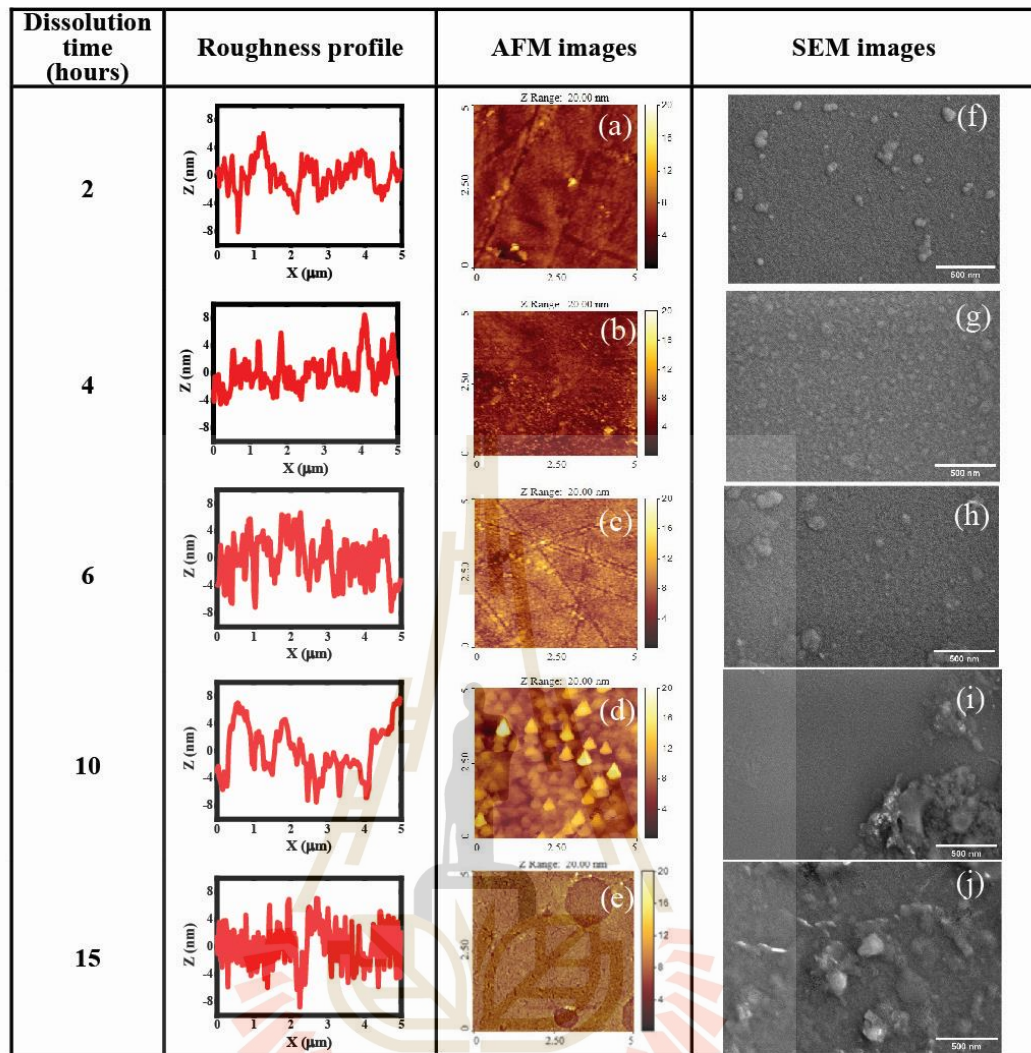
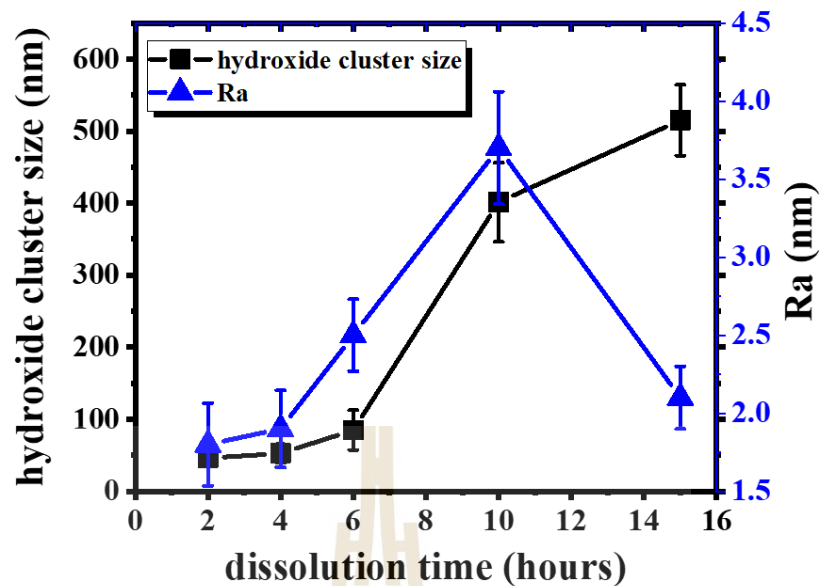


Figure 3.2 (a)–(e) AFM images at  $5 \times 5 \mu\text{m}$  scan size and (f)–(j) SEM images at  $\times 50000$  magnification on MgO dissolved surfaces in deionized water for 2, 4, 6, 10, and 15 hours respectively.



**Figure 3.3** Film roughness (Ra) and  $Mg(OH)_2$  cluster size on MgO thin film as a function of dissolution time in deionized water derived from AFM images of the surface.

### 3.3.2 Electrical conductivity (EC)

The solubility of the MgO thin film depends on the dissolution time. The EC meter was used to measure the concentration of MgO dissolved in water. Since the EC has increased with the amount of  $Mg^{2+}$  in the DI water, the change of the EC as a function of time is correlated to the dissolution of MgO in DI water. Figure 3.4 is the electrical conductivity-dissolution time (ECT) curve which is extracted by using a mathematical model based on the first-order rate law (Atkins & de Paula, 2010) and the multi-rate model by using dynamic fitting (Xing et al., 2018) of the EC versus dissolution time plot.

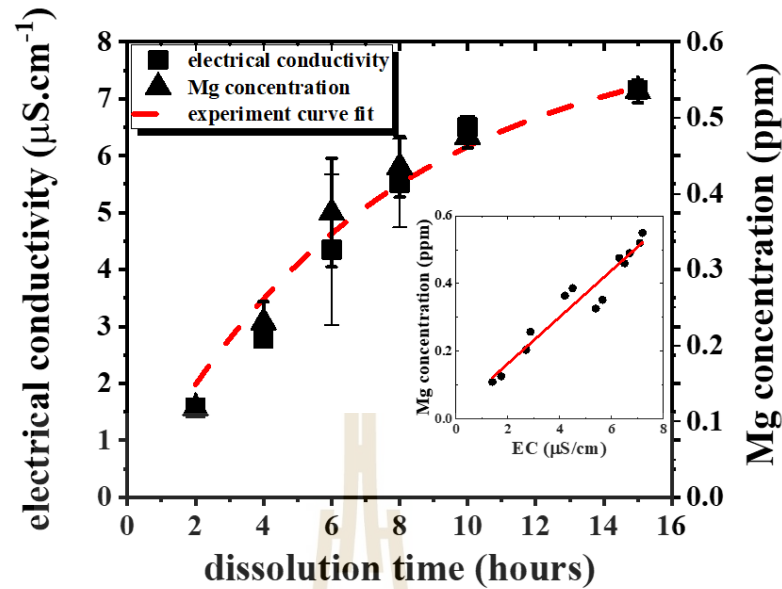


**Figure 3.4** Electrical conductivity (EC) and Mg concentration as a function of dissolution time. The Red dashed line is the curve fitting to the experimental data. The inset depicts the linear relationship between Mg concentration and EC.

A nonlinear regression curve (first-order kinetics) representing the behavior of the EC (measured in micro siemens per centimeter:  $\mu\text{S}\cdot\text{cm}^{-1}$ ) of MgO dissolution as a function of dissolution time,  $t$ , (measured in hour) can be expressed by Equation 3.1:

$$EC = EC_{\max} (1 - e^{-kt}) \quad (3.1)$$

Where  $EC_{\max}$  is the maximum electrical conductivity, and  $k$  is the reaction constant. The extracted curve fitting parameters are as follows:

$$EC = 8.25(1 - e^{-0.14t}) \quad (3.2)$$

As measured by atomic absorption spectroscopy (AAS), the concentration of  $\text{Mg}^{2+}$  dissolved in DI water increases as a function of time. The inset in Figure 3.4 is a plot of the  $\text{Mg}^{2+}$  concentration in solution versus EC during the dissolution reaction.

The calibration curve is linear over a wide range of  $Mg^{2+}$  concentration. The relationship between Mg concentration obtained from AAS and EC is given in Equation 3.3:

$$[Mg] = 0.07EC \quad (3.3)$$

Where EC is measured in  $\mu S/cm$  while  $[Mg]$  is Mg concentration measured in mg/L. By combining Equations (3.2) and (3.3), the Mg concentration as a function of time can be calculated with the following equation:

$$[Mg] = 0.58(1 - e^{-0.14t}) \quad (3.4)$$

The volume of MgO thin film that is dissolved in DI water is  $1.571 \times 10^{-5} \text{ cm}^3$  and the mass loss fraction of Mg from the MgO density ( $3.51 \text{ g/cm}^3$ ) is  $3.391 \times 10^{-5} \text{ g}$ . If this entire amount is dissolved in water, the maximum  $[Mg]$  in this experiment is 1.69 mg/L. From Equation 3.3, the percentage of mass loss can be calculated with the following equation:

$$\% \text{ mass loss} = 31.95(1 - e^{-0.14t}) \% \quad (3.5)$$

### 3.3.3 Ellipsometry

We can estimate the film thickness dissolved in DI water as a function of time from Equation 3.4. The comparison between the experimental measurements and model calculations of  $[Mg]$  versus dissolution time is summarized in The solubility of the MgO thin film depends on the dissolution time. The EC meter was used to measure the concentration of MgO dissolved in water. Since the EC has increased with the amount of  $Mg^{2+}$  in the DI water, the change of the EC as a function of time is correlated to the dissolution of MgO in DI water. Figure 3.4 is the electrical conductivity-dissolution time (ECT) curve which is extracted by using a mathematical model based on the first-order rate law (Atkins & de Paula, 2010) and the multi-rate model by using dynamic fitting (Xing et al., 2018) of the EC versus dissolution time plot.



**Table 3.1** Comparison of MgO mass loss from the experimental AAS results and with dissolution model calculations for various time scales.

Sample no.	Dissolution time (hour)	Mg concentration, [Mg]		Mass loss	
		Experiment	Calculated	Experiment	Calculated
		(mg/L)	(mg/L)	(%)	(%)
1	2	0.12	0.14	8.38	7.80
2	4	0.23	0.25	14.72	13.70
3	6	0.38	0.33	19.50	18.16
4	8	0.38	0.39	23.12	21.53
5	10	0.48	0.44	25.86	24.07
6	15	0.54	0.51	30.12	28.04

However, the remaining MgO film thickness, measured using an ellipsometer after 10 hours in DI water (Figure 3.5), revealed that the dissolution pattern is not cylindrical, but rather semicircular. The film thickness gradually decreased from the O-ring edge to the center of the area exposed to the water. The FIB-SEM cross-section images of the Si substrate/MgO thin film interface at different locations after 10 hours of exposure to DI water corroborated the thickness measurement from the ellipsometer. Figure 3.5 (b) is the SEM image of the MgO surface located outside the O-ring, which corresponds to the area of MgO not exposed to DI water. The MgO film thickness in this location is 60 nm, similar to that of the as-received sample. Figure 3.5(c) shows the MgO cross-section surface located near the edge of the O-ring and inside the dissolution area. The massive agglomerations of particles are expected to be Mg(OH)<sub>2</sub> clusters (Alavi & Morsali, 2010; Hwan Eun et al., 2003). The film thickness in this location decreased to 44 nm. Figure 3.5(d) shows the MgO cross-section surface located at the center of the dissolution area. The surface is rough, with an increasing number of particle clusters. The thickness further decreased to 37 nm.

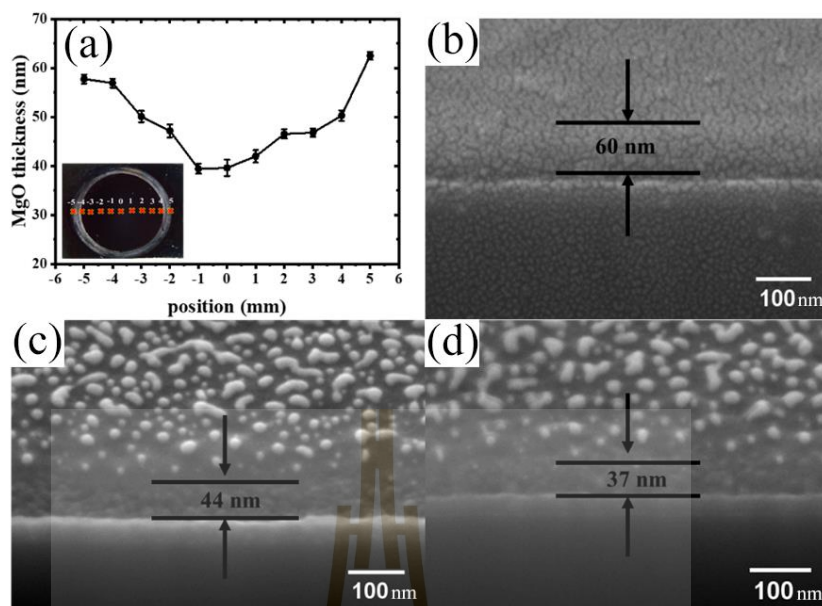


**Figure 3.5** (a) Thickness profile of the MgO thin film after dissolution, as measured by ellipsometry. (b-d) SEM-FIB cross section of the film (b) outside the exposed area, (c) inside the exposed area (near O-ring), and (d) at the center of the exposed area.

### 3.3.4 XPS chemical analysis

The films after different amounts of dissolution times were studied using SEM and XPS to confirm the coverage of the precipitated  $\text{Mg}(\text{OH})_2$  clusters over the MgO film surfaces. Figure 3.6(a) and (b) are SEM micrographs showing MgO film morphologies before and after dissolution. Before being exposed to the DI water, the films have smooth surfaces of uniformly distributed grains. After DI water exposure, the film morphology changed as a function of the dissolution time. Figure 3.6(c) and (d) show the O 1s XPS spectra of the MgO films before and after exposure to DI water. The pristine MgO films exhibited O 1s binding energy at 530.5 eV. After the MgO thin film was immersed in DI water for 10 hours, there was a 2 eV red shift in the O 1s binding energy spectra, which indicates that some of the oxygen is present in the form of hydroxide (Liu et al., 1998). The deconvolution of the O 1s spectrum (Figure 3.6(c)) into two peaks advocates that the peak at 530.1 eV corresponds to the MgO

component and the peak at 532.1 eV corresponds to the precipitated  $\text{Mg}(\text{OH})_2$  component (M. Santamaria et al., 2007). For the present work, the XPS data were only used to qualitatively identify the species found at the surface to be mainly  $\text{Mg}(\text{OH})_2$ .

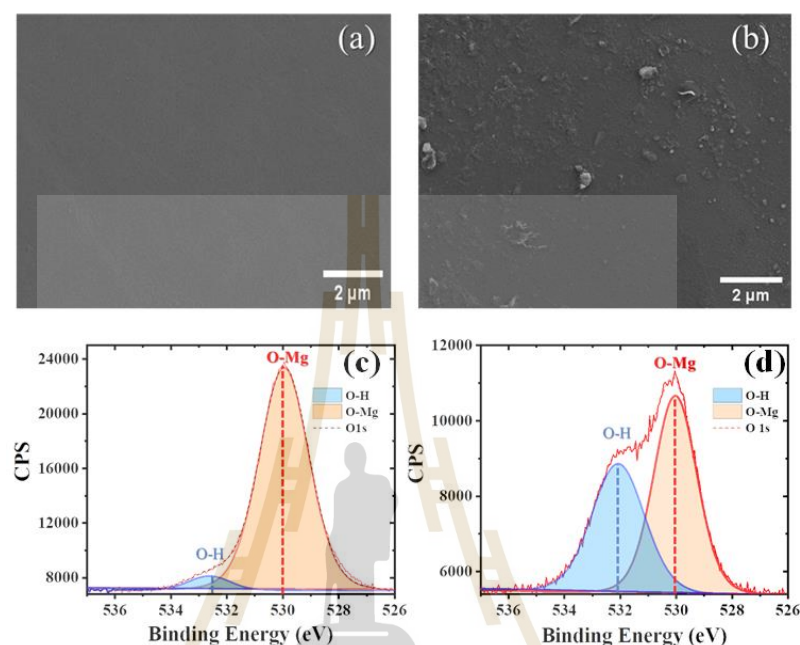


**Figure 3.6** (a,b)SEM micrographs and (c,d) O 1s XPS spectra of as-received MgO (a and c, respectively), and MgO immersed in deionized water for 10 hours (b and d, respectively).

### 3.3.5 Dissolution mechanism of MgO

The dissolution mechanism of MgO thin film can be explained by the dissolution and precipitation reactions as shown in Figure 3.7. When MgO was exposed to water, the water molecule,  $\text{H}_2\text{O}$ , deprotonated to become a hydroxide ion ( $\text{OH}^-$ ). Consequently, formed from the self-ionization of  $\text{H}_2\text{O}$ , the hydrogen nucleus ( $\text{H}^+$ ) immediately protonated MgO to form  $\text{MgOH}^+$  as described in Equation 3.6. After that, the negatively charged  $\text{OH}^-$  ions from the water were attracted to the positively charged  $\text{MgOH}^+$  ions on the surface where they were adsorbed to form  $\text{MgOH}^+\cdot\text{OH}^-$ , as described in Equation 3.7. Equation 3.8 describes the dissolution of the MgO film into  $\text{Mg}^{2+}$  and  $\text{OH}^-$  ions dissolved into the water. The amount of  $\text{Mg}^{2+}$  in the solution

was associated with material loss from the film as it was continuously dissolved. Equation 3.9 describes how the concentration reaches the saturation point:  $Mg(OH)_2$  precipitated and formed protective layer, resulting in a lower rate of  $MgO$  dissolution. In addition, the precipitation of  $Mg(OH)_2$  also affected the surface roughness of the film, resulting in thin film surface microstructures based on the dissolution time.

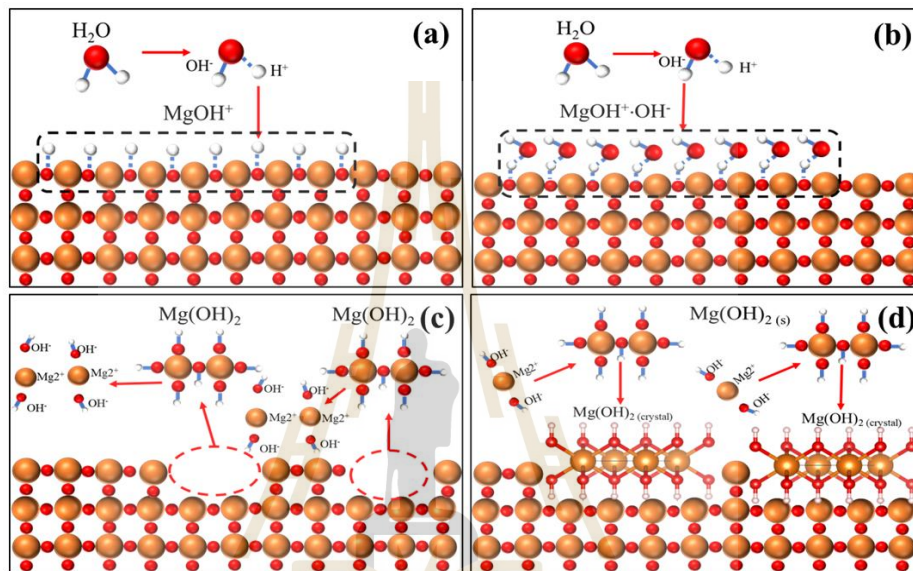
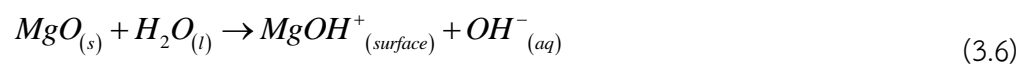


**Figure 3.7** The mechanism of  $MgO$  dissolution (a) surface is protonated by  $H^+$  ions from water ( $H_2O$ ), (b)  $OH^-$  negative ions absorbed on the surface to form  $MgOH^+ \cdot OH^-$ , (c) dissolution of the  $MgO$  film into  $Mg^{2+}$  and  $OH^-$  ions, and (d) magnesium hydroxide ( $Mg(OH)_2$ ) cluster.

The equations associated with the dissolution mechanism of  $MgO$  thin films with DI water are as follows (Birchal et al., 2001; Holt et al., 1997; Kato et al., 1996; Rocha et al., 2004):

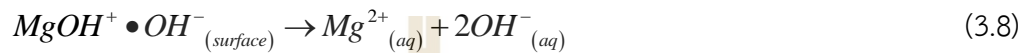
- 1)  $MgO$ -alkaline oxide acts as an electron donor in water:



2)  $\text{OH}^-$  anions are adsorbed on the positively charged surface:



3)  $\text{OH}^-$  anions are desorbed from the surface and release the  $\text{Mg}^{2+}$  ions into the solution:



4) Ion concentration in solution reaches at the supersaturation point, which the hydroxide starts to precipitate on the oxide surface:



### 3.4 Conclusions

In summary, the dissolution of the commercial MgO thin film used as a magnetic insulator layer after exposure to DI water was investigated, to demonstrate the challenge in the production process of read/write heads for magnetic HDDs. When the MgO thin film is exposed to DI water, a hydration reaction occurs rapidly, which can cause physical and chemical damage to the film and affect device performance. We demonstrated that the amount of dissolved MgO film can be measured by the EC, which is linearly proportional to the amount of  $\text{Mg}^{2+}$  in the solution. The proposed model of MgO dissolution shows that the precipitated  $\text{Mg}(\text{OH})_2$  clusters form a protective layer on the film surface which eventually inhibits the dissolution process. Using film thickness, roughness measurements, and XPS of MgO thin films after different DI water exposure time, we confirmed that our prediction model was in agreement very well with the experimental results. The precipitated  $\text{Mg}(\text{OH})_2$  cluster sizes increase with DI water exposure times, while the film roughness initially increases as  $\text{Mg}(\text{OH})_2$  clusters precipitate, but then decreases as the  $\text{Mg}(\text{OH})_2$  coverage becomes more universal. The experimental measurements of MgO mass loss and prediction

model are within 20% of each other. The model provides a fundamental understanding of the underlying mechanisms of MgO thin film damage during the hydration process. Our simple experimental setup enables the rapid identification of suitable MgO thin film candidates for the HDD read/write heads, and the possibility of optimizing the manufacturing process of such devices.

### 3.5 References

- Alavi, M. A., & Morsali, A. (2010). Syntheses and characterization of Mg(OH)<sub>2</sub> and MgO nanostructures by ultrasonic method. *Ultrasonics Sonochemistry*, 17(2), 441-446. doi:10.1016/j.ultsonch.2009.08.013
- Amaral, L. F., Oliveira, I. R., Bonadia, P., Salomão, R., & Pandolfelli, V. C. (2011). Chelants to inhibit magnesia (MgO) hydration. *Ceramics International*, 37(5), 1537-1542. doi:10.1016/j.ceramint.2011.01.030
- Atkins, P., & de Paula, J. (2010). *Atkins' Physical Chemistry*: OUP Oxford.
- Birchal, V. S., Rocha, S. D. F., Mansur, M. B., & Ciminelli, V. S. T. (2001). A simplified mechanistic analysis of the hydration of magnesia. *The Canadian Journal of Chemical Engineering*, 79(4), 507-511. doi:10.1002/cjce.5450790406
- Carrasco, E., Brown, M. A., Sterrer, M., Freund, H.-J., Kwapien, K., Sierka, M., & Sauer, J. (2010). Thickness-Dependent Hydroxylation of MgO(001) Thin Films. *The Journal of Physical Chemistry C*, 114(42), 18207-18214. doi:10.1021/jp105294e
- Haginoya, C., Hatatani, M., Meguro, K., Ishikawa, C., Yoshida, N., Kusakawa, K., & Watanabe, K. (2004). Side-shielded tunneling magnetoresistive read head for high-density recording. *IEEE Transactions on Magnetics*, 40(4), 2221-2223. doi:10.1109/TMAG.2004.829157
- Holt, S. A., Jones, C. F., Watson, G. S., Crossley, A., Johnston, C., Sofield, C. J., & Myhra, S. (1997). Surface modification of MgO substrates from aqueous exposure: an atomic force microscopy study. *Thin Solid Films*, 292(1), 96-102. doi:10.1016/S0040-6090(96)08955-9

- Hwan Eun, J., Heon Lee, J., Gil Kim, S., Yoon Um, M., Young Park, S., & Joon Kim, H. (2003). The protection of MgO film against hydration by using Al<sub>2</sub>O<sub>3</sub> capping layer deposited by magnetron sputtering method. *Thin Solid Films*, *435*(1), 199-204. doi:10.1016/S0040-6090(03)00362-6
- Jones, C. F., Reeve, R. A., Rigg, R., Segall, R. L., Smart, R. S. C., & Turner, P. S. (1984). Surface area and the mechanism of hydroxylation of ionic oxide surfaces. *Journal of the Chemical Society, Faraday Transactions 1: Physical Chemistry in Condensed Phases*, *80*(10), 2609-2617. doi:10.1039/F19848002609
- Kato, Y., Yamashita, N., Kobayashi, K., & Yoshizawa, Y. (1996). Kinetic study of the hydration of magnesium oxide for a chemical heat pump. *Applied Thermal Engineering*, *16*(11), 853-862. doi:10.1016/1359-4311(96)00009-9
- Liu, P., Kendelewicz, T., Brown, G. E., & Parks, G. A. (1998). Reaction of water with MgO(100) surfaces. Part I: Synchrotron X-ray photoemission studies of low-defect surfaces. *Surface Science*, *412-413*, 287-314. doi:10.1016/S0039-6028(98)00444-0
- Rocha, S. D. F., Mansur, M. B., & Ciminelli, V. S. T. (2004). Kinetics and mechanistic analysis of caustic magnesia hydration. *Journal of Chemical Technology & Biotechnology*, *79*(8), 816-821. doi:10.1002/jctb.1038
- Santamaria, M., Di Quarto, F., Zanna, S., & Marcus, P. (2007). Initial surface film on magnesium metal: A characterization by X-ray photoelectron spectroscopy (XPS) and photocurrent spectroscopy (PCS). *Electrochimica Acta*, *53*(3), 1314-1324. doi:10.1016/j.electacta.2007.03.019
- Xing, Z., Bai, L., Ma, Y., Wang, D., & Li, M. (2018). Mechanism of Magnesium Oxide Hydration Based on the Multi-Rate Model. *Materials*, *11*(10), 1835. doi:10.3390/ma11101835
- Zheng, Y. K., Han, G. C., Li, K. B., Guo, Z. B., Qiu, J. J., Tan, S. G., Wu, Y. H. (2006). Side Shielded TMR Reader With Track-Width-Reduction Scheme. *IEEE Transactions on Magnetics*, *42*(10), 2303-2305. doi:10.1109/TMAG.2006.880463

## CHAPTER 4

### EFFECT OF ANNEALING ATMOSPHERE ON PHYSICAL AND ELECTRICAL PROPERTIES OF MgO THIN FILM IN TUNNELING MAGNETORESISTANCE SENSOR

#### 4.1. Introductions

In **chapter 3** was discussed the effects of MgO thin films that have been exposed to water and dissolved in the hard disk drive manufacturing process. In this chapter MgO thin films were annealed to remove moisture and residual stress from the films at various temperatures (250, 350, and 450 °C) and various gas atmospheres (Ar, N<sub>2</sub> and normal air) as well as investigate the combined effects of temperature and gas atmospheres annealing on the morphological, chemical, and electrical properties of MgO thin films which were used as a shielding insulator in HDD reader heads. The results were analyzed by using atomic force microscopy (AFM), X-ray photoelectron spectroscopy (XPS), focused ion beam scanning electron microscopy (FIB-SEM), and source meter.

This chapter is divided into the following sections: Section 4.2 describes the experimental procedure used in this study. Section 4.3 presents the results and discussions on data obtained by using a variety of analysis techniques, section 4.3.1 presents surface roughness analysis by AFM, section 4.3.2 presents FIB-SEM cross-sectional image analysis, section 4.3.3 presents electrical properties by measuring the dielectric breakdown voltage, section 4.3.4 presents chemical composition analysis by XPS, section 4.3.5 presents and grain expansion mechanism. Finally, section 4.4 is the conclusion of this chapter.



## 4.2. Experimental procedure

In this work, 50 nm thick MgO films on 10 nm Ruthenium (Ru) on silicon (Si) substrates (provided by Western Digital, LLC, Fremont, CA, US) were used to study the annealing in different environments. These MgO films were annealed at 250, 350, and 450 °C with Argon (Ar), Nitrogen (N<sub>2</sub>) and normal air atmospheres using a custom-built in-house gas chamber (as shown in Figure 4.1 (a)). The samples were kept at the bottom of two cups and allowed the gases to enter the respective gas chamber. The custom-built chamber was kept in the oven and annealed at 250, 350 and 450 °C for 2 hours. The ramp-up and ramp-down rates of an oven were 5 °C/min. The gas inlets of the chamber were connected to the Ar and N<sub>2</sub> gases with a flow rate of 100 cm<sup>3</sup>/min. In the case of conventional air annealing, samples were annealed with a flow rate of 100 cm<sup>3</sup>/min by a conventional air pump. The actual image of the custom-built in-house gas chamber is shown in Figure 4.1 (b).

Tapping mode atomic force microscopy (AFM, XE-120 Park Systems, scan frequency 0.2 Hz, 512 lines) was used to investigate the surface roughness of the films, and the measured scan area was 5 × 5 μm<sup>2</sup>. AFM images were analyzed using XEI software (Park Systems) to extract the root mean square (RMS) roughness values. Focused ion-beam scanning electron microscopy (FIB-SEM, dual-beam, Auriga, SE detector, 5 kV, Zeiss) was used to determine the topographical information and cross-sectional images (Gallium Ion source, 5 kV). Additional research was carried out using X-ray photoelectron spectroscopy (XPS) at Beamline 3.2 of the Synchrotron Light Research Institute (SLRI) in Thailand to investigate MgO films' chemical composition and depth profile. The XPS measurement parameters are as follows: the survey spectrum was collected from 0 – 1400 eV with 1 eV energy step, 117.5 eV pass energy. High-resolution Mg 2p, O 1s, and Ru 3d spectra were acquired with a 0.1 eV energy step, a 23.5 eV pass energy, and five cycles. The depth profile analysis of the MgO thin films were sputtered using an in-situ argon ion (Ar<sup>+</sup>, 1 keV) source with 1 mA beam current, 2x2 mm<sup>2</sup> beam size, and a 10-minute per step size. The XPS spectra analysis was performed using the commercial software CasaXPS (Casa Software Ltd).

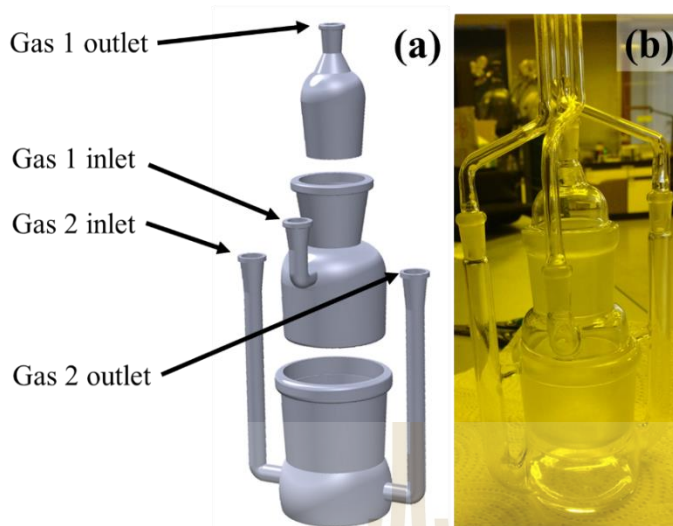


**Figure 4.1** (a) schematic representation of custom-built in-house annealing setup and (b) actual image of the annealing gas chamber.

In-house prepared circuits were used to measure the dielectric breakdown of MgO films. The schematic diagram of the dielectric breakdown measurement is shown in Figure 4.2. A 10 nm Gold (Au) electrode was deposited on both MgO film (as a top electrode of  $10 \times 10 \text{ mm}^2$ ) and on the Ru electrode (as a bottom electrode of  $2.5 \times 10 \text{ mm}^2$ ). The electrodes were connected to a voltage source unit (Keysight B2901A) to measure the current-voltage (I-V) curves.

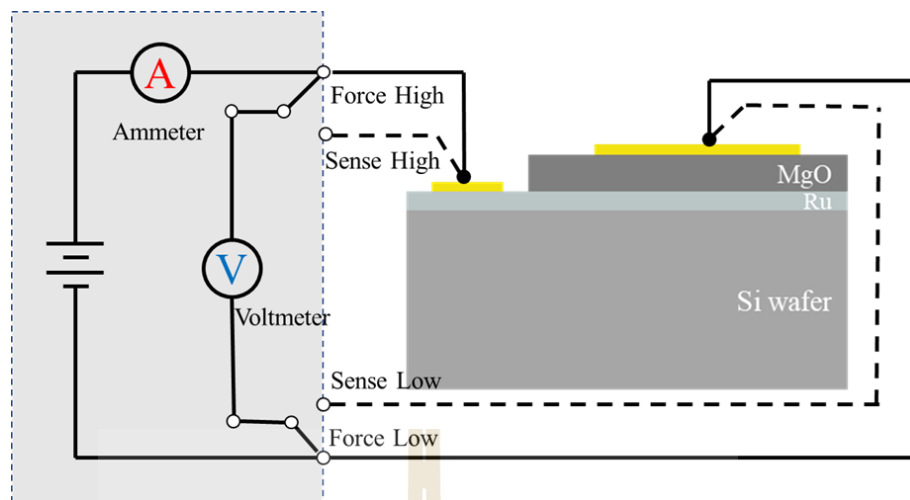


**Figure 4.2** a schematic diagram of the MgO thin film prepared for dielectric breakdown measurement

## 4.3. Results and discussions

### 4.3.1. AFM roughness

Figure 4.3 shows the topographic AFM images recorded over  $5 \times 5 \mu\text{m}^2$  of MgO thin films. The Ar gas annealing showed an increased RMS roughness value from 1.74 to 2.53 nm as the annealing temperature increased from 250 to 450 °C, as shown in Figure 4.3 (a-c). Similarly, the N<sub>2</sub> gas annealed MgO film RMS values are 2.47 and 4.10 and 3.61 nm, respectively, for 250, 350 and 450 °C, as shown in Figure 4.3 (d-f). The decreased film roughness with an increase in annealing temperature is related to grain growth and aggregation, creating a greater surface area (Mukhin et al., 2019). However, it seems to be RMS values are higher for air annealed samples, and the values are 2.82, 3.53, and 5.12 nm, respectively, for 250, 350 and 450 °C, as shown in Figure 4.3 (g-i). It is found that the surface roughness is increased with increasing temperature in all the gas environments. The maximum surface roughness is observed for air-annealed films at a higher temperature. This might be due to the grain growth effect in the MgO films, and this grain growth is maximum for air-annealed samples. High annealing temperatures lead to an increase in film thickness from grain growth, which can be the reason for the increase in surface roughness when the annealing temperature increases (Tolstova et al., 2016; Wang & Zhu, 2018).

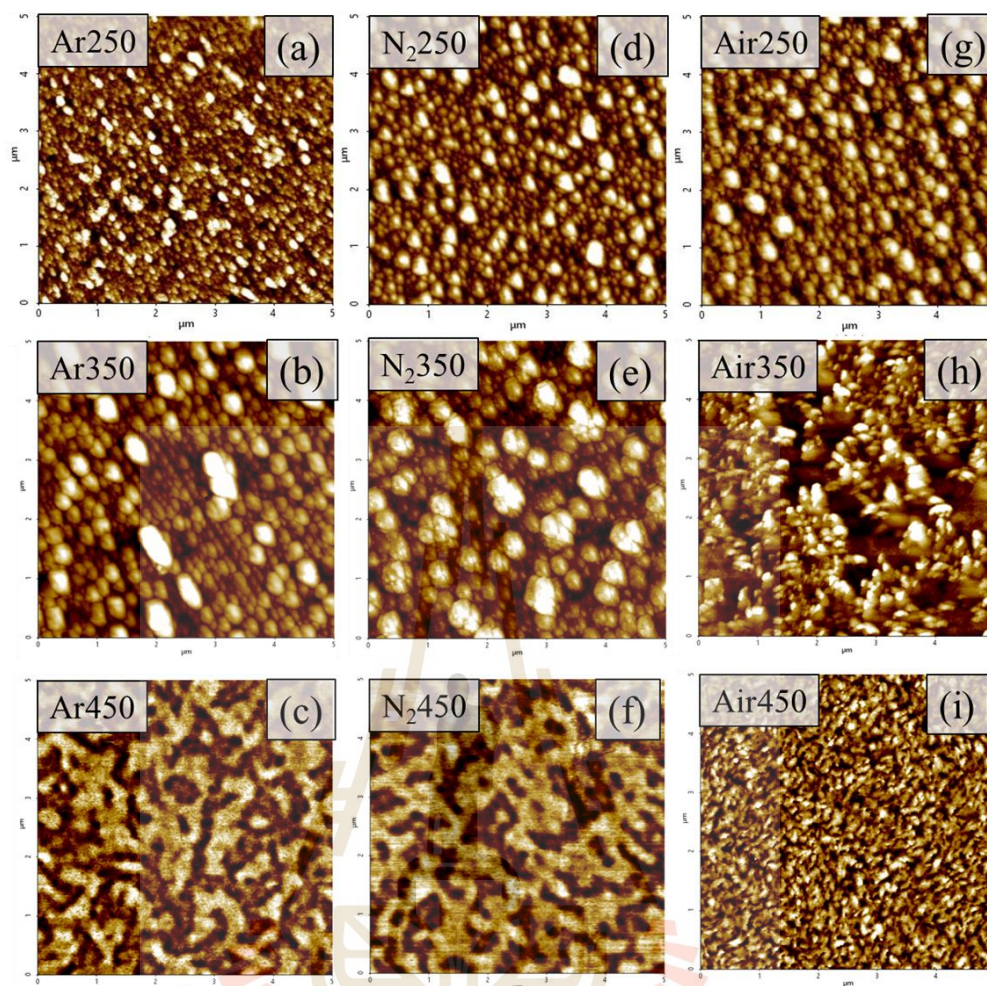
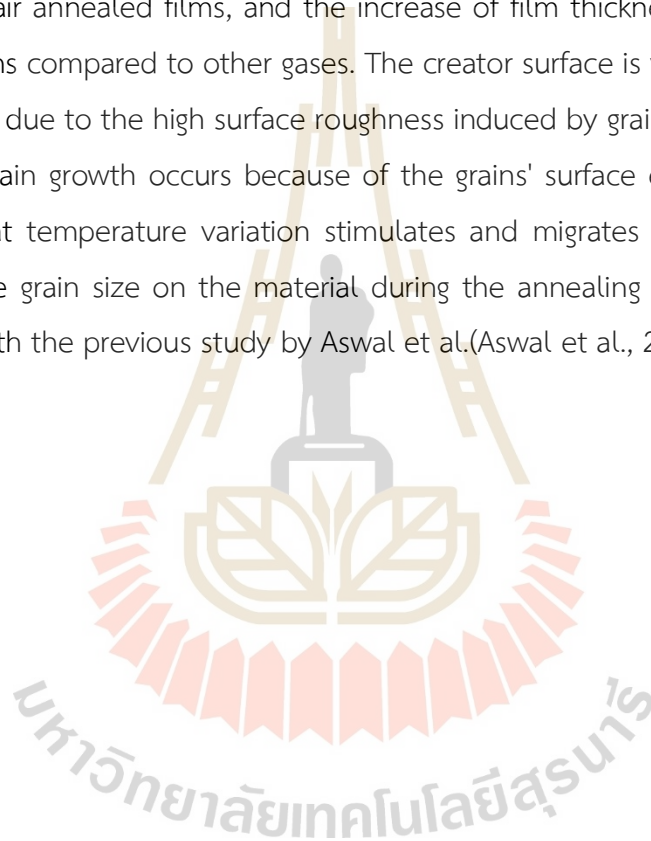


**Figure 4.3** surface roughness of MgO films at different gas atmospheric temperatures. Figures (a-c) depict the Ar gas annealing, figures (d-f) depict the N<sub>2</sub> gas annealing, and figures (g-i) depict the normal air annealing. Here annealing temperatures are 250, 350, 450 °C.

#### 4.3.2. FIB-SEM images

MgO film thicknesses were estimated from FIB-SEM cross-sectional images, as shown in Figure 4.4. Pristine MgO film showed a smooth surface, homogeneous, with an average film thickness of 49.58 nm, as shown in Figure 4.4 (a). The Ar gas annealed MgO film thickness values are 49.48, 49.61, and 47.98 nm, respectively, for 250, 350, and 450 °C, as shown in Figure 4.4 (b-d). Similarly, the N<sub>2</sub> gas annealed MgO film thickness values are 49.93, 55.43, and 51.01 nm, respectively, for

250, 350 and 450 °C, as shown in Figure 4.4 (e-g). However, when the MgO thin film was subjected to annealing under air containing atmosphere, the grain size of the film increased adversely. The thin film thicknesses of normal air annealed films are 47.09, 58.08, and 104.5 nm, respectively, for 250, 350 and 450 °C, as shown in Figure 4.4 (h-i). These experimental results are consistent with Lin et al. (Lin et al., 2005), which showed that high temperatures could promote grain boundary movement and agglomerate other grains during the annealing process. The increased film thickness is observed in air annealed films, and the increase of film thickness is very high for air annealed films compared to other gases. The creator surface is visible throughout the film, possibly due to the high surface roughness induced by grain growth or hydroxide formation. Grain growth occurs because of the grains' surface energy reduction. It is observed that temperature variation stimulates and migrates the grain boundaries, increasing the grain size on the material during the annealing process. The result is consistent with the previous study by Aswal et al. (Aswal et al., 2002).



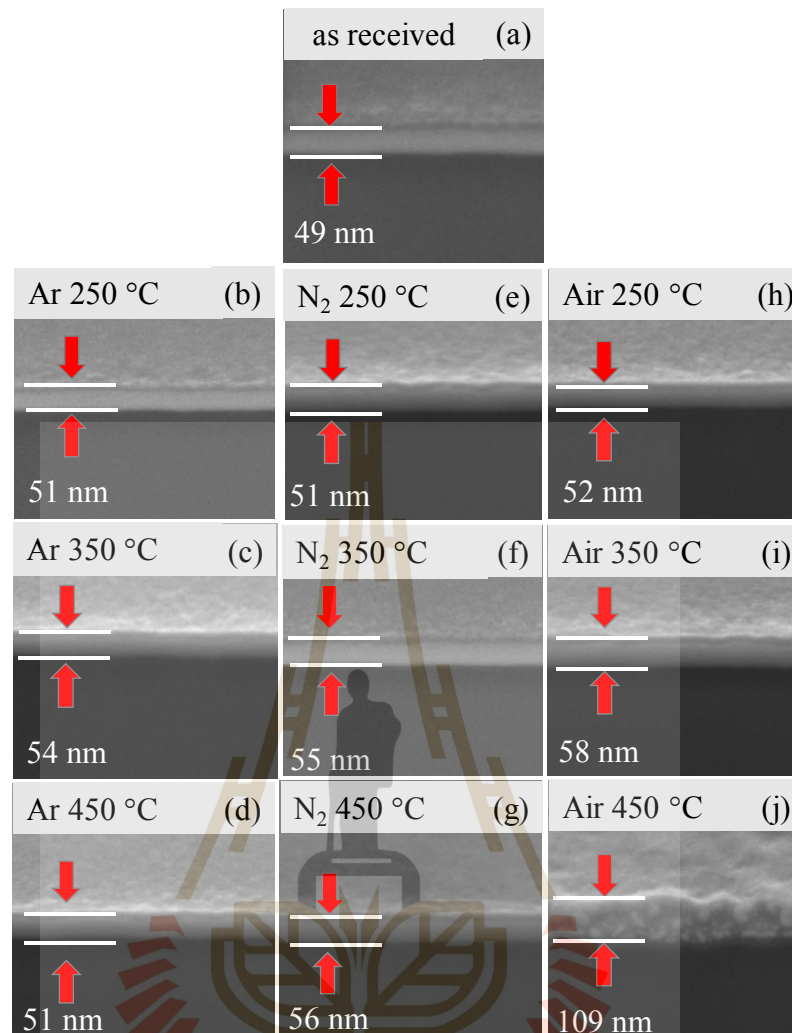


**Figure 4.4** SEM-FIB cross-section of (a) as-received, (b-d) argon, (e-g) nitrogen, and (h-j) normal air 250–450 °C samples, respectively.

### 4.3.3. Dielectric break down

Typically, the isotropic MgO has a critical field strength between 100 – 350 kV/cm, which means that 50 nm MgO film has the 0.25-1.75V critical field strength (Chen et al., 2009; Ho et al., 1997; Khan et al., 2008). As seen in Figure 4.5, the current-voltage (I-V) curves are measured for Ar, N<sub>2</sub> and air-annealed MgO films. When the voltage is low, the current is of few microamperes, and when the voltage reaches a certain threshold, a rapid rise in current indicates the onset of dielectric breakdown. This irreversible change in conductivity correlates to the thin film's hard dielectric

breakdown (Dimitrov et al., 2009). Figure 4.5 shows the as received film dielectric breakdown voltage at around 2.2 V, and consistent with the predicted value.

The Argon annealed sample breakdown voltages are 10.2, 8.4 and 7.2 V, respectively, for 250, 350, and 450 °C, as shown in Figure 4.5 (a). While nitrogen gas annealed film's dielectric breakdown voltage are 8.3, 7.2 and 5.5 V, respectively, for 250, 350, and 450 °C, as shown in Figure 4.5 (b). Similarly, the air annealed sample breakdown voltages are 8.2, 5.6 and 1.7 V, respectively, for 250, 350, and 450 °C, as shown in Figure 4.5 (c). The result showed that the breakdown voltage of the films decreased with increasing annealing temperature. The change in the dielectric breakdown voltage is due to the change in magnesium oxide film density caused by the reaction with oxygen and air humidity in the annealing atmosphere. As a result, the internal structure of the film was changed from MgO to Mg(OH)<sub>2</sub>, which reduced the dielectric strength of air-annealed thin film (Zahran et al., 2018). Therefore, compared to N<sub>2</sub> and air annealed samples at the same temperature, annealing in the Ar atmosphere exhibited higher breakdown voltages. This finding implies that a lower annealing temperature results in better film durability.



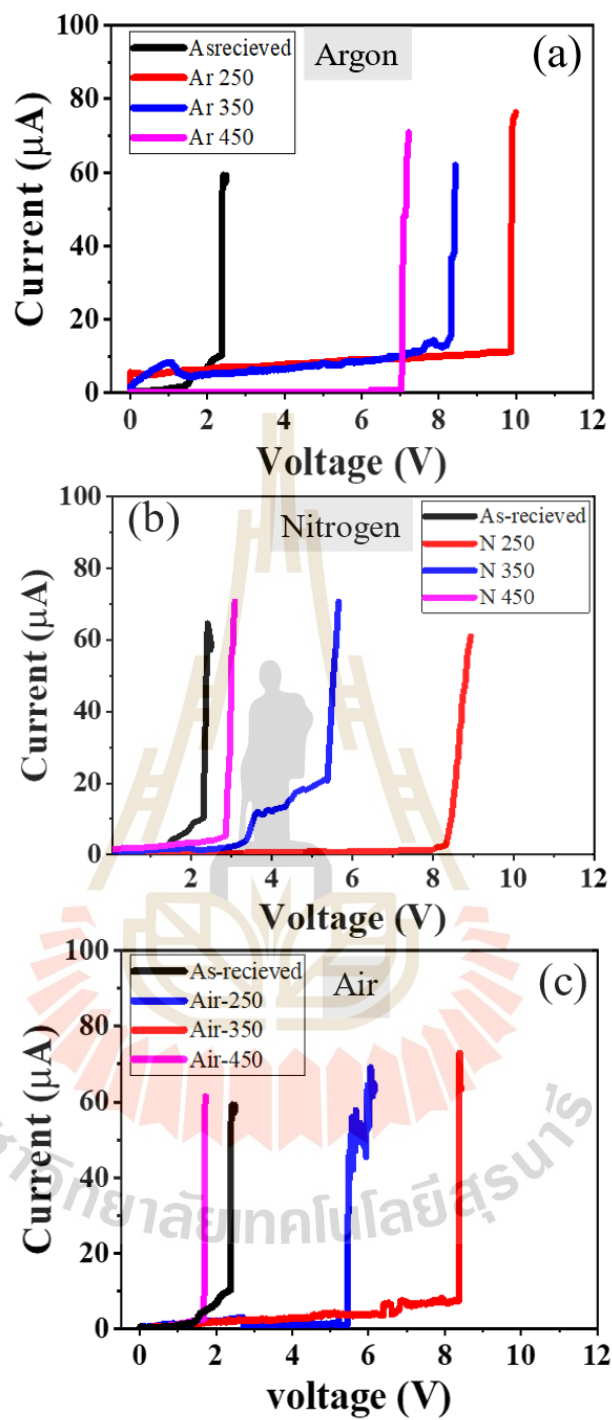


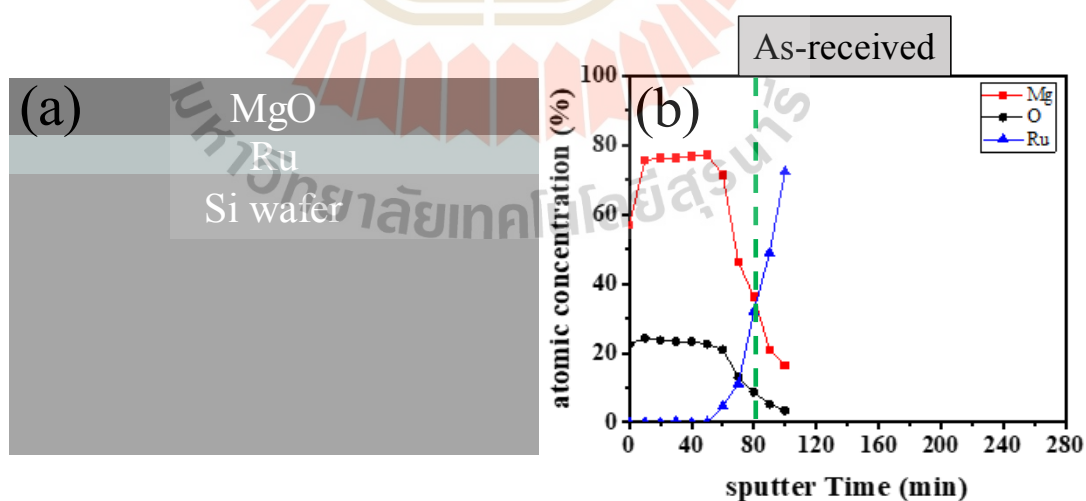
Figure 4.5 (a-c) I-V curve of the Ar, N<sub>2</sub> and normal air annealed MgO films. Current jump indicates the dielectric breakdown voltage.



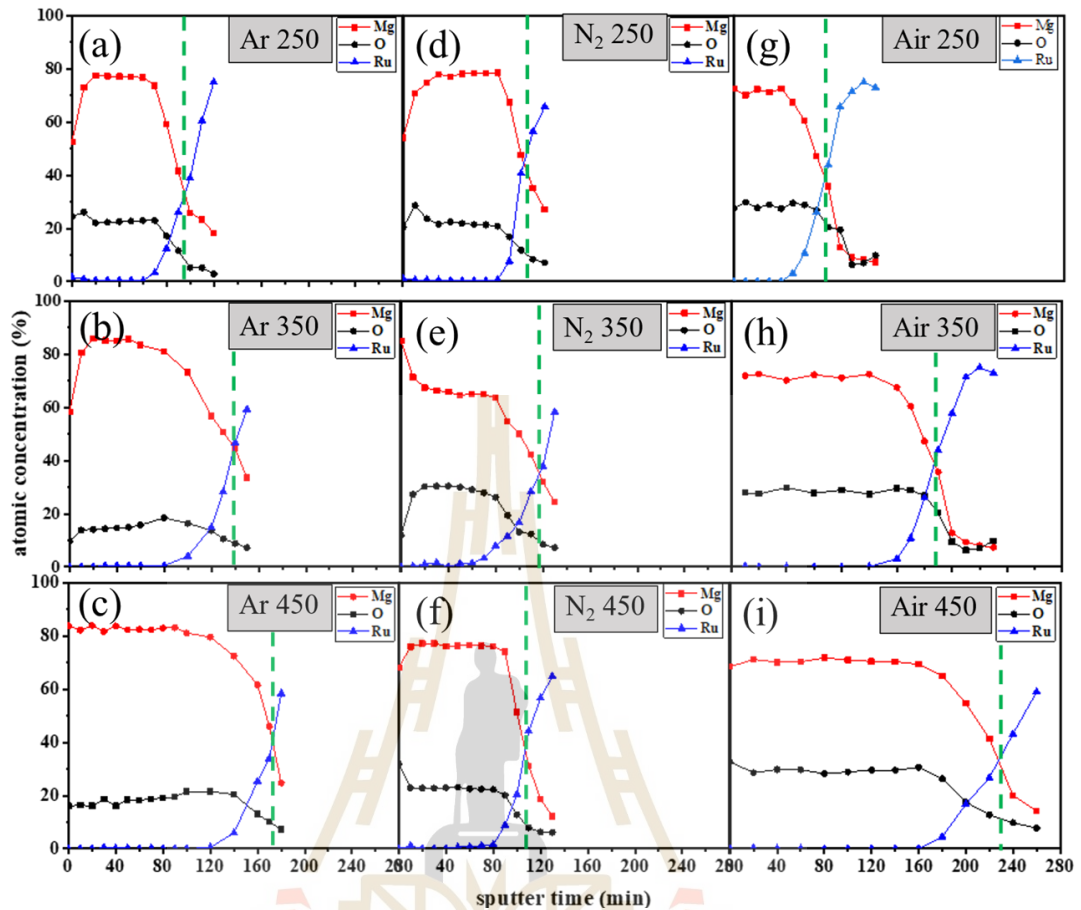
#### 4.3.4. Ion sputter etch rate

Figure 4.6 shows the schematic drawing of the pristine film's MgO layer structure and XPS depth profile. Pre-sputtering of MgO films was done for 10 min to remove the surface contamination. High-resolution XPS spectra were recorded, and the procedure continued until the Ru film layer reached. The Mg, O and Ru atomic concentrations significantly varied as the sputtering time increased (as shown in Figure 4.6 b).

The area under the O1s, Mg2p, and Ru3d peaks were plotted as a function of etching time. Initially, both Mg and O concentrations increased slightly (this might be due to surface impurities) and were further saturated for a certain period (this is due to the core MgO film content). As the sputtering time progressed further, both Mg and O concentrations dropped, and Ru (bottom electrode film) concentration rose sharply. This is due to the end of MgO film and starting of the bottom electrode layer. On average, the rate of MgO etching rate is 0.63 atoms/min. The sputtering rate was calculated by dividing the sputtering time by film thickness measured from FIB-SEM images. The detailed XPS analysis of MgO films was discussed in our previous publication (Kongtunmon et al., 2021).



**Figure 4.6** (a) Schematic drawing of MgO layer structure (b) XPS depth profile of as-received MgO/Ru/Si film to determine the atomic concentration of Mg as a function of film depth



**Figure 4.7** Ion depth profile of MgO thin film with different annealing environments. High-resolution peak intensity of Mg2p, O1s, and Ru3d as a function of etching time for the fresh sample, N<sub>2</sub> and Ar. Rising of the Ru peak intensity is used to calculate the etch

Different gas annealed MgO film depth profile results are shown in Figure 4.7. Ar gas annealed films depth profiles are shown in Figure 4.7 (a-c). As the annealing temperature increases, the sputter rate decreases in Ar gas annealed films. The sputtering rates of the annealed films are 0.53, 0.35, and 0.28 nm/min, respectively, for 250, 350 and 450 °C. The decrease in the sputter rate indicates that the film becomes stronger as the annealing temperature increases. This might be due to an increase in film density and crystallinity, which is consistent with the Oswald et al. (2020) (Oswald et al., 2020) result. The N<sub>2</sub> gas annealed film's depth profiles are shown

in Figure 4.7 (d-f). The sputtering rates of  $N_2$  gas annealed films are 0.54, 0.47, and 0.47 nm/min with increasing annealing temperatures from 250 to 350 and 450 °C, respectively. The sputtering rate slightly decreased and did not change much in  $N_2$  gas annealed films, and these sputter rates are comparable to Ar gas annealed films. It means that the annealing temperature does not influence much the film hardness. Figure 4.7 (g-i) shows the normal air annealed film depth profiles. The sputtering rates of air-annealed films are 0.56, 0.44, and 0.46 nm/min, respectively, for 250, 350, and 450 °C. The sputtering rate is decreased with increasing annealing temperature. However, the results of this experiment showed that increasing air annealing leads to an increase in thin film thickness. Therefore, variation in sputtering time is due to varying film thickness. However, the sputtering yield variation results from the varying film densities (Shulga, 2000). As film thickness increases, film density drops, impacting the sputtering rate. The higher the expansion of the thickness, the slower the sputtering rate.

#### 4.3.5. grain expansion mechanism

This study indicates that both gas environments and annealing temperatures influence the surface morphology, composition, and dielectric properties breakdown voltage of MgO films. Figure 4.8 shows the basic understanding and a schematic representation of the hydration reaction mechanism. MgO film easily reacts with the oxygen content in the atmosphere and initiates the hydration reaction within the film. Annealing temperature influences the oxygen content in the atmosphere and the hydration reaction rate. The oxygen content in Ar and  $N_2$  gases is significantly less; hence the observed less hydration reaction (in all the temperatures). However, oxygen content in the air is adequate to initiate the hydration reaction for all temperatures. The larger MgO grains create more voids between grain boundaries and allow the water molecules in the air (in the form of moisture) into the gaps. The primary reason for this phenomenon is the change in film thickness caused by the oxygen concentration of the air flowing through the annealing chamber, which results in oxygen gas diffusion and adsorption on the thin film's surface (Aswal et al., 2002; Sun et al., 2013).

Additionally, increasing annealing temperature increases the lattice constant of MgO, resulting in grain growth of MgO thin films (Diana et al., 2021; Singh & Chae, 2019; Singh et al., 2018). As a result, films annealed in the air have a lower

free carrier concentration than those annealed in inert gas. When annealing in an oxidant reduction environment, the grain boundaries act as carrier traps, creating a decrease/increase in carrier concentration (Nunes et al., 2001).

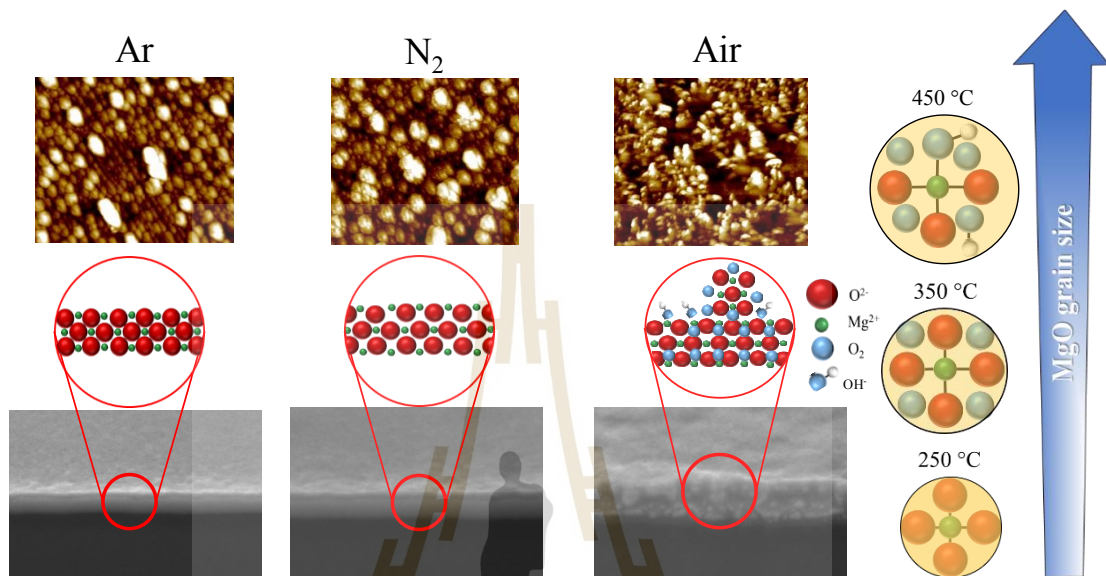


Figure 4.8 Mechanism of gas annealed MgO thin films grain expansion.

#### 4.4. Conclusions

In conclusion, MgO films are annealed at different temperatures in different gas environments to examine their physical and chemical properties. The MgO film thickness slightly increases when annealed in Ar and N<sub>2</sub> gases. However, the film thickness is drastically increased after air annealing. The reason behind the increase in film thickness is hydration reaction-assisted grain growth. Oxygen content in the Annealing environment is the main contender for the hydration reaction of MgO films. The maximum surface roughness of air-annealed films is due to the surface scatters that evolved due to drastic grain growth. The smooth surface of films is observed when annealed below 350 °C, and the roughness of the films increases after 450 °C. The FIB-SEM results revealed that film thickness increased twice of a pristine film when annealed air atmosphere at 450 °C. Although the film density decreases with the annealing temperature, the dielectric breakdown voltage is decreased as the

temperature increases. The argon-annealed film demonstrated the lowest reduction in dielectric breakdown voltage.

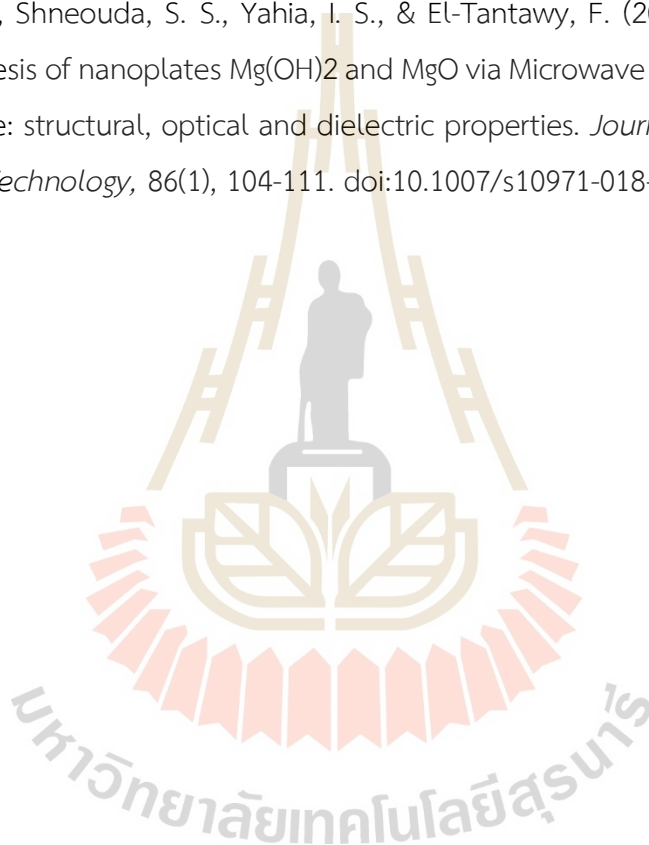
In contrast, the air-annealed thin film showed the most significant decrease in dielectric breakdown voltage, affecting the film's shielding performance and signal output quality of the hard disk reader heads. In addition, the Ar gas annealing can reduce residual stress and humidity in MgO thin films rather than using N<sub>2</sub> gas to prevent the film thickness expansion, film surface roughness, and reduction of dielectric strength of MgO thin films. The results provide information for the hard disk drives (HDDs) manufacturing process suitable for Ar gas annealing.

#### 4.5. References

- Aswal, D. K., Muthe, K. P., Tawde, S., Chodhury, S., Bagkar, N., Singh, A., Gupta, S. K., & Yakhmi, J. V. (2002). XPS and AFM investigations of annealing induced surface modifications of MgO single crystals. *Journal of Crystal Growth*, 236(4), 661-666. doi:[https://doi.org/10.1016/S0022-0248\(02\)00852-7](https://doi.org/10.1016/S0022-0248(02)00852-7)
- Diana, P., Saravanakumar, S., Prasad, K. H., Sivaganesh, D., Chidhambaram, N., Isaac, R. S. R., Alshahrani, T., Shkir, M., Aifaify, S., & Ali, K. S. S. (2021). Enhanced Photocatalytic Decomposition Efficacy of Novel MgO NPs: Impact of Annealing Temperatures. *Journal of Inorganic and Organometallic Polymers and Materials*, 31(7), 3027-3036. doi:10.1007/s10904-021-01896-4
- Fang, Z. B., Yan, Z. J., Tan, Y. S., Liu, X. Q., & Wang, Y. Y. (2005). Influence of post-annealing treatment on the structure properties of ZnO films. *Applied Surface Science*, 241(3), 303-308. doi:<https://doi.org/10.1016/j.apsusc.2004.07.056>
- Kongtunmon, M., Supadee, L., Kundhikanjana, W., Janphuang, P., Supruangnet, R., Jongpinit, W., Munthala, D., & Pojprapai, S. (2021). Effect of annealing atmosphere on hydration behavior of MgO thin film in tunneling magnetoresistance sensor. *Ceramics International*. doi:<https://doi.org/10.1016/j.ceramint.2021.11.253>

- Lin, Y., Xie, J., Wang, H., Li, Y., Chavez, C., Lee, S., Foltyn, S. R., Crooker, S. A., Burrell, A. K., McCleskey, T. M., & Jia, Q. X. (2005). Green luminescent zinc oxide films prepared by polymer-assisted deposition with rapid thermal process. *Thin Solid Films*, 492(1), 101-104. doi:<https://doi.org/10.1016/j.tsf.2005.06.060>
- Mukhin, N., Chigirev, D., Bakhchova, L., & Tumarkin, A. (2019). Microstructure and Properties of PZT Films with Different PbO Content—Ionic Mechanism of Built-In Fields Formation. *Materials*, 12(18), 2926. Retrieved from <https://www.mdpi.com/1996-1944/12/18/2926>
- Nunes, P., Fortunato, E., & Martins, R. (2001). Influence of the post-treatment on the properties of ZnO thin films. *Thin Solid Films*, 383(1), 277-280. doi:[https://doi.org/10.1016/S0040-6090\(00\)01577-7](https://doi.org/10.1016/S0040-6090(00)01577-7)
- Oswald, S., Lattner, E., & Seifert, M. (2020). XPS chemical state analysis of sputter depth profiling measurements for annealed TiAl-SiO<sub>2</sub> and TiAl-W layer stacks. *Surface and Interface Analysis*, 52(12), 924-928. doi:<https://doi.org/10.1002/sia.6820>
- Shulga, V. I. (2000). The density effects in sputtering of amorphous materials. *Nuclear Instruments and Methods in Physics Research Section B: Beam Interactions with Materials and Atoms*, 170(3), 347-361. doi:[https://doi.org/10.1016/S0168-583X\(00\)00255-X](https://doi.org/10.1016/S0168-583X(00)00255-X)
- Singh, J. P., & Chae, K. H. (2019). Local Electronic Structure Perspectives of Nanoparticle Growth: The Case of MgO. *ACS Omega*, 4(4), 7140-7150. doi:10.1021/acsomega.9b00262
- Singh, J. P., Kim, S. H., Kang, H. K., Won, S. O., Lee, I.-J., & Chae, K. H. (2018). Are organic templates responsible for the optical and magnetic response of MgO nanoparticles? *Materials Chemistry Frontiers*, 2(9), 1707-1715. doi:10.1039/C8QM00145F
- Sun, R., Zhang, H.-Y., Wang, G.-G., Han, J.-C., Wang, X.-Z., Kuang, X.-P., Cui, L., Jin, L., & Tian, J.-L. (2013). Influence of annealing atmosphere on the structure, morphology and transmittance of N-incorporated Ga<sub>2</sub>O<sub>3</sub> films. *Superlattices and Microstructures*, 60, 257-262. doi:<https://doi.org/10.1016/j.spmi.2013.05.004>

- Tolstova, Y., Omelchenko, S. T., Shing, A. M., & Atwater, H. A. (2016). Heteroepitaxial growth of Pt and Au thin films on MgO single crystals by bias-assisted sputtering. *Scientific Reports*, 6(1), 23232. doi:10.1038/srep23232
- Wang, H. J., & Zhu, Y. Y. (2018). Effect of post-annealing on the structure and optical properties of ZnO films deposited on Si substrates. *IOP Conference Series: Materials Science and Engineering*, 382, 022054. doi:10.1088/1757-899x/382/2/022054
- Zahran, H. Y., Shneouda, S. S., Yahia, I. S., & El-Tantawy, F. (2018). Facile and rapid synthesis of nanoplates Mg(OH)<sub>2</sub> and MgO via Microwave technique from metal source: structural, optical and dielectric properties. *Journal of Sol-Gel Science and Technology*, 86(1), 104-111. doi:10.1007/s10971-018-4613-2



## CHAPTER 5

### EFFECT OF ANNEALING ATMOSPHERE ON HYDRATION BEHAVIOR OF MGO THIN FILM IN TUNNELING MAGNETORESISTANCE SENSOR

#### 5.1. Introductions

Chapter 3 and Chapter 4 report the effects of MgO thin films that have been exposed to water and dissolved during the hard disk drive manufacturing process, as well as the effects of heat treatment on moisture and residual stress in the thin films.

This chapter will discuss the effects of storing heat-treated film in a humidity-controlled cabinet at 50% relative humidity for 30 days. MgO thin films are annealed at various atmospheric gasses and then stored for 30 days in a 50% humidity-controlled cabinet to investigate the combined effect of atmospheric annealing and humidity. The atomic force microscope (AFM), X-ray photoelectron spectroscopy (XPS), and focused ion beam scanning electron microscopy (FIB-SEM) were used to determine these effects.

This chapter is divided into the following sections: Section 5.2 describes the experimental procedure used in this study. Section 5.3 discusses data obtained using various analysis techniques, such as section 5.3.1, which includes FIB-SEM cross-sectional image analysis, surface roughness analysis by AFM (section 5.3.2), depth dependent chemical composition analysis by XPS depth profile (section 5.3.3), and the mechanism of MgO thin films hydration (section 5.3.4). Finally, section 5.4 is the conclusion of this chapter.

#### 5.2. Experimental procedure

MgO (50 nm)/ Ru (10 nm)/Si films were provided by Western Digital, LLC, Fremont, CA, US. The heat-treated MgO films at different atmospheres (Ar, N<sub>2</sub>, and normal air) were prepared by annealing the MgO film in a custom-built gas chamber, as shown in Figure 5.1. The gas chamber was placed inside a commercially purchased oven (VULCAN 3-550) during the annealing process. Figure 5.1. (a) shows the sketch



diagram, and Figure 5.1. (b) shows the actual image of a custom-built gas chamber. The samples were annealed at 450 °C for two hours, while flowing Ar, N<sub>2</sub> gasses, and normal air gases into the chamber with a 100 cm<sup>3</sup>/min flow rate. Then, the annealed films are stored in the humidity control cabinet (Weifo, Dry-70, Taiwan), where the internal humidity is regulated at 50% relative humidity for 30 days.

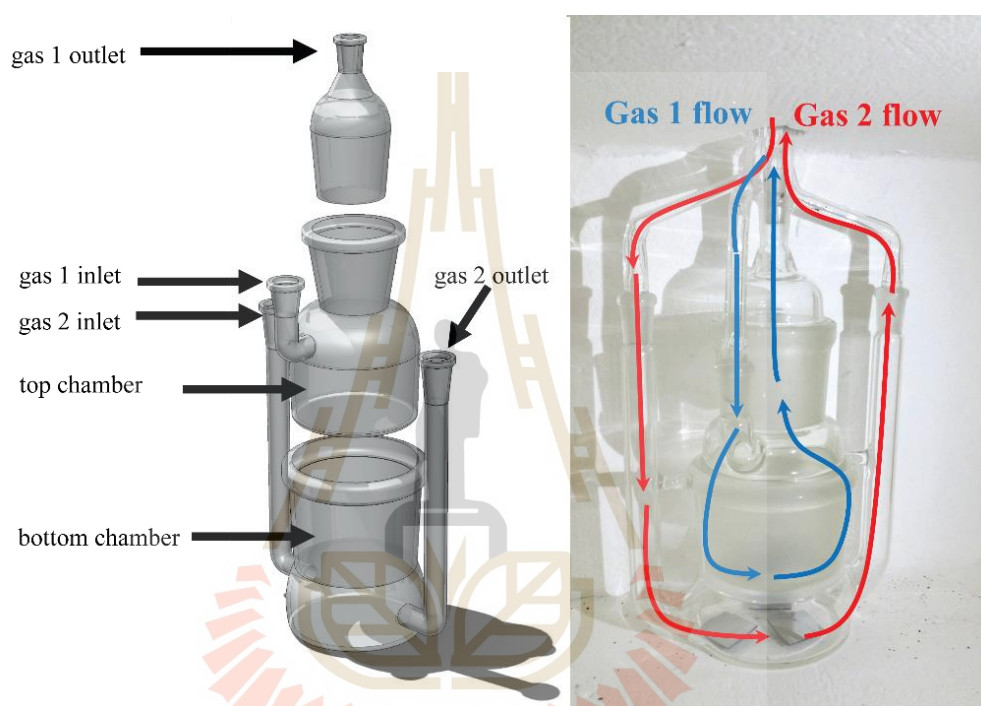


**Figure 5.1** shows the annealing set-up of MgO films. (a) Schematic drawing and (b) actual image of the custom-made gas annealing chamber.

The surface morphology, roughness, topography, and cross-sectional profile of annealed MgO films were studied by using a tapping mode atomic force microscope (AFM, XE-120 Park Systems, scan frequency 0.2 Hz, 512 lines), and focused ion beam scanning electron microscopy (Auriga dual-beam FIB-SEM, Zeiss) respectively. Furthermore, the chemical composition and depth profile of hydration (Mg(OH)<sub>2</sub>) were investigated using X-ray photoelectron spectroscopy (XPS) at Beamline 5.2 of the Synchrotron Light Research Institute (SLRI), Thailand. The high-resolution C 1s, O 1s, and Mg 2p spectra were taken at a 0.1 eV energy step, a 23.5 eV pass energy, and a

total of five cycles. The MgO thin films were etched using an in-situ argon ion ( $\text{Ar}^+$ , 1 keV) source with 1 mA beam current,  $2 \times 2 \text{ mm}^2$  of beam size, and 2 min per step size in order to study the depth profile analysis. The XPS spectra analysis was performed by using commercial CasaXPS (Casa Software Ltd.) software.

### 5.3. Results and discussions

#### 5.3.1. Microstructure analysis by SEM imaging

Figure 5.2. shows SEM micrographs of as-received, Ar gas,  $\text{N}_2$  gas, and normal air annealed MgO films at  $450^\circ\text{C}$ . The thickness of the MgO films was analyzed by a cross-section image of the films using FIB-SEM. As-received MgO film possesses a smooth surface and an average film thickness of 49 nm as shown in Figure 5.2. (a). However, the surface morphology and thickness of MgO films changed drastically at different gas annealed films. After annealing with Ar gas at  $450^\circ\text{C}$ , the thickness of the film slightly increased to 51 nm, as shown in Figure 5.2. (b). Likewise, annealing with  $\text{N}_2$  gas, the film thickness increased to 56 nm (Figure 5.2. (c)). In the case of Figure 5.2. (d), a normal air atmosphere, the film thickness increased almost twice (109 nm) as as-received film. These results are in agreement with the previous work done by L. F. Amaral *et al.* (Amaral *et al.*, 2011) and L. Balcells *et al.* (Balcells *et al.*, 2010). The reason behind the growth of film thickness could be hydroxide formation on the film surface. At high-temperature annealing, the increasing film thickness occurrence causes grain growth, and the size of voids significantly increases (Thompson, 1990). Consequently, the penetrations of residual moisture in the air into the film initiates the hydration reaction within the film. However, this behavior was not seen when the films were annealed in an Argon and Nitrogen gas environment due to the absence of oxygen in the Ar and  $\text{N}_2$  gasses.

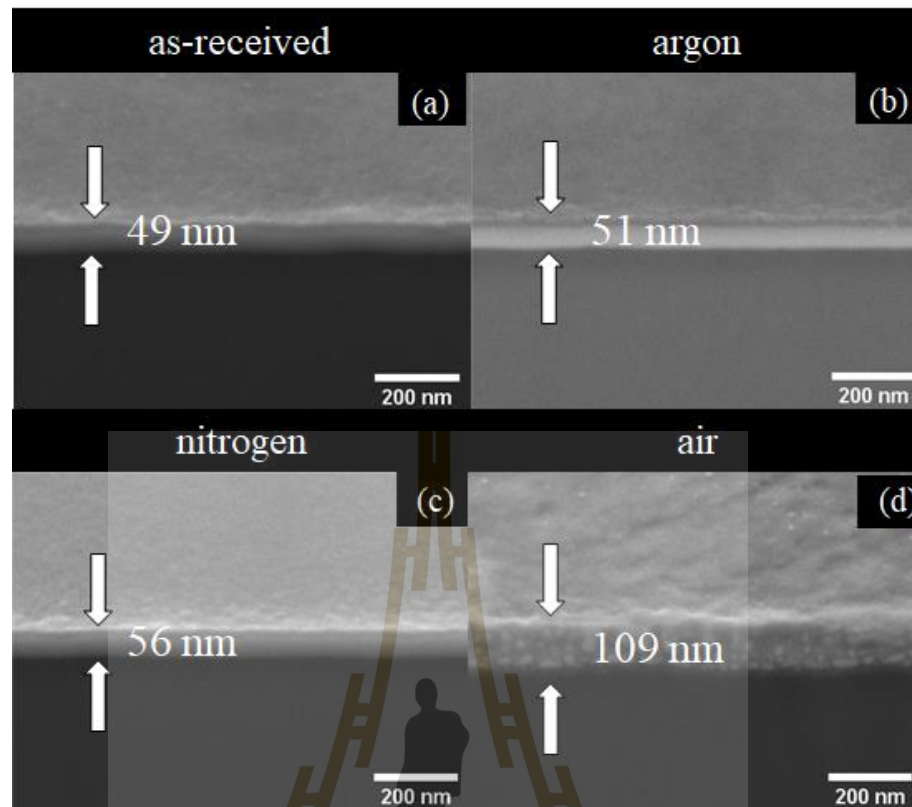


**Figure 5.2** SEM-FIB cross-section of (a) as-received, (b) argon 450 °C, (c) nitrogen 450 °C and (d) air 450 °C annealed samples, respectively.

### 5.3.2. Surface roughness analysis by AFM

AFM micrographs of different gas annealed and moisture-controlled MgO thin films are shown in Figure 5.3. (a-c). The measured root mean square (RMS) roughness values of thin films are 2.5, 3.2, and 5.1 nm, respectively. For Ar, N<sub>2</sub> gasses, and normal air annealed films. It is evident that the MgO thin film annealed under air has higher surface roughness value (5.1 nm) than that of annealed under N<sub>2</sub> (3.2 nm) and Ar (2.5 nm) gasses. The increase in thickness could be due to the grain growth and hydration reaction in MgO films. In particular, annealing under a normal air atmosphere with higher oxygen content could be the cause of a greater degree of grain growth and hydration reactions (Yao et al., 2019). The irregular grain growth causes more surface roughness and voids on the surface of the films.

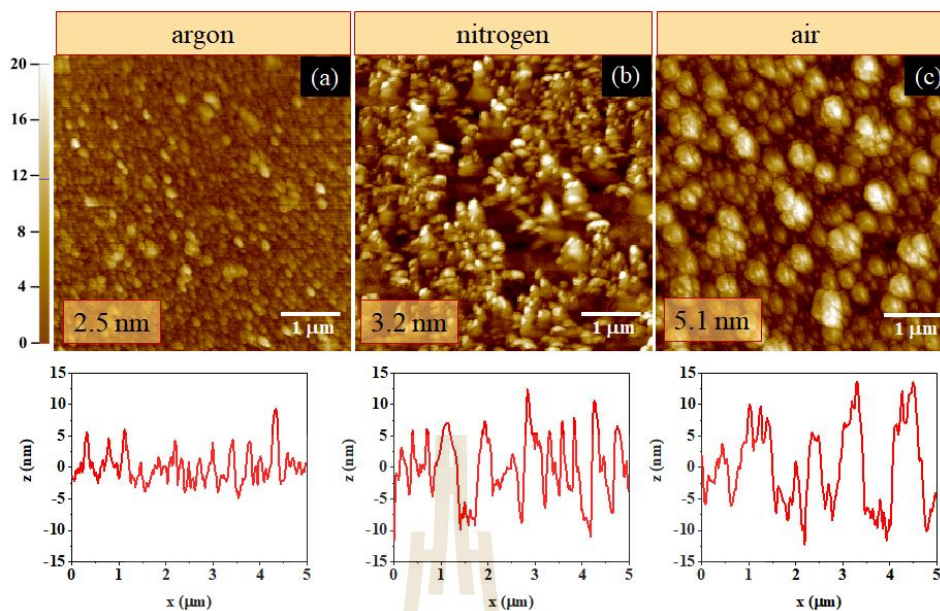


**Figure 5.3** AFM surface images of (a)-(c) the Ar, N<sub>2</sub> and Air 450 °C annealed MgO films after being hydrated (stored in a 50% relative humidity control cabinet for 30 days). The inset numbers are the roughness of the films.

### 5.3.3. Chemical composition analysis by XPS

The chemical composition and depth profile hydration of different gas annealed MgO films were studied using XPS analysis. First, the surface contamination of films was removed by Ar ion etching for 2 min, and the depth profile of hydration was reviewed by etching the films for 10 min. The high-resolution O 1s XPS spectra can provide qualitative and quantitative information about the hydration behavior of MgO films. Figure 5.4. shows the high-resolution O 1s XPS spectra of as-received and annealed MgO films at different atmospheres. The main photoelectron peak between 528-535 eV belongs to the O 1s orbital. Further deconvolution of this peak reveals the accurate chemical composition of elements. The deconvoluted peak at 530.5 eV belongs to the binding energy of MgO (O-Mg), and the deconvoluted peak at 532.1 eV belongs to the hydration behavior of oxygen (O-OH; Mg(OH)<sub>2</sub>) (Liu et al., 1998; M. Santamaria et al., 2007). In this analysis, 2 and 10 minute sputtered O 1s XPS spectra are presented in Figure 5.4. (a)-5.4(d) and 5.4(e)-5.4(h), respectively. The as-received film (sputtered for 2 min as shown in Figure 5.4. (a)) provided the information of the

presence of both hydroxide peak (O-OH;  $\text{Mg}(\text{OH})_2$ ) and the main binding peak MgO (O-Mg). Furthermore, a significant reduction in hydroxide peak ( $\text{Mg}(\text{OH})_2$ ) can be observed in 10 min compared to that of 2 min sputtered films. The depth-dependent (here, each depth is counted for 2 min) hydration reaction (hydroxide peak formation) of all the annealed films are shown in Figure 5.5. In the case of the as-received sample, the hydroxide  $\text{Mg}(\text{OH})_2$  peak percentage decreased with MgO film depth. For 2 min sputtered film, the hydroxide  $\text{Mg}(\text{OH})_2$  peak is significant, when compared to oxide peak (Mg-O), and insignificant (almost disappeared) for 10 min sputtered film. This information provides that the hydration reaction is only limited to the surface layer (for as-received sample). The corresponding images can be seen in Figure 5.4. (a and e). Regarding the Argon annealed films, the rate at which hydroxide  $\text{Mg}(\text{OH})_2$  peak percentage decreases is less than as-received film (as discussed above). The hydroxide  $\text{Mg}(\text{OH})_2$  peak intensity is slightly higher than the as-received sample for 2 min sputtered films and significantly present in 10 min sputtered films as shown in Figure 5.4. (b and f). When it comes to the  $\text{N}_2$  gas annealed films, the rate at which hydroxide  $\text{Mg}(\text{OH})_2$  peak percentage decreases is less than that of both as-received and Argon annealed films, and the presence of hydroxide  $\text{Mg}(\text{OH})_2$  percentage is higher than these films. The hydroxide  $\text{Mg}(\text{OH})_2$  peak intensity is slightly higher than the as-received sample for 2 min sputtered films and significantly present in 10 min sputtered films as shown in Figure 5.4. (c and g). Similarly, the rate at which hydroxide  $\text{Mg}(\text{OH})_2$  peak percentage decreases is significantly less compared to as-received and Ar,  $\text{N}_2$  gas annealed films. However, the presence of hydroxide  $\text{Mg}(\text{OH})_2$  peak on the surface and beneath layers is very much higher than the other film sets (Figure 5.4. (d and h)). This evidence confirms that the hydration reaction rate is higher for normal air annealed films and less than for Ar and  $\text{N}_2$  gas annealed films.

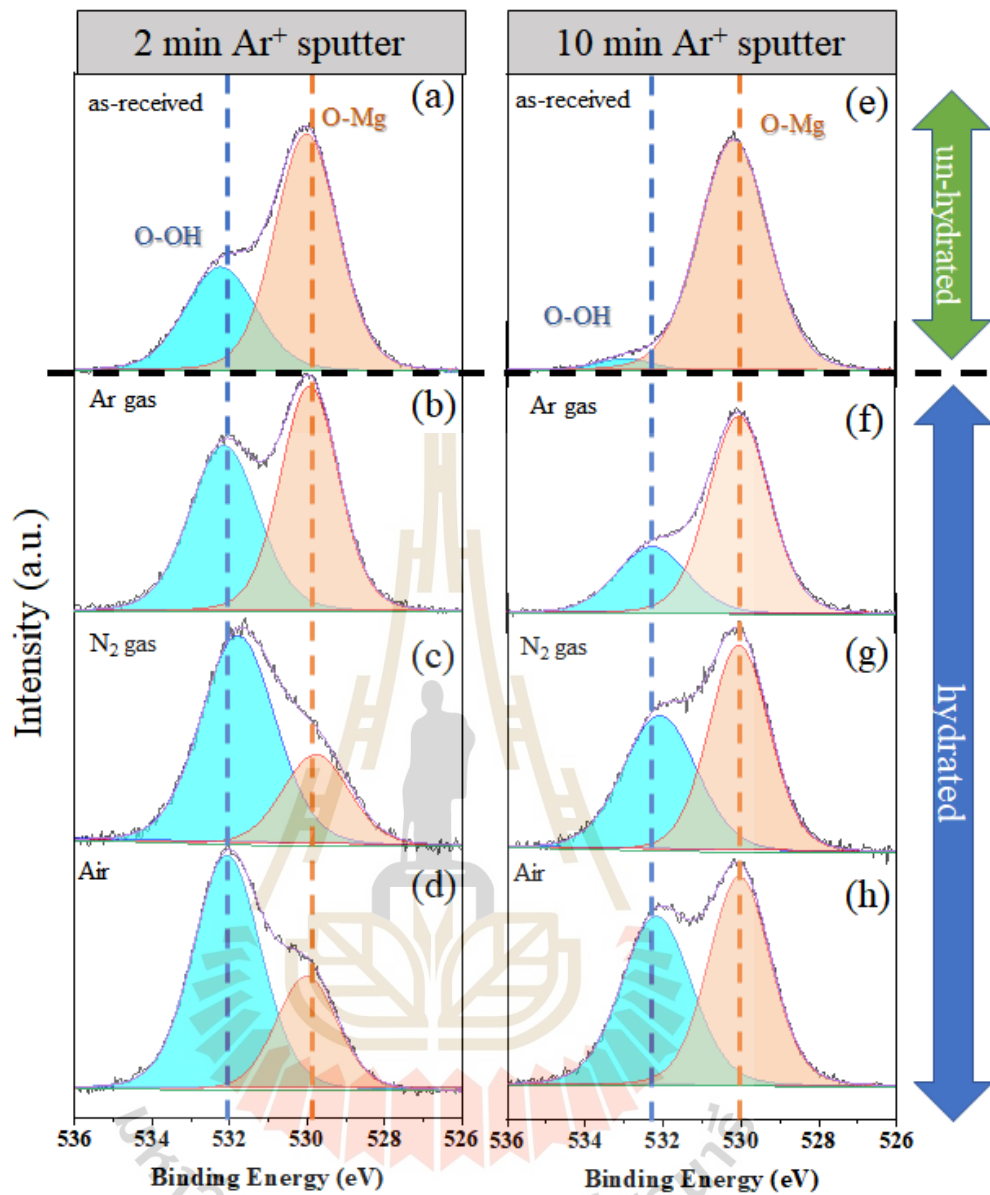


Figure 5.4 comparative O 1s XPS spectra after 2 minutes [(a) – (d)] and 10 minutes [(e) – (h)] of sputter time of un-hydrated (as-received) MgO thin film and hydrated MgO films that were stored in a 50% relative humidity-controlled cabinet for 30 days.

The atomic ratio (O-OH)/(O-Mg) of each sample decreased with sputter time, and this might be due to the removal of the  $\text{Mg}(\text{OH})_2$  layer during  $\text{Ar}^+$  ion etching. From Figure 5.5, it has been shown that the hydroxide/oxide ratio ((O-OH)/(O-Mg)) decreased with the increase in sputter time. The reduction ratio (hydroxide/oxide ratio) is highest for as-received film, followed by Ar annealed,  $\text{N}_2$  annealed, and air annealed samples. Among the annealed films, the Ar annealed film exhibited the highest hydroxide (O-OH) decreasing rate compared to  $\text{N}_2$  annealed films and the lowest for air annealed films. However, the decreasing rates of these  $\text{N}_2$  and air annealed films were much lower than that of the Ar annealed film.

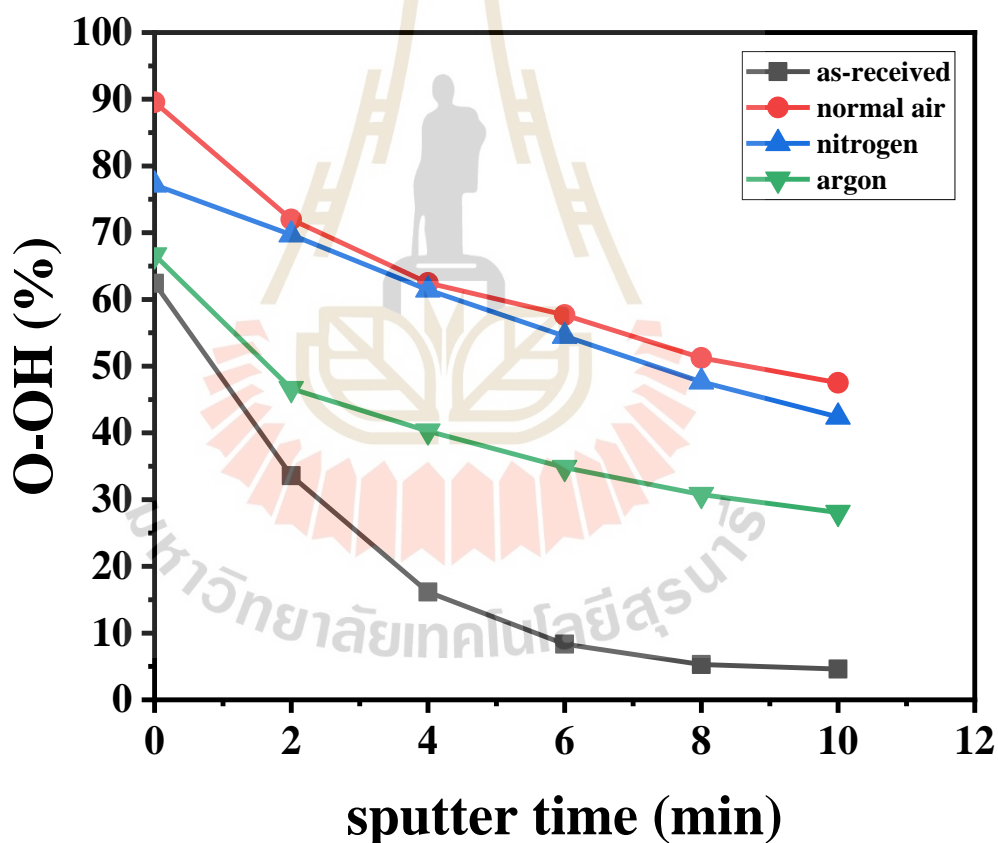


Figure 5.5 XPS sputter time of MgO thin films annealed at different gas environments.

The hydration depth process in thin films layer can be calculated from the sputtering rates of thin films after annealing in Section 3. The result of the calculation

is shown in Figure 5.6. The proportional changes of the hydroxide/oxide peak ratio (O-OH)/(O-Mg) reflected the hydration reaction penetration depth caused by the MgO film's reaction with the residual humidity in the air. Air annealed film thickness is more compared to N<sub>2</sub> and Argon annealed films due to voids created between the grains allowing humidity in the air to penetrate through into the film layer. The figures illustrate that the depth of the hydration process in as-received films and films annealed with argon gas is only a few nanometers. However, when the film is annealed in nitrogen or air atmospheres, the hydration reaction penetrates greater than 6 nm, implying that the reaction penetrates more than 10% of the film thickness. The smaller the film thickness, the smaller the voids in the films. This results, as well, in lower penetration depth of water molecules in the air into the film.

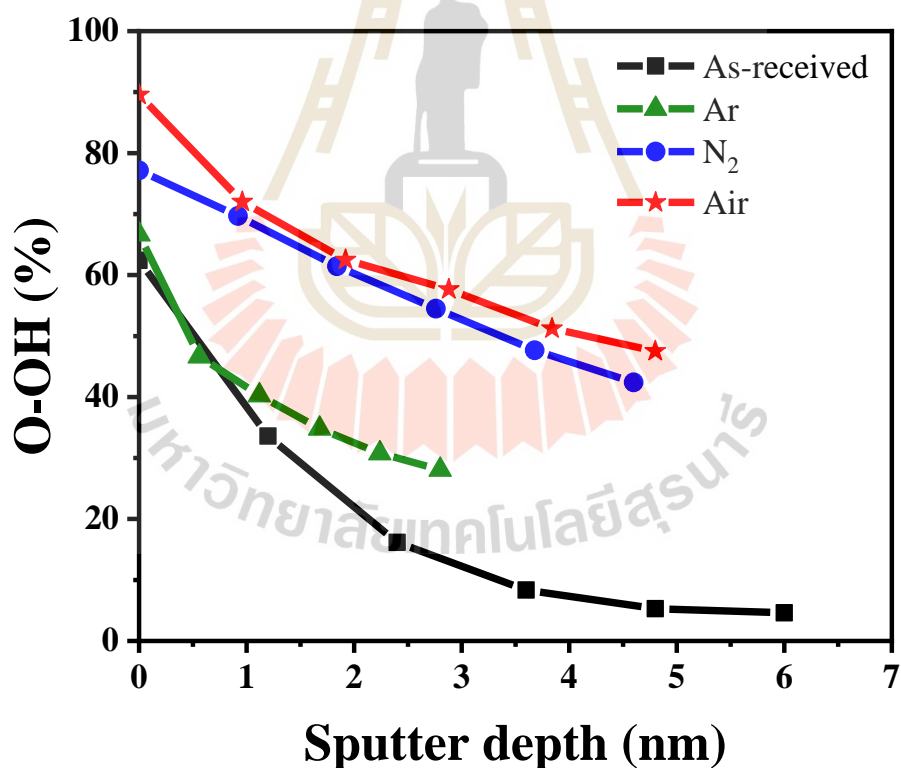


Figure 5.6 hydration reaction depth profile of MgO thin films annealed at different environments.



#### 5.3.4. Mechanism of MgO thin film hydration

To understand the mechanism of hydration reaction deep inside the film, Figure 5.7. shows the effect of MgO grain size on hydration reaction due to humidity in the air. The larger MgO grains create more voids between grain boundaries and allow the water molecules present in the air (in the form of moisture) into the voids. When MgO films are exposed to moisture in the air, the water molecule ( $H_2O$ ) deprotonates to become a hydroxide ion ( $OH^-$ ). Meanwhile, the hydrogen nucleus ( $H^+$ ) formed from the self-ionization of  $H_2O$  to protonate MgO to form  $MgOH^+$  as described in Equation 5.1. After that, the negatively charged  $OH^-$  ions from the humidity attracted by positively charged  $MgOH^+$  ions (on the surface where they are adsorbed) form  $MgOH^+ \cdot OH^-$ , as described in Equation 5.2. The equations associated with the hydration mechanism of MgO thin films are as follows (Birchal et al., 2001; Holt et al., 1997; Kato et al., 1996; Rocha et al., 2004):

- 1) MgO acts as an electron donor in water:



- 2)  $OH^-$  anions are adsorbed on the positively charged surface:



The hydration reaction deeply penetrates the film and causes the swelling of that particular area (Amaral et al., 2011; Carrasco et al., 2010; Holt et al., 1997; Kushner & Hickner, 2017). This effect leads to increased voids, surface swelling, and an increase in the film roughness (Lee et al., 2003). According to Mejias et al. (Mejias et al., 1999), grain size, shape, and porosity further encourage water absorption from air humidity. Along with that, the defect sites in grain boundaries can easily absorb water and form chemisorbed  $Mg(OH)_2$ .

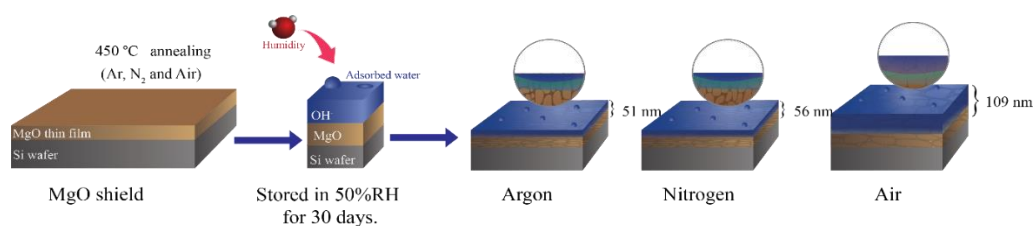


**Figure 5.7** Mechanism of gas annealed MgO thin films hydration.

#### 5.4. Conclusions

In this chapter, the effect of the gas annealing atmosphere on MgO thin films was analyzed. According to AFM observations, most of the surfaces of the MgO thin film remained smooth, except for the air annealed thin film, which had an increase from 49 nm to 109 nm. After heat treatment, grain expansion and voids in nitrogen annealing and air annealing samples were observed. In addition, after the films were hydrated by storing them in a humidity-controlled cabinet at 50% RH for 30 days, the surface became rough and had a mossy appearance. This indicates that a hydration reaction is formed on the film surface by humidity in the air, i.e., the larger the film expansion is, the greater the hydration reaction would be. Larger grains favor hydration via the filling of oxygen vacancies and adsorption of water at the surface. This results in a deterioration in the shielding performance of MgO, consequently resulting in a decrease in the signal output quality of the hard disk reader heads. These findings were confirmed by XPS depth profiling, which indicates that the O-OH bonding of air annealing is the highest when compared to the other annealing atmospheres. The results provide the information for the manufacture of HDD devices to use Ar gas as an annealing atmosphere to reduce the residual stress and humidity in MgO thin films rather than the use of N<sub>2</sub> gas to prevent the film thickness expansion, film surface roughness, and hydroxide penetration depth. In addition, if the film is stored in the humidity control cabinet for a long time, argon gas annealing is recommended.

## 5.5. References

- Amaral, L. F., Oliveira, I. R., Bonadia, P., Salomão, R., & Pandolfelli, V. C. (2011). Chelants to inhibit magnesia (MgO) hydration. *Ceramics International*, 37(5), 1537-1542. doi:10.1016/j.ceramint.2011.01.030
- Balcells, L., Beltrán, J. I., Martínez-Boubeta, C., Konstantinović, Z., Arbiol, J., Martínez, B., D., F. (2010). Aging of magnetic properties in MgO films. *Applied Physics Letters*, 97(25), 252503. doi:10.1063/1.3527963
- Birchal, V. S., Rocha, S. D. F., Mansur, M. B., & Ciminelli, V. S. T. (2001). A simplified mechanistic analysis of the hydration of magnesia. *The Canadian Journal of Chemical Engineering*, 79(4), 507-511. doi:10.1002/cjce.5450790406
- Carrasco, E., Brown, M. A., Sterrer, M., Freund, H.-J., Kwapien, K., Sierka, M., & Sauer, J. (2010). Thickness-Dependent Hydroxylation of MgO(001) Thin Films. *The Journal of Physical Chemistry C*, 114(42), 18207-18214. doi:10.1021/jp105294e
- Holt, S. A., Jones, C. F., Watson, G. S., Crossley, A., Johnston, C., Sofield, C. J., & Myhra, S. (1997). Surface modification of MgO substrates from aqueous exposure: an atomic force microscopy study. *Thin Solid Films*, 292(1), 96-102. doi:10.1016/S0040-6090(96)08955-9
- Kato, Y., Yamashita, N., Kobayashi, K., & Yoshizawa, Y. (1996). Kinetic study of the hydration of magnesium oxide for a chemical heat pump. *Applied Thermal Engineering*, 16(11), 853-862. doi:10.1016/1359-4311(96)00009-9
- Kushner, D. I., & Hickner, M. A. (2017). Water Sorption in Electron-Beam Evaporated SiO<sub>2</sub> on QCM Crystals and Its Influence on Polymer Thin Film Hydration Measurements. *Langmuir*, 33(21), 5261-5268. doi:10.1021/acs.langmuir.7b00759
- Lee, J. H., Eun, J. H., Kim, S. G., Park, S. Y., Lee, M. J., & Kim, H. J. (2003). Hydration behavior of MgO single crystals and thin films. *Journal of Materials Research*, 18(12), 2895-2903. doi:10.1557/JMR.2003.0404
- Liu, P., Kendelewicz, T., Brown, G. E., & Parks, G. A. (1998). Reaction of water with MgO(100) surfaces. Part I: Synchrotron X-ray photoemission studies of low-defect surfaces. *Surface Science*, 412-413, 287-314. doi:10.1016/S0039-6028(98)00444-0

- Marchon, B., Pitchford, T., Hsia, Y.-T., & Gangopadhyay, S. (2013). The Head-Disk Interface Roadmap to an Areal Density of Tbit/in<sup>2</sup>. *Advances in Tribology*, 2013, 8. doi:10.1155/2013/521086
- Mejias, J. A., Berry, A. J., Refson, K., & Fraser, D. G. (1999). The kinetics and mechanism of MgO dissolution. *Chemical Physics Letters*, 314(5–6), 558-563. doi:10.1016/S0009-2614(99)00909-4
- Rocha, S. D. F., Mansur, M. B., & Ciminelli, V. S. T. (2004). Kinetics and mechanistic analysis of caustic magnesia hydration. *Journal of Chemical Technology & Biotechnology*, 79(8), 816-821. doi:10.1002/jctb.1038
- Santamaria, M., Di Quarto, F., Zanna, S., & Marcus, P. (2007). Initial surface film on magnesium metal: A characterization by X-ray photoelectron spectroscopy (XPS) and photocurrent spectroscopy (PCS). *Electrochimica Acta*, 53(3), 1314-1324. doi:10.1016/j.electacta.2007.03.019
- Yao, C., Ismail, M., Hao, A., Thatikonda, S. K., Huang, W., Qin, N., & Bao, D. (2019). Annealing atmosphere effect on the resistive switching and magnetic properties of spinel Co<sub>3</sub>O<sub>4</sub> thin films prepared by a sol-gel technique. *RSC Advances*, 9(22), 12615-12625. doi:10.1039/C9RA01121H

## CHAPTER 6

### CONCLUSION AND FUTURE PERSPECTIVES

This chapter is the conclusion of the dissertation. It also presents the perspectives for the future work.

#### 6.1 General Conclusions

The research goals are to gain a comprehensive understanding of the dissolution and heat treatment mechanisms of the MgO thin film employed as a shielding layer in magnetic sensor MTJs in hard disk drives. The experiment aims to simulate a virtual production environment and determines how it influences the overall properties of the hard disk drive reader head. The models are developed to elucidate the dissolution mechanism of the MgO thin films that could take place during HDD manufacturing processes.

The primary thesis conclusions are summarized as follows.

1. In **Chapter 3**, the dissolution mechanism of the MgO thin film shielding layer is investigated. It is discovered that a hydration reaction occurs rapidly when the MgO thin film layers are exposed to DI water. The hydration reaction that occurs can cause physical and chemical damage to the film and affect the device performance. The amount of dissolved MgO film can be measured by the EC, which is linearly proportional to the amount of  $Mg^{2+}$  in the solution. A model for MgO dissolution, where the precipitated  $Mg(OH)_2$  clusters form a protective layer on the film surface eventually inhibits the dissolution process. The author confirms that the proposed prediction model is in agreement with the experimental results and provide a fundamental understanding of the underlying mechanisms of MgO thin films, which are damaged during the hydration process. The simple experimental setup enables the rapid identification of suitable MgO thin film candidates for the HDD read/write heads and the possibility of optimizing the manufacturing process of such devices.

2. **Chapter4** describes the effect of annealing in different gases annealing at different temperatures of MgO thin films. It is found that the normal air annealed films showed a drastic behavior in film structure and film quality compared to other gas (Ar and N<sub>2</sub>) annealing. The dielectric breakdown voltage decreased as annealing temperature increased, and the rate of reduction was greatest for air annealing, moderate for N<sub>2</sub> gas annealing, and minimal for Ar gas annealing. MgO hydroxide formation played a critical role in the damage of MgO film quality and properties. It is very clear that the MgOH formation is negligible for Ar, N<sub>2</sub> gas annealing and significant for air annealing films. The XPS depth profiling analysis further confirms the MgOH formation decreased with an increased thickness and increased with annealing temperature. The qualitative and quantitative analysis suggests that the Ar gas and moderate annealing temperature are the best results compared to another gas annealing. These results provide critical information to the HDDs manufacturers on the use of Ar gas as an annealing atmosphere to reduce residual stress and humidity in MgO thin films rather than N<sub>2</sub> gas.

3. **Chapter5** provides a detailed study on the effects of MgO film storage in the humidity-controlled cabinet at 50% relative humidity. The moisture in the air initiates a hydration process on the film surface, i.e., film thickness expansion, which increases the hydration reaction and causes the penetration of the hydration process into the film layer. Furthermore, the penetration depth increases with intensifying the film thickness. Larger grains favor the hydration reaction via oxygen vacancy filling and water adsorption at the surface. As a result, degradation in the shielding performance in hard disk reader heads. The XPS depth profiling analysis suggests that air annealing has the largest O-OH bonding corresponding to hydroxide penetration depth compared to other annealing atmospheres. The results indicate that nitrogen gas and air atmosphere heat treatment lead to film expansion, surface roughness, and hydroxide penetration depth. Therefore, HDD devices manufacturing process is advised to employ argon gas as an annealing environment to minimize residual stress and reduce hydroxide formation in MgO thin films, especially when the film is stored in the humidity control cabinet for a long period.

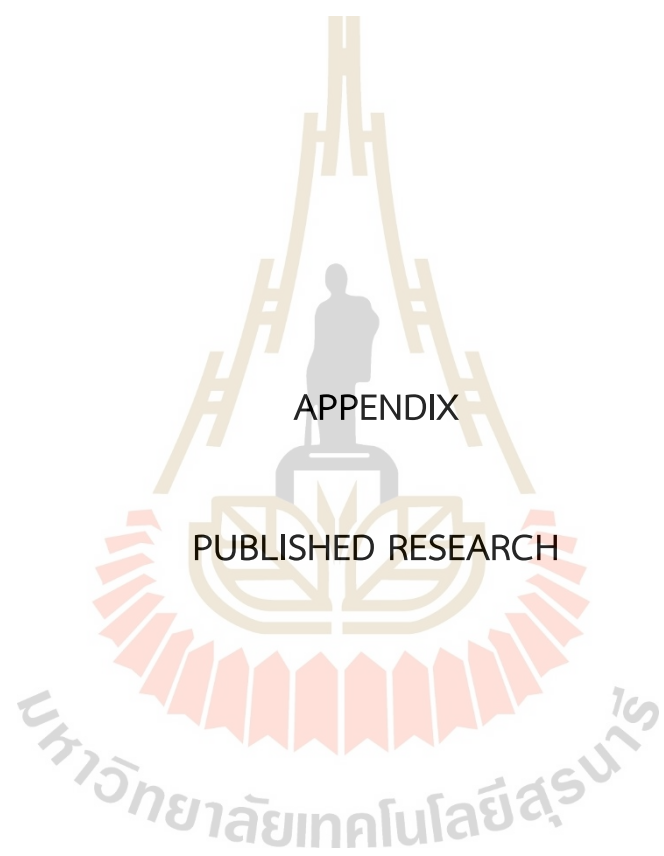
## 6.2 Recommendations for Future Work

6.2.1 This thesis provides a better knowledge of the dissolution mechanism of MgO in DI water. The scope of the future study includes the different types of water-based solutions (such as surfactants for cleaning) for the critical cleaning of the manufacturing process. Lubricants for polishing and coolants in the cutting process can be used to improve the accuracy of the dissolution model.

6.2.2 The influence of the gas environment during the annealing process can affect the physical, chemical, and electrical properties of MgO thin films. Therefore, it is extremely beneficial to investigate the additional properties of the MgO thin film, including mechanical and crystal properties. This discussion will enhance our understanding of thin-film degradation, improving efficiency and reducing waste in the manufacturing process of hard disks that use MgO thin film as MTJs magnetic sensors.

Finally, the author expects that this knowledge will help hard disk drive companies set up optimal methods for manufacturing process conditions to reduce the degradation of magnesium oxide thin films owing to exposure to water, humidity, temperature, and various gas atmospheres during manufacturing.



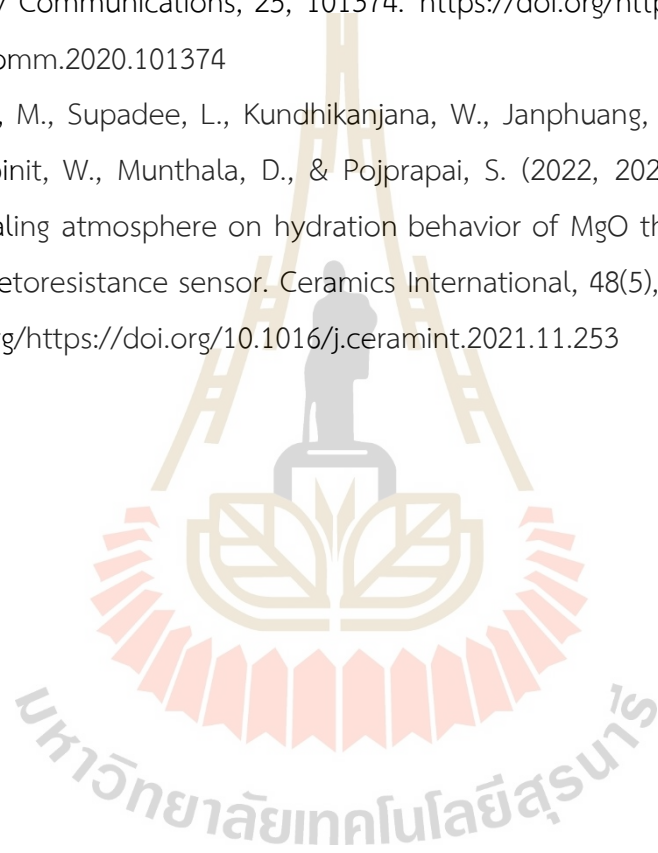




## List Of Publication

Kongtungmon, M., Kundhikanjana, W., Supadee, L., Chanlek, N., & Pojprapai, S. (2020, 2020/12/01/). Dissolution mechanism of MgO thin film shielding layer in tunneling magnetoresistance hard disk drive read head. *Materials Today Communications*, 25, 101374. <https://doi.org/https://doi.org/10.1016/j.mtcomm.2020.101374>

Kongtungmon, M., Supadee, L., Kundhikanjana, W., Janphuang, P., Supruangnet, R., Jongpinit, W., Munthala, D., & Pojprapai, S. (2022, 2022/03/01/). Effect of annealing atmosphere on hydration behavior of MgO thin film in tunneling magnetoresistance sensor. *Ceramics International*, 48(5), 6966-6970. <https://doi.org/https://doi.org/10.1016/j.ceramint.2021.11.253>





## Dissolution mechanism of MgO thin film shielding layer in tunneling magnetoresistance hard disk drive read head

Mongkol Kongtungmon<sup>a</sup>, Worasom Kundhikanjana<sup>b</sup>, Laddawan Supadee<sup>c</sup>, Narong Chanlek<sup>d</sup>, Soodkhet Pojprapai<sup>a,\*</sup>

<sup>a</sup> School of Ceramic Engineering, Institute of Engineering, Suranaree University of Technology, Thailand

<sup>b</sup> School of Physics, Institute of Science, Suranaree University of Technology, Thailand

<sup>c</sup> Modular Cleaning, Western Digital (Thailand) Co., Ltd, Thailand

<sup>d</sup> Synchrotron Light Research Institute, 111 University Avenue, Muang, Nakorn Ratchasima, 30000, Thailand



### ARTICLE INFO

#### Keywords:

MgO  
Dissolution  
Electrical conductivity  
Thin film  
AFM  
Surface roughness

### ABSTRACT

Magnesium oxide (MgO) thin films are used as magnetic shields and barriers for magnetic tunneling junctions in magnetic data storage devices. During the fabrication process, these films are exposed to water, causing a hydration reaction resulting in magnesium hydroxide precipitation. This hydration process can cause material loss and changes in the properties of the films, which may compromise the device performance. In this study, we investigate the dissolution of MgO thin films in deionized water. The magnitude and extent of the damage to the surface structures of the MgO films depend on the properties of the thin films and the time of dissolution. The surface roughness and morphology of the dissolved area are investigated by using atomic force microscopy and scanning electron microscope, respectively. It was found that the surface roughness increased with exposure time to water (from 1 to 10 h), corresponding to increasing film damage. Moreover, a model describing the reaction rate is created based on electrical conductivity measurements of dissolved MgO as a function of time.

### 1. Introduction

Currently, hard disk drives (HDDs) are common storage media that is extensively used because of its high capacity per price ratio. In HDDs, the data is represented as binary bits which are produced by exploiting the magnetoresistive (MR) phenomenon in ferromagnetic materials. MR describes the dependence of the resistance of a ferromagnetic material on the magnetization direction of the applied magnetic field relative to the direction of current flow. When a ferromagnetic material is magnetized parallelly to the direction of current flow, its resistance decreases. On the other hand, when a ferromagnetic material is magnetized perpendicularly to the direction of current flow, its resistance increases. This property of a ferromagnetic material is being utilized for HDDs. In particular, the read/write head is a small active component in a HDD that is used to detect and modify the magnetization of the HDD's ferromagnetic thin films. It is a part of the slider, located at the end of the actuator arm. A schematic drawing of a slider is shown in Fig. 1(a). The magnetization process in HDDs representing the binary data bits by using tunneling magnetoresistance (TMR) is the next step in the development of HDD read heads, the technology which is currently under development.

A magnesium oxide (MgO) thin film is used as a magnetic shielding/insulator layer in TMR sensors because HDD manufacturers have discovered that MgO thin film insulators can increase the signal-to-noise ratio and reduce the side reading effect of HDD read heads [1,2]. The schematic representation of a typical thin-film multilayer stack for the magnetic sensor in a HDD read head is shown in Fig. 1(b). During the HDD manufacturing process, the read/write sensor goes through various production processes such as cutting, cleaning, polishing, and washing.

The major challenge for the MgO in a read/write head is the cleaning/polishing process, where it comes into contact with water. MgO reacts very quickly and easily with water, and even moisture in the air [3–5], which can cause an irreversible hydration reaction and magnesium hydroxide (Mg(OH)<sub>2</sub>) precipitation [6]. The dissolution of an MgO thin film causes material loss and changes in the properties of the film, which can compromise device performance. The hydration process can lead to swelling and cracks in the film due to the density difference between MgO ( $\rho = 3.5 \text{ g/cm}^3$ ) and Mg(OH)<sub>2</sub> ( $\rho = 2.4 \text{ g/cm}^3$ ) [4,6]. An accurate prediction of the dissolution process enables the prevention of device damage and reduces the amount of waste in the production process.

\* Corresponding author.

E-mail address: [soodkhet@g.sut.ac.th](mailto:soodkhet@g.sut.ac.th) (S. Pojprapai).

<https://doi.org/10.1016/j.mtcomm.2020.101374>

Received 28 July 2019; Received in revised form 11 June 2020; Accepted 11 June 2020

Available online 29 June 2020

2352-4928/© 2020 Elsevier Ltd. All rights reserved.

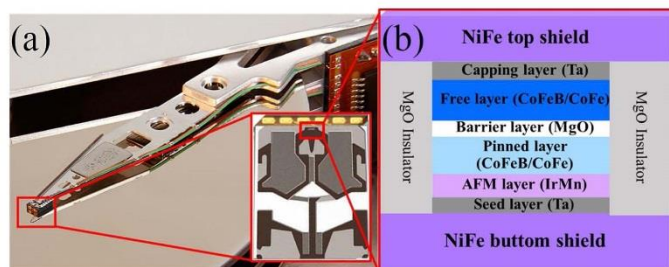


Fig. 1. (a) Schematic illustration of the HDD slider (b) schematic of typical thin-film multilayer stack cross-section for magnetic sensor in hard disk drive read head.

MgO thin film dissolution is typically measured using the amount of the film that has been dissolved in the solution. The precipitation of Mg(OH)<sub>2</sub> is proportional to the amount of water/moisture and the exposure time. The concentration of this product is proportional to the amount of MgO dissolved in water. The mass loss of MgO as a function of time can be expressed as the following reaction rate equation:

$$R(t) = kC_1(t)C_2(t) \quad (1)$$

where  $k$  is the reaction rate, and  $C_1(t)$  and  $C_2(t)$  are the amount of water and MgO, respectively. In the present work, the MgO thin film thickness is only a few tens of nanometers, and thus the amount of MgO is the rate-limiting factor. Taking into account the rate-limiting factor, Eq. 1 then becomes

$$R(t) = kC_2(t) \quad (2)$$

In an actual system, either the reactant runs out or the solution saturates with the Mg(OH)<sub>2</sub> by-products. Thus, the dissolution rate reaction slows down and then eventually stops. A plot of the Mg(OH)<sub>2</sub> concentration as a function of time is therefore characterized by an initial quick increase and gradually followed by a plateau at higher  $t$ .

From the product concentration as a function of time, we can calculate the reaction rate,  $k$ , by calculating the slope of the graph. The reaction rate is often described by an Arrhenius equation:

$$k = Ae^{-E_a/k_B T} \quad (3)$$

where  $E_a$  is the activation energy,  $k_B$  is the Boltzmann's constant, and  $A$  is the number of collisions, which depends highly on the surface area. Plotting  $k$  and  $1/T$  in a logarithmic scale gives the slope, which is proportional to  $E_a$  [7]. The measurement of MgO concentration can be performed over a long time with fine resolution on just one sample.

The MgO dissolution mechanism and the dissolution rate as a function of pH [8], crystal orientations [4,9], temperature [10], and kinetic mechanism [11–14] have been investigated by many recent experiments. However, most of these reports were performed on bulk MgO specimens. Even though these thin films are very important in HDD manufacturing, the dissolution mechanism and dissolution rates in thin films, especially the MgO thin film shielding layer of TMR devices, are not yet well understood. In the present paper, the kinetics of MgO hydration with different exposure time to deionized water (DI water) at room temperature were investigated. The changes of surface roughness and surface morphology were investigated by using atomic force microscopy (AFM) and scanning electron microscopy (SEM). A kinetic model and its verification with electrical conductivity (EC) measurements of samples exposed to DI water for varying amounts of time are proposed. Our model can be used to predict material loss during the production process and identify promising candidates for manufacturing.

## 2. Experimental methods

Specially sputtered 50 nm MgO thin film shielding insulators (i.e. for TMR sensors of HDDs) on silicon substrates (provided by Western Digital, LLC, Fremont, CA, US) were cut into 15 mm × 15 mm coupons for experimental flexibility. These samples were fixed to custom-built test cells (Fig. 2). The surface areas of the MgO films exposed to the solvent were controlled by a 10 mm diameter O-ring fixed to the test cells. Thus, only the encircled film surface was exposed to the 20 mL DI water, allowing for good control of the environment and the properties of the solution.

The EC measurements of the samples as a function of immersion time were carried out at room temperature using an electrode linked to a data acquisition system (Lutron CD-4319SD). The EC data were acquired at a rate of 6 samples per minute and stored in an SD card. A PinAAcle-900 F (PerkinElmer, Germany) atomic absorption spectrometer (AAS) was used to determine the magnesium (Mg) concentration in the dissolved solution. Tapping mode AFM (XE-120 Park Systems, scan frequency 0.2 Hz, 512 lines) was used to scan 5 × 5 μm<sup>2</sup> sample areas. AFM images were analyzed by using XEI software (Park Systems) to extract the roughness and particle size information from the sample surface. Focused ion beam-SEM (FIB-SEM) measurements (Auriga dual beam FIB SEM, Zeiss) were used to investigate the topography and microstructures of the surface (SE detector, 5 kV) as well as the cross-sections (Gallium Ion source, 5 kV). The SEM images processing using ImageJ (NIH Image) and thickness measurements using ellipsometer (M-2000, JA Woollam) were used to extract the Mg(OH)<sub>2</sub> cluster sizes and left-over film profiles, respectively. X-ray photoelectron spectroscopy (XPS) spectra were obtained using a commercial PHI VersaProbe III XPS (ULVAC-PHI, Inc.). The source was monochromatic Al K s radiation (1486.6 eV) and a pass energy of 23.5 eV was used. The analysis



Fig. 2. Schematic view (left) and photograph (right) of the custom-built test cell.

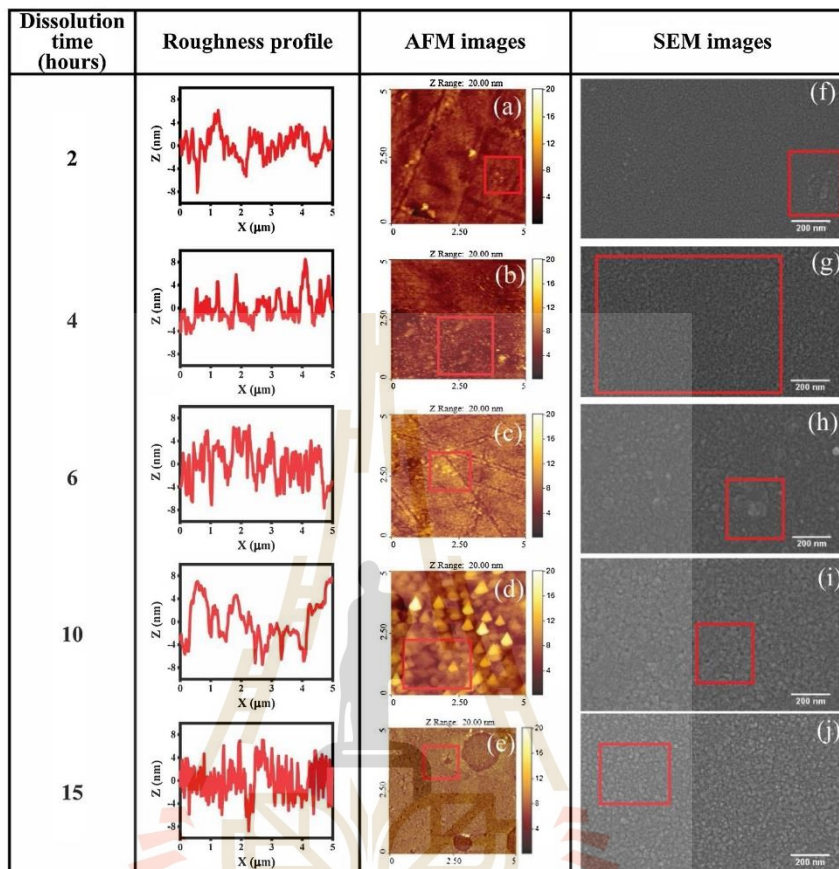


Fig. 3. (a)–(e) AFM images at  $5 \times 5 \mu\text{m}$  scan size and (f)–(j) SEM images at  $\times 50000$  magnification on MgO dissolved surfaces in deionized water for 2, 4, 6, 10, 15 h respectively.

of the XPS spectra was performed using CasaXPS (Casa Software Ltd).

### 3. Results and discussion

When the MgO thin films were in contact with water, reactions such as hydration, dissolution, and precipitation occurred immediately. These reactions affected the physical properties of the thin film surface. Fig. 3 (a) and (f) represent the AFM image of the surface roughness and the topographic SEM image of the MgO film surface after immersion in DI water for 2 h, respectively. These images show that hydration reaction initiated as small groups of 50 nm hydration clusters on the film surface. Immersion of the MgO films for 4 h resulted in the expansion of hydration clusters to a wider area and larger  $\text{Mg}(\text{OH})_2$  clusters with size of approximately 80–100 nm, as shown in Fig. 3(b) and (g). Meanwhile, the film roughness did not change significantly. With an immersion time of 6 h, the  $\text{Mg}(\text{OH})_2$  cluster sizes increased to 200 nm, and parts of the film peeled off about  $0.5\text{--}1 \text{ nm}^2$  as shown in Fig. 3 (c) and

(h). With an immersion time of 10 h, the AFM micrograph shows the maximum roughness in the films (Fig. 3(d)). The SEM image (Fig. 3 (i)) reveals increasing peeling of the surface film, leaving behind deeper areas and small traces of scattered holes that spread throughout the film (Fig. 3(e)). After 15 h of immersion, the film roughness decreased to a minimum value as shown in Fig. 3(j). The surface of the MgO layer was almost insoluble due to  $\text{Mg}(\text{OH})_2$  precipitation possibly because the  $\text{Mg}(\text{OH})_2$  layer acted as a protective layer that blocked further dissolution. Fig. 4 is a plot of the  $\text{Mg}(\text{OH})_2$  cluster size as a function of dissolution time in hours. The cluster size was estimated using the XEI software from the AFM images of the sample surface and was confirmed by particle size measurements from the SEM images using the ImageJ software. The  $\text{Mg}(\text{OH})_2$  cluster size, derived from AFM and SEM images, increased with dissolution time. On the other hand, the film roughness increased initially with dissolution times of up to 10 h, then decreased at 15 h of dissolution time. These observations suggest that  $\text{Mg}^{2+}$  ions formed from the MgO thin film dissolution in the first phase. After 10 h,

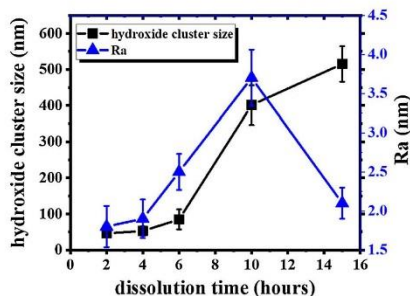


Fig. 4. Film roughness (Ra) and  $\text{Mg}(\text{OH})_2$  cluster size on  $\text{MgO}$  thin films as a function of dissolution time in deionized water derived from AFM images of the surface.

$\text{Mg}(\text{OH})_2$  clusters nearly covered the entire surface area of the dissolved film, which inhibited the further dissolution of the  $\text{MgO}$  film. The roughness of the film surface decreased as the  $\text{Mg}(\text{OH})_2$  coverage became more universal.

The solubility of the  $\text{MgO}$  thin films depended on the dissolution time. The EC meter was used to measure the concentration of  $\text{MgO}$  dissolved in water. Since the EC increased with the amount of  $\text{Mg}^{2+}$  in the DI water, the changes of the EC as a function of time were correlated to the dissolution of  $\text{MgO}$  in DI water. Fig. 5 is the electrical conductivity-dissolution time (ECT) curve which was extracted by using a mathematical model based on the first-order rate law [15] and the multi-rate model by using dynamic fitting [16] of the EC versus dissolution time plot. A nonlinear regression curve (first-order kinetics) representing the behavior of the EC (measured in micro Siemens per centimeter:  $\mu\text{S cm}^{-1}$ ) of  $\text{MgO}$  dissolution as a function of dissolution time,  $t$  (measured in hours) can be expressed by Eq. 4:

$$EC = EC_{\max}(1 - e^{-kt}) \quad (4)$$

where  $EC_{\max}$  is the maximum electrical conductivity, and  $k$  is the reaction constant. The extracted curve fitting parameters are as follows:

$$EC = 8.25(1 - e^{-0.14t}) \quad (5)$$

As measured by atomic absorption spectroscopy (AAS), the concentration of  $\text{Mg}^{2+}$  dissolved in DI water increased as a function of time. The inset in Fig. 5 is a plot of the  $\text{Mg}^{2+}$  concentration in solution versus EC during the dissolution reaction. The calibration curve is

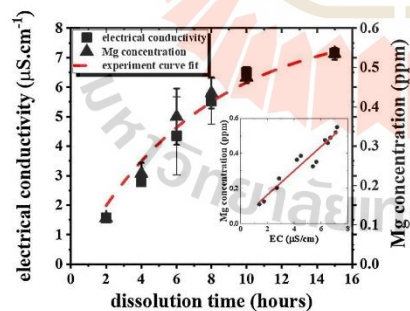


Fig. 5. Electrical conductivity (EC) and Mg concentration as a function of dissolution time. Red dashed line is the curve fit to the experimental data. The inset depicts the linear relationship between Mg concentration and EC.

linear over a wide range of  $\text{Mg}^{2+}$  concentration. The relationship between Mg concentration from AAS,  $[\text{Mg}]$ , and EC is given in Eq. 6:

$$[\text{Mg}] = 0.07EC \quad (6)$$

where EC is measured in  $\mu\text{S/cm}$  while  $[\text{Mg}]$  is measured in  $\text{mg/L}$ . By combining Eq. (5) and (6), the Mg concentration as a function of time can be calculated with the following equation:

$$[\text{Mg}] = 0.58(1 - e^{-0.14t}) \quad (7)$$

The volume of  $\text{MgO}$  thin films that were dissolved in DI water was  $1.571 \times 10^{-5} \text{ cm}^3$  and the mass loss fraction of Mg from the  $\text{MgO}$  density ( $3.51 \text{ g/cm}^3$ ) was  $3.391 \times 10^{-5} \text{ g}$ . If this entire amount was dissolved in water, the maximum  $[\text{Mg}]$  in this experiment was  $1.69 \text{ mg/L}$ . From Eq. 6, the percentage of mass loss can be calculated with the following equation:

$$\% \text{massloss} = 31.95(1 - e^{-0.14t})\% \quad (8)$$

The thickness of films dissolved in DI water as a function of time were estimated by Eq. 8. The comparison between the experimental measurements and calculation model of  $[\text{Mg}]$  versus dissolution time were summarized in Table 1. The calculation model agreed to within 20 % of the experimental measurements. The maximum mass loss in this experiment was approximately 28 %. If the dissolution occurred in a cylindrical volume, the thickness of  $\text{MgO}$  thin films would be reduced to 36 nm from 50 nm as calculated using Eq. 8. However, the remaining  $\text{MgO}$  film thickness, measured using an ellipsometer after 10 h in DI water (Fig. 6), suggests that the dissolution pattern was not cylindrical, but rather semicircular. The film thickness gradually decreased from the O-ring edge to the center of the area exposed to the water. FIB-SEM cross-section images of the Si substrate/ $\text{MgO}$  thin film interface at different locations after 10 h of exposure to DI water corroborate the thickness measurement from the ellipsometer. Fig. 6(b) is the SEM image of the  $\text{MgO}$  surface located outside the O-ring, which corresponds to the area of  $\text{MgO}$  that was not exposed to DI water. The  $\text{MgO}$  film thickness in this location was 60 nm, similar to the thickness of the as-received sample. Fig. 6(c) shows the  $\text{MgO}$  cross-section surface located near the edge of O-ring and inside the dissolution area. The massive agglomerations of particles were expected to be  $\text{Mg}(\text{OH})_2$  clusters [17,18]. The film thickness in this location decreased to 44 nm. Fig. 6(d) shows the  $\text{MgO}$  cross-section surface located at the center of the dissolution area. The surface was rough, with an increasing number of particle clusters. The thickness further decreased to 37 nm.

The films after different amounts of dissolution times were studied using SEM and XPS to confirm the coverage of the precipitated  $\text{Mg}(\text{OH})_2$  clusters over the  $\text{MgO}$  film surfaces. Fig. 7(a) and (b) are SEM micrographs showing  $\text{MgO}$  film morphologies before and after dissolution. Before exposure to the DI water, the films had smooth surfaces of uniformly distributed grains. After DI water exposure, the film morphology changed as a function of the dissolution time. Fig. 7(c) and (d) show the O 1s XPS spectra of the  $\text{MgO}$  films before and after exposure to DI water. The pristine  $\text{MgO}$  films exhibited O 1s binding energy at 530.5 eV. After the  $\text{MgO}$  thin films were immersed in DI water for 10 h, there was a 2 eV redshift in the O 1s binding energy spectra, which indicated that some of the oxygen was present in the form of hydroxide [19]. The deconvolution of the O 1s spectrum (Fig. 7(c)) into two peaks suggests that the peak at 530.1 eV corresponded to the  $\text{MgO}$  component and the peak at 532.1 eV corresponded to the precipitated  $\text{Mg}(\text{OH})_2$  component [20]. For the present work, the XPS data was used to only qualitatively identify the species found at the surface to be mainly  $\text{Mg}(\text{OH})_2$ .

The dissolution mechanism of  $\text{MgO}$  thin films can be explained by the dissolution and precipitation reactions as shown in Fig. 8. When  $\text{MgO}$  is exposed to water, the water molecule,  $\text{H}_2\text{O}$ , deprotonates to become a hydroxide ion ( $\text{OH}^-$ ). Meanwhile, the hydrogen nucleus ( $\text{H}^+$ ) formed from the self-ionization of  $\text{H}_2\text{O}$  immediately protonates  $\text{MgO}$  to form  $\text{MgOH}^+$  as described in Eq. 9. After that, the negatively

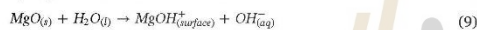
**Table 1**  
Comparison of MgO mass loss from the experimental AAS results and with calculation models (Eqs. 7 and 8) for various time scales.

Sample no.	Dissolution time (hour)	Mg concentration, [Mg]		Mass loss	
		Experiment (mg/L)	Calculation (mg/L)	Experiment (%)	Calculation (%)
1	2	0.12	0.14	8.38	7.80
2	4	0.23	0.25	14.72	13.70
3	6	0.38	0.33	19.50	18.16
4	8	0.38	0.39	23.12	21.53
5	10	0.48	0.44	25.86	24.07
6	15	0.54	0.51	30.12	28.04

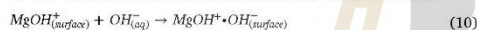
charged  $\text{OH}^-$  ions from the water are attracted to the positively charged  $\text{MgOH}^+$  ions on the surface where they are adsorbed to form  $\text{MgOH}^+ \cdot \text{OH}^-$ , as described in Eq. 10. Eq. 11 describes the dissolution of the MgO films into  $\text{Mg}^{2+}$  and  $\text{OH}^-$  ions dissolved into the water. The amount of  $\text{Mg}^{2+}$  in the solution is associated with material loss from the films as they are continuously dissolved. Eq. 12 describes how the concentration reaches the saturation point:  $\text{Mg}(\text{OH})_2$  precipitates and covers the surface of the thin films as a protective layer, resulting in a lower rate of MgO dissolution. In addition, the precipitation of  $\text{Mg}(\text{OH})_2$  also affects the surface roughness of the films, resulting in thin film surface microstructures that depends on the dissolution time.

The equations associated with the dissolution mechanism of MgO thin films with DI water are as follows [4,12,21,22]:

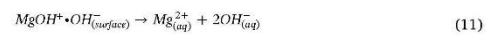
- 1) MgO-alkaline oxide acts as an electron donor in water:



- 2)  $\text{OH}^-$  anions are adsorbed on the positively charged surface:



- 3)  $\text{OH}^-$  anions are desorbed from the surface and release the  $\text{Mg}^{2+}$  ions into the solution:



- 4) Ion concentration in solution reaches supersaturation, the point at which the hydroxide starts to precipitate on the oxide surface:



#### 4. Conclusions

In summary, the dissolution of commercial MgO thin film magnetic insulator layers that are exposed to DI water, which is an existing challenge in the manufacturing process of read/write heads for magnetic HDDs was investigated. When the MgO thin films are exposed to DI water, a hydration reaction occurs rapidly, which can cause physical and chemical damage to the film and affect device performance. This research work demonstrated that the amount of dissolved MgO film can be measured by the EC, which is linearly proportional to the amount of  $\text{Mg}^{2+}$  in the solution. A calculation model for MgO dissolution where the precipitated  $\text{Mg}(\text{OH})_2$  clusters form a protective layer on the film surface that eventually inhibits the dissolution process was proposed. This model agrees very well with the experiment results. The precipitated  $\text{Mg}(\text{OH})_2$  cluster sizes increase with DI water exposure time, while the film roughness initially increased as  $\text{Mg}(\text{OH})_2$  clusters precipitated, but then decreased as the  $\text{Mg}(\text{OH})_2$  coverage became more

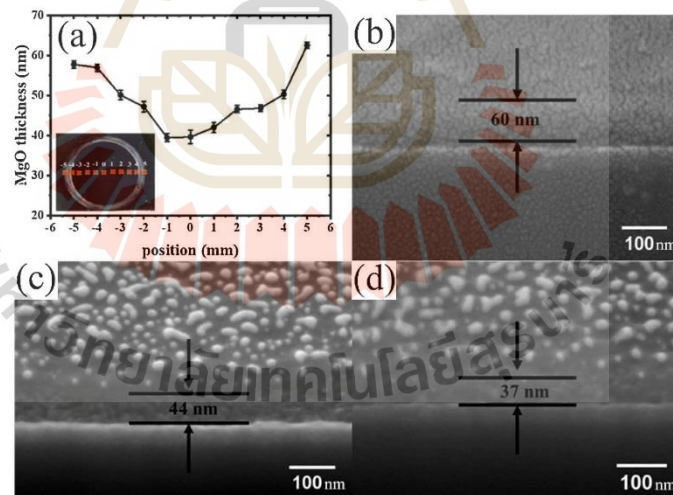


**Fig. 6.** (a) Thickness profile of the MgO thin films after dissolution, as measured by ellipsometry. (b-d) SEM-FIB cross section of the films (b) outside the exposed area, (c) inside the exposed area (near O-ring), and (d) at the center of the exposed area.

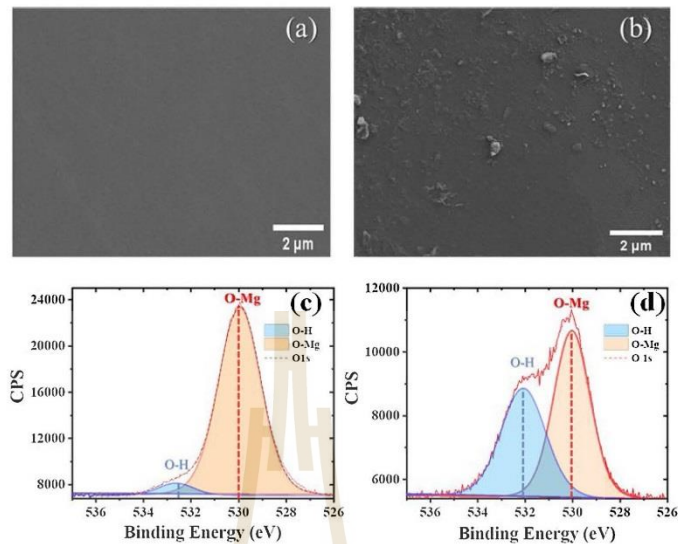


Fig. 7. (a,b)SEM micrographs and (c,d) O 1s XPS spectra of as-received MgO (a and c, respectively), and MgO immersed in deionized water for 10 h (b and d, respectively).

universal. The experimental measurements of MgO mass loss can be estimated by using the calculation model. The model provides a fundamental understanding of the underlying mechanisms of MgO thin film damage during the hydration process. The simple experimental setup of this work enables the rapid identification of suitable MgO thin film candidates for the HDD read/write heads, and the possibility of optimizing the manufacturing process of such devices.

#### CRediT authorship contribution statement

**Mongkol Kongtungmon:** Conceptualization, Methodology, Formal analysis, Investigation, Data curation, Writing - original draft, Visualization. **Worasom Kundhikanjana:** Conceptualization, Methodology, Writing - review & editing, Data curation. **Laddawan Supadee:** Conceptualization, Resources. **Narong Chanlek:** Investigation, Resource. **Soodkhet Pojprapai:** Conceptualization, Methodology, Resources, Data curation, Writing - review & editing.

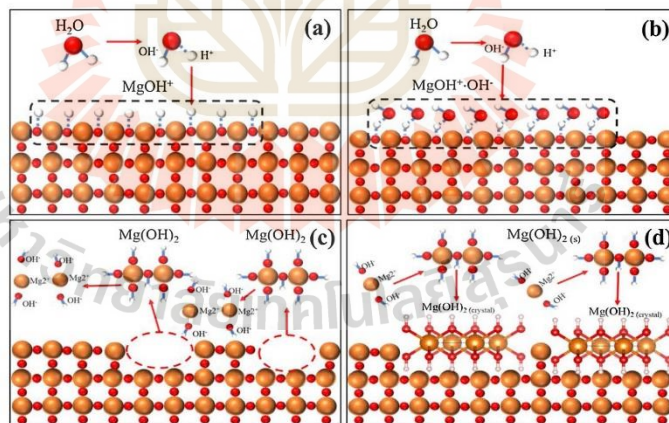


Fig. 8. The mechanism of MgO dissolution (a) surface is protonated by H<sup>+</sup> ions from water (H<sub>2</sub>O), (b) OH<sup>-</sup> negative ions absorbed on the surface to form MgOH<sup>+</sup>·OH<sup>-</sup>, (c) dissolution of the MgO films into Mg<sup>2+</sup> and OH<sup>-</sup> ions, and (d) magnesium hydroxide (Mg(OH)<sub>2</sub>) clusters cover the thin films.

Visualization, Supervision, Project administration, Funding acquisition.

#### Declaration of Competing Interest

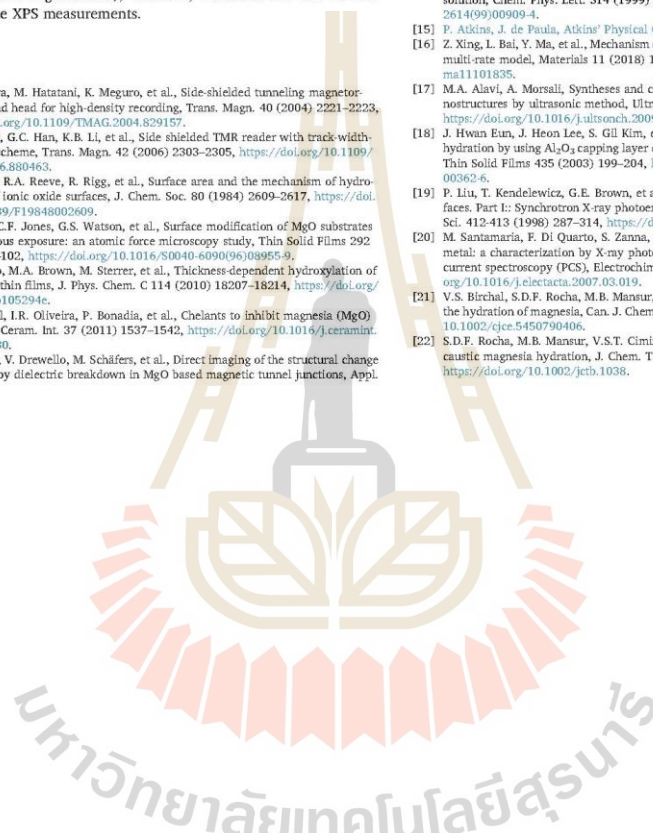
The authors declare that they have no known competing financial interests or personal relationships that could have appeared to influence the work reported in this paper.

#### Acknowledgements

This research is supported by Western Digital Technology (Thailand) research fund. M. Kongtungmon is grateful to Suranaree University of Technology for the One Research One Grant scholarship, and the authors would like to thank the Synchrotron Light Research Institute (Public Organization), Thailand, Beamline 5.3 and 3.2 for supporting the XPS measurements.

#### References

- [1] C. Haginoya, M. Hatatani, K. Meguro, et al., Side-shielded tunneling magnetoresistive read head for high-density recording, *Trans. Magn.* 40 (2004) 2221–2223, <https://doi.org/10.1109/TMAG.2004.829157>.
- [2] Y.K. Zheng, G.C. Han, K.B. Li, et al., Side shielded TMR reader with track-width-reduction scheme, *Trans. Magn.* 42 (2006) 2303–2305, <https://doi.org/10.1109/TMAG.2006.880463>.
- [3] C.F. Jones, R.A. Reeve, R. Rigg, et al., Surface area and the mechanism of hydroxylation of ionic oxide surfaces, *J. Chem. Soc.* 80 (1984) 2609–2617, <https://doi.org/10.1039/F19848002609>.
- [4] S.A. Holt, C.F. Jones, G.S. Watson, et al., Surface modification of MgO substrates from aqueous exposure: an atomic force microscopy study, *Thin Solid Films* 292 (1997) 96–102, [https://doi.org/10.1016/S0040-6090\(96\)08955-9](https://doi.org/10.1016/S0040-6090(96)08955-9).
- [5] E. Carrasco, M.A. Brown, M. Sterrer, et al., Thickness-dependent hydroxylation of MgO(001) thin films, *J. Phys. Chem. C* 114 (2010) 18207–18214, <https://doi.org/10.1021/jp105294e>.
- [6] L.F. Amaral, I.R. Oliveira, P. Bonadia, et al., Chelants to inhibit magnesia (MgO) hydration, *Ceram. Int.* 37 (2011) 1537–1542, <https://doi.org/10.1016/j.ceramint.2011.01.030>.
- [7] A. Thomas, V. Drewello, M. Schäfers, et al., Direct imaging of the structural change generated by dielectric breakdown in MgO based magnetic tunnel junctions, *Appl. Phys. Lett.* 93 (2008) 152508, <https://doi.org/10.1063/1.3001934>.
- [8] O. Frühwirth, G.W. Herzog, I. Hollerer, et al., Dissolution and hydration kinetics of MgO, *Subsurf. Sens. Technol.* 24 (1985) 301–317, [https://doi.org/10.1016/0376-4583\(85\)90080-9](https://doi.org/10.1016/0376-4583(85)90080-9).
- [9] P. Geysmans, F. Finocchi, J. Goniakowski, et al., Combination of (100), (110) and (111) facets in MgO crystals shapes from dry to wet environment, *Phys. Chem. Chem. Phys.* 11 (2009) 2228–2233, <https://doi.org/10.1039/B812376D>.
- [10] L.F. Amaral, I.R. Oliveira, R. Salomão, et al., Temperature and common-ion effect on magnesium oxide (MgO) hydration, *Ceram. Int.* 36 (2010) 1047–1054, <https://doi.org/10.1016/j.ceramint.2009.12.009>.
- [11] J. Blaha, Kinetics of hydration of magnesium oxide in aqueous suspension, *Ceramics-Silikaty* 39 (1995) 45–51.
- [12] Y. Kato, N. Yamashita, K. Kobayashi, et al., Kinetic study of the hydration of magnesium oxide for a chemical heat pump, *Appl. Therm. Eng.* 16 (1996) 853–862, [https://doi.org/10.1016/1359-4311\(96\)00009-9](https://doi.org/10.1016/1359-4311(96)00009-9).
- [13] S. G. L. B. N. N., The kinetics and mechanism of the hydration of magnesium oxide in a batch reactor, *Can. J. Chem. Eng.* 47 (1969) 508–513, <https://doi.org/10.1002/cjce.5450470602>.
- [14] J.A. Mejias, A.J. Berry, K. Refson, et al., The kinetics and mechanism of MgO dissolution, *Chem. Phys. Lett.* 314 (1999) 558–563, [https://doi.org/10.1016/S0009-2614\(99\)00909-4](https://doi.org/10.1016/S0009-2614(99)00909-4).
- [15] P. Atkins, J. de Paula, *Atkins' Physical Chemistry*, OUP Oxford, 2010.
- [16] Z. Xing, L. Bai, Y. Ma, et al., Mechanism of magnesium oxide hydration based on the multi-rate model, *Materials* 11 (2018) 1835, <https://doi.org/10.3390/ma11101835>.
- [17] M.A. Alavi, A. Morsali, Syntheses and characterization of Mg(OH)2 and MgO nanostructures by ultrasonic method, *Ultrason. Sonochem.* 17 (2010) 441–446, <https://doi.org/10.1016/j.ultrsonch.2009.08.013>.
- [18] J. Hwan Eun, J. Heon Lee, S. Gil Kim, et al., The protection of MgO film against hydration by using Al<sub>2</sub>O<sub>3</sub> capping layer deposited by magnetron sputtering method, *Thin Solid Films* 435 (2003) 199–204, [https://doi.org/10.1016/S0040-6090\(03\)00362-6](https://doi.org/10.1016/S0040-6090(03)00362-6).
- [19] P. Liu, T. Kendelewicz, G.E. Brown, et al., Reaction of water with MgO(100) surfaces. Part I: Synchrotron X-ray photoemission studies of low-defect surfaces, *Surf. Sci.* 412–413 (1998) 287–314, [https://doi.org/10.1016/S0039-6028\(98\)00444-0](https://doi.org/10.1016/S0039-6028(98)00444-0).
- [20] M. Santamaria, F. Di Quarto, S. Zanna, et al., Initial surface film on magnesium metal: a characterization by X-ray photoelectron spectroscopy (XPS) and photocurrent spectroscopy (PCS), *Electrochim. Acta* 53 (2007) 1314–1324, <https://doi.org/10.1016/j.electacta.2007.03.019>.
- [21] V.S. Birchal, S.D.F. Rocha, M.B. Mansur, et al., A simplified mechanistic analysis of the hydration of magnesia, *Can. J. Chem. Eng.* 79 (2001) 507–511, <https://doi.org/10.1002/cjce.5450790406>.
- [22] S.D.F. Rocha, M.B. Mansur, V.S.T. Ciminelli, Kinetics and mechanistic analysis of caustic magnesia hydration, *J. Chem. Technol. Biotechnol.* 79 (2004) 816–821, <https://doi.org/10.1002/jctb.1038>.







ELSEVIER

Contents lists available at ScienceDirect

Ceramics International

journal homepage: [www.elsevier.com/locate/ceramint](http://www.elsevier.com/locate/ceramint)

## Effect of annealing atmosphere on hydration behavior of MgO thin film in tunneling magnetoresistance sensor

Mongkol Kongtungmon<sup>a</sup>, Laddawan Supadee<sup>c</sup>, Worasom Kundhikanjana<sup>b</sup>,  
Pattanaiphong Janphuang<sup>d</sup>, Ratchadaporn Supruangnet<sup>d</sup>, Watcharin Jongpinit<sup>a</sup>,  
Dhanunjaya Munthala<sup>a</sup>, Soodkhet Pojprapai<sup>a,\*</sup>

<sup>a</sup> School of Ceramic Engineering Institute of Engineering Suranaree University of Technology, Thailand

<sup>b</sup> School of Physics, Institute of Science, Suranaree University of Technology, Thailand

<sup>c</sup> Mochdar Cleaning, Western Digital (Thailand) Co., Ltd, Thailand

<sup>d</sup> Synchrotron Light Research Institute, 111 University Avenue, Muang, Nakhon Ratchasima, 30000, Thailand

### ARTICLE INFO

#### Keywords:

MgO  
Sputter depth profile  
Annealing  
Thin film  
Hydration  
Hard disk drive  
Surface roughness

### ABSTRACT

The magnesium oxide (MgO) thin films are well known as a magnetic shield in read/write sensor head in a hard disk drive (HDDs). The production room regulates the humidity to approximately 50% RH in the HDD manufacturing process, which is initiating the hydration reaction with MgO films. In this work, MgO thin films were heat-treated at 450 °C under different gases (Ar, N<sub>2</sub>, and air) and stored in controlled humidity to understand and estimate the hydroxide (Mg(OH)<sub>2</sub>) formation. X-ray photoelectron spectroscopy (XPS), atomic force microscope (AFM), and focused ion beam scanning electron microscope (FIB-SEM) were employed to estimate the chemical reactions, surface morphology, and thickness of MgO films. It is found that hydration layer formation increased 28%, 42%, and 47%, respectively, for Ar, N<sub>2</sub>, and air annealed films. Furthermore, the thickness of the MgO films varied differently with different annealing conditions and found that it is proportional to the hydration reaction. The result of this study might be helpful to estimate the better optimization process of read/write sensor head of HDD production.

### 1. Introductions

Nowadays, hard disk drives (HDDs) are still in demand as memory storage devices because they are more versatile and cheaper than solid-state drives. The magnesium oxide (MgO) thin film is used as a magnetic shielding/insulator layer in tunneling magnetoresistance (TMR) sensors to increase the performance of the read/write head in HDDs [1]. Recently, it was found that MgO thin film insulator can increase the signal-to-noise ratio and reduce the side reading effect of HDD read heads [2] (Fig. 1(a)). During the HDD manufacturing, the pre-assembly of the TMR sensor with the HDD slider consists of cutting, cleaning, polishing, and washing process. Unfortunately, MgO reacts very quickly and easily with water or even moisture in the air and leads to an irreversible hydration reaction (magnesium hydroxide (Mg(OH)<sub>2</sub>) precipitation) [3–6]. The sensor head production may require a special cleaning/polishing process where the sensor comes into contact with water. The hydration reaction results in swelling and cracks on the

surface of the film due to the different densities between MgO ( $\rho = 3.5 \text{ g/cm}^3$ ) and Mg(OH)<sub>2</sub> ( $\rho = 2.4 \text{ g/cm}^3$ ) [3–5]. Moreover, mechanical forces also cause residual stress in a thin film. Therefore, hard disk manufacturers prefer to use a preheating method to remove moisture and reduce the residual stress in the film.

Some studies show that thermal annealing improves the dielectric strength, porosity, defects and reduces the leakage current [7–11]. In the case of MgO films, thermal annealing (called calcination) can remove surface adsorbents such as water, hydroxyl (OH), and carbonyl (CO) group [12–14]. Recently, the annealing effect of MgO films used in magnetic tunnel junction (MTJs) is an interesting subject. It has been shown that the annealing process improves the crystallinity and structure at the interface of the MgO and CoFeB, resulting in an increase in magnetoresistance [15–17].

Annealing temperature, annealing condition, and amount of humidity maintained in the processing room greatly affect the film qualities (chemical and structural stability, density, porosity, and roughness).

\* Corresponding author.

E-mail address: [soodkhet@g.sut.ac.th](mailto:soodkhet@g.sut.ac.th) (S. Pojprapai).

<https://doi.org/10.1016/j.ceramint.2021.11.253>

Received 24 September 2021; Received in revised form 10 November 2021; Accepted 24 November 2021

Available online 25 November 2021

0272-8842/© 2021 Elsevier Ltd and Techna Group S.r.l. All rights reserved.

## ARTICLE IN PRESS

M. Kongtuanon et al.

Ceramics International xxx (xxxx) xxx

In the HDD manufacturing process, production room regulates the humidity approximately 50% RH, which could initiate the hydration reaction with MgO thin films. The change in physical and chemical properties of MgO thin film can alter the magnetic sensitivity of the read/write sensor head [18], and the film surface roughness related to the distance between the read/write head and magnetic plate [19] (Fig. 1(b)). In this work, MgO thin films are annealed at different atmospheres and stored in a 50% humidity control chamber for 30 days to study the combined effect of both atmospheric annealing and humidity control reaction effects. The above results will be discussed in the framework of atomic force microscope (AFM), X-ray photoelectron spectroscopy (XPS), and Focused ion beam scanning electron microscopy (FIB-SEM).

## 2. Material and methods

MgO (50 nm)/Ru (10 nm)/Si films were provided by Western Digital, LLC, Fremont, CA, US. The heat-treated MgO films at different atmospheres (Ar, N<sub>2</sub> and normal air) were prepared by annealing the MgO film in a custom-built gas chamber, as shown in Fig. 2. The gas chamber was placed inside a commercially purchased oven (VULCAN 3-550) during the annealing process. Fig. 2(a) shows the sketch diagram, and Fig. 2(b) shows the actual image of a custom-built gas chamber. The samples were annealed at 450 °C for 2 h while flowing Ar, N<sub>2</sub> gases, and normal air gases into the chamber with a 100 cm<sup>3</sup>/min flow rate.

The surface morphology, roughness, topography, and cross-sectional profile of annealed MgO films were studied by using tapping mode atomic force microscope (AFM, XE-120 Park Systems, scan frequency 0.2 Hz, 512 lines), and focused ion beam scanning electron microscopy (Auriga dual-beam FIB-SEM, Zeiss) respectively. In addition, the chemical composition and depth profile of hydration (Mg(OH)<sub>2</sub>) were studied using X-ray photoelectron spectroscopy (XPS) at Beamline 5.2, Synchrotron Light Research Institute (SLRI), Thailand. The high-resolution C 1s, O 1s, and Mg 2p spectra were taken at 0.1 eV energy step, 23.5 eV pass energy, and a total of five cycles. The MgO thin films were etched using an in-situ argon ion (Ar<sup>+</sup>, 1 keV) source with 1 mA beam current, 2 × 2 mm<sup>2</sup> of beam size, and 2 min per step size order to study the depth profile analysis. The XPS spectra analysis was performed by using a commercial CasaXPS (Casa Software Ltd.) software.

## 3. Results and discussion

### 3.1. Microstructure analysis by SEM imaging

Fig. 3 shows SEM micrographs of as-received, Ar gas, N<sub>2</sub> gas, and normal air annealed MgO films at 450 °C. The thickness of the MgO films was analyzed by cross-section image of the films using FIB-SEM. As-

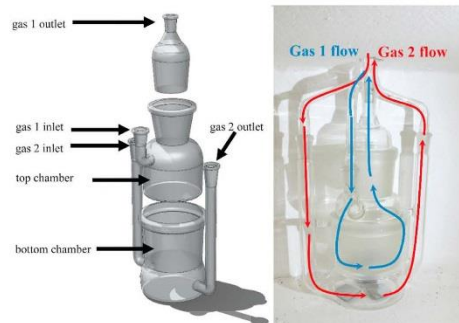


Fig. 2. shows the annealing set-up of MgO films. (a) Schematic drawing and (b) actual image of the custom-made gas annealing chamber.

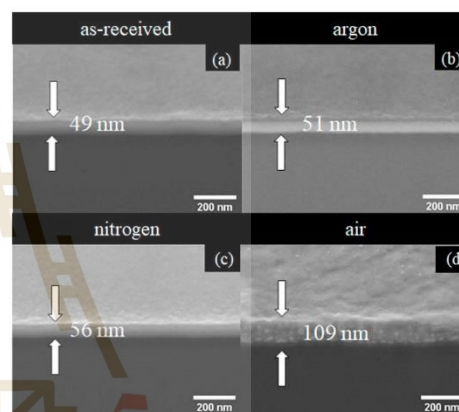


Fig. 3. SEM-FIB cross-section of (a) as-received, (b) argon 450 °C, (c) nitrogen 450 °C and (d) air 450 °C samples, respectively.

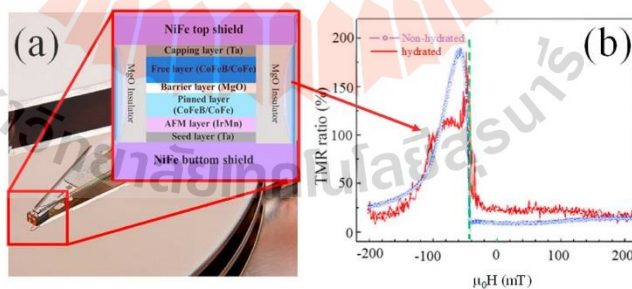


Fig. 1. (a): schematic of a typical thin-film multilayer stack cross-section for magnetic sensors in a hard disk drive reader head (b) TMR signal comparison between non-hydrated and hydrated insulator films.

received MgO film possesses a smooth surface and an average film thickness of 49 nm as shown in Fig. 3(a). However, the surface morphology and thickness of MgO films changed drastically at different gas annealed films. After annealing with Ar gas at 450 °C, the thickness of the film slightly increased to 51 nm, as shown in Fig. 3(b). Likewise, annealing with N<sub>2</sub> gas, the film thickness increased to 56 nm (Fig. 3(c)). Finally, in the case of Fig. 3(d) a normal air atmosphere, the film thickness was increased almost twice (109 nm) thick as as-received film. These results are in agreement with the previous work done by L. F. Amaral et al. [5] and L. Balcells et al. [18]. The reason behind the growth of film thickness could be hydroxide formation on the film surface.

### 3.2. Surface roughness analysis by AFM

AFM micrographs of different gas annealed and moisture control stored MgO thin films are shown in Fig. 4(a–c). The measured root mean square (RMS) roughness values of thin films are 2.5, 3.2, and 5.1 nm, respectively for Ar, N<sub>2</sub> gases, and normal air annealed films. It is evident that the MgO thin film annealed under air has the highest surface roughness value (5.1 nm) than that of annealed under N<sub>2</sub> (3.2 nm) and Ar (2.5 nm) gases. The increase in thickness could be due to the grain growth and hydration reaction in MgO film. In particular, annealing under a normal air atmosphere with higher oxygen content could be the cause of a greater degree of grain growth and hydration reactions [20]. The irregular grain growth causes more surface roughness and voids on the surface of the films.

### 3.3. Chemical composition analysis by XPS

The chemical composition and depth profile hydration of different gas annealed MgO films were studied using XPS analysis. First, the surface contamination of films was removed by Ar ion etching for 2 min and the depth profile of hydration was reviewed by etching the films for 10 min. The high-resolution O 1s XPS spectra can provide qualitative

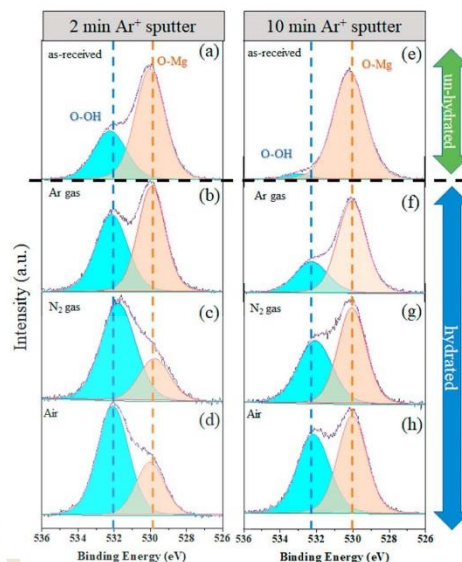


Fig. 5. Comparative O 1s XPS spectra after 2 min [(a)–(d)] and 10 min [(e)–(h)] of sputter time of un-hydrated (as-received) MgO thin film and hydrated MgO films that were stored in a 50% relative humidity-controlled cabinet for 30 days.

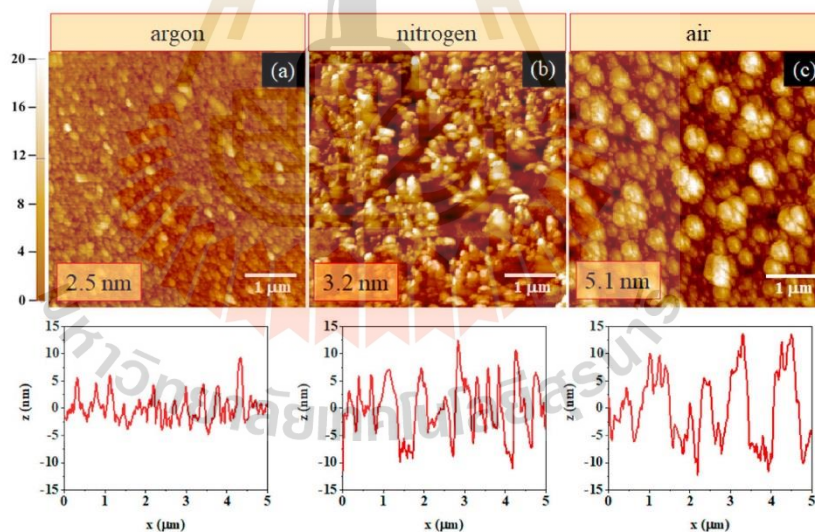


Fig. 4. AFM surface images of (a)–(c) the Ar, N<sub>2</sub> and Air 450 °C annealed MgO films after being hydrated (stored in a 50% relative humidity control cabinet for 30 days). The inset numbers are the roughness of the films.

and quantitative information of the hydration behavior of MgO films. Fig. 5 shows the high-resolution O 1s XPS spectra of as-received and annealed MgO films at different atmospheres. The main photoelectron peak between 528 and 535 eV belongs to the O 1s orbital. Further deconvolution of this peak reveals the accurate chemical composition of elements. The deconvoluted peak at 530.5 eV belongs to the binding energy of MgO (O–Mg), and the deconvoluted peak at 532.1 eV belongs to the hydration behavior of oxygen (O–OH; Mg(OH)<sub>2</sub>) [21,22].

In this analysis, 2 and 10 min sputtered O 1s XPS spectra are presented in Fig. 5 (a)–5(d) and 5(e)–5(h), respectively. The as-received film (sputtered for 2 min as shown in Fig. 5(a)) provided the information that the presence of both hydroxide peak (O–OH; Mg(OH)<sub>2</sub>) and the main binding peak MgO (O–Mg). Furthermore, a significant reduction in hydroxide peak (Mg(OH)<sub>2</sub>) can observe in 10 min sputtered films compared to that of 2 min sputtered films. The depth-dependent (here, each depth is counted for 2 min) hydration reaction (hydroxide peak formation) of all the annealed films are shown in Fig. 6.

In the case of the as-received sample, the hydroxide Mg(OH)<sub>2</sub> peak percentage decreased with MgO film depth. The hydroxide Mg(OH)<sub>2</sub> peak is significant compared to oxide peak (Mg–O) for 2 min sputtered film and insignificant (almost disappeared) for 10 min sputtered film. This information provides that the hydration reaction is only limited to the surface layer (for as-received sample). The corresponding images can be seen in Fig. 5(a and e). Regarding the Ar gas annealed films, the rate at which hydroxide Mg(OH)<sub>2</sub> peak percentage decrease is less than as-received film (as discussed above). The hydroxide Mg(OH)<sub>2</sub> peak intensity is slightly higher than the as-received sample for 2 min sputtered films and significantly present in 10 min sputtered film as shown in Fig. 5(b and f). When it comes to the N<sub>2</sub> gas annealed films, the rate at which hydroxide Mg(OH)<sub>2</sub> peak percentage decrease is less than that of both as-received and Ar gas annealed films, and the presence of hydroxide Mg(OH)<sub>2</sub> percentage is higher than these films. The hydroxide Mg(OH)<sub>2</sub> peak intensity is slightly higher than the as-received sample for 2 min sputtered films and significantly present in 10 min sputtered film as shown in Fig. 5 (c and g). Similarly, the rate at which hydroxide Mg(OH)<sub>2</sub> peak percentage decrease is significantly less compared to as-received and Ar, N<sub>2</sub> gas annealed films. However, the presence of hydroxide Mg(OH)<sub>2</sub> peak on the surface and beneath layers is very much higher than the other film sets (Fig. 5 (d and h)). This evidence confirms that the hydration reaction rate is higher for normal air annealed films and less in Ar and N<sub>2</sub> gas annealed films.

The atomic ratio (O–OH)/(O–Mg) of each sample decreased with

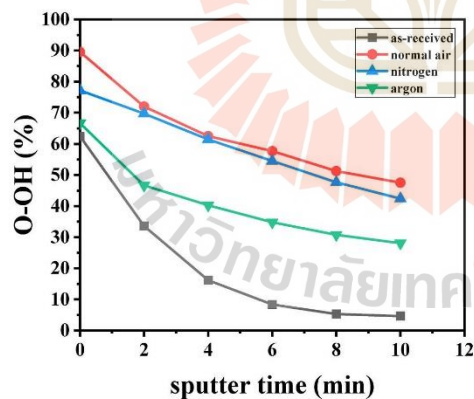
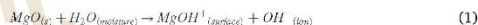


Fig. 6. Depth profile hydration reaction in MgO thin films annealed at different environments.

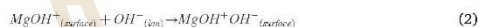
sputtering time, and this might be due to the removal of the Mg(OH)<sub>2</sub> layer during Ar<sup>+</sup> ion etching. From Fig. 6, it has been shown that the hydroxide/oxide ratio ((O–OH)/(O–Mg)) decreased with the increase of sputter time. The reduction ratio (hydroxide/oxide ratio) is highest for as-received film, followed by Ar annealed, N<sub>2</sub> annealed, and air annealed sample. Among the annealed films, the Ar annealed film exhibited the highest hydroxide (O–OH) decreasing rate compared to N<sub>2</sub> annealed films and lowest for air annealed films. However, the decreasing rates of these N<sub>2</sub> and air annealed films were much lower than that of the Ar annealed film. The decrease of hydroxide/oxide (O–OH)/(O–Mg) peak ratio with penetration depth reflects the decrease hydration reaction with the residual humidity in the air. Air annealed films thickness is more compared to N<sub>2</sub> and Ar gas annealed films. This created voids between the grains allowing humidity in the air to penetrate through the voids deep into the film layer. The smaller the film thickness, the smaller the voids in the films. This results, as well, in lower penetration depth of water molecules in the air into the film.

To understand the mechanism of hydration reaction deep inside the film, Fig. 7 shows the effect of MgO grain size on hydration reaction due to humidity in the air. The larger MgO grains create more voids between grain boundaries and allow the water molecules present in the air (in the form of moisture) into the voids. When MgO films are exposed to moisture in the air, the water molecule (H<sub>2</sub>O) deprotonates to become a hydroxide ion (OH<sup>-</sup>). Meanwhile, the hydrogen nucleus (H<sup>+</sup>) formed from the self-ionization of H<sub>2</sub>O to protonate MgO to form MgOH<sup>+</sup> as described in below Equation (1). After that, the negatively charged OH<sup>-</sup> ions from the humidity attracted by positively charged MgOH<sup>+</sup> ions (on the surface where they are adsorbed) form MgOH<sup>+</sup>•OH<sup>-</sup>, as described in Equation (2). The equations associated with the hydration mechanism of MgO thin films are as follows [3,23–25]:

1) MgO acts as an electron donor in water:



2) OH<sup>-</sup> anions are adsorbed on the positively charged surface:



The hydration reaction deeply penetrates the film and causes swelling of that particular area [3–5,26]. This effect leads to increased voids, surface swelling, and an increase of film in the roughness [27]. In addition, according to Mejias et al. [28], grain size, shape, and porosity further encourage water absorption from air humidity. Along with that, the defect sites in grain boundaries can easily absorb water and form chemisorbed Mg(OH)<sub>2</sub>.

#### 4. Conclusions

In conclusion, the effect of gas annealing atmosphere on MgO thin films was analyzed by SEM, AFM, and XPS with Ar<sup>+</sup> ion cluster sputtering. According to AFM observations, most of the surfaces of the MgO thin film remain smooth, except for air annealed thin film, which had an increase from 49 nm to 109 nm. After heat treatment, grain expansion and voids in nitrogen annealing and air annealing samples were observed. In addition, after the films were hydrated by storing films in a humidity-controlled cabinet at 50% RH for 30 days, the surface became rough and had a mossy appearance. This indicates that hydration reaction is formed on the film surface from humidity in the air, i.e., the larger film expansion is the greater the hydration reaction would be. Larger grains favor hydration via the filling of the oxygen vacancies and adsorption of water at the surface. This results in a deterioration in the shielding performance of MgO, consequently resulting in a decrease in the signal output quality of the hard disk reader heads. These findings were confirmed by XPS depth profiling, which indicates that O–OH bonding of air annealing is highest compared to the other annealing

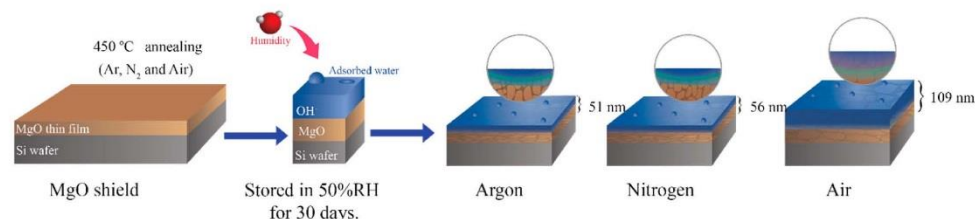


Fig. 7. Mechanism of gas annealed MgO thin films hydration.

atmospheres. The results provide the information for the manufacture of HDD devices to use Ar gas as an annealing atmosphere to reduce the residual stress and humidity in MgO thin film rather than the use of N<sub>2</sub> gas to prevent the film thickness expansion, film surface roughness, and hydroxide penetration depth. In addition, if the film is to be stored in the humidity control cabinet for a long time, argon gas annealing is recommended.

#### Declaration of competing interest

The authors declare that they have no known competing financial interests or personal relationships that could have appeared to influence the work reported in this paper.

#### Acknowledgment

This work was supported by (i) Suranaree University of Technology (SUT), (ii) Thailand Science Research and Innovation (TSRI), and (iii) National Science, Research and Innovation Fund (NSRF) (Project code 90464). It was also supported by Western Digital (Thailand). The authors would like to thank the Synchrotron Light Research Institute (Public Organization), Thailand, Beamline 5.3 and 3.2 for supporting the XPS measurements.

#### References

- [1] C. Hagino, M. Hatatani, K. Meguro, C. Ishikawa, N. Yoshida, K. Kusikawa, K. Watanabe, Side shielded tunneling magnetoresistive read head for high density recording, *IEEE Trans. Magn.* 40 (2004) 2221–2223.
- [2] Y.K. Zheng, G. Han, K.B. Li, Z.B. Guo, J. Qiu, S.G. Tan, Z.Y. Liu, B. Liu, Y.H. Wu, Side shielded TMR reader with track width reduction scheme, *Magnetics, IEEE Trans. on* 42 (2006) 2303–2305.
- [3] S.A. Holt, C.F. Jones, G.S. Watson, A. Crossley, C. Johnston, C.J. Sofield, S. Myhra, Surface modification of MgO substrates from aqueous exposure: an atomic force microscopy study, *Thin Solid Films* 292 (1997) 96–102.
- [4] E. Carrasco, M.A. Brown, M. Steiner, H.J. Freund, K. Kwapien, M. Sterka, J. Sauer, Thickness-dependent hydroxylation of MgO(001) thin films, *J. Phys. Chem. C* 114 (2010) 18207–18214.
- [5] L.F. Amaral, I.R. Oliveira, P. Bonadia, R. Salomão, V.C. Pandolfelli, Chelants to inhibit magnesia (MgO) hydration, *Ceram. Int.* 37 (2011) 1537–1542.
- [6] C.F. Jones, R.A. Reeve, R. Rigg, R.L. Segall, R.S.C. Smart, P.S. Turner, Surface area and the mechanism of hydroxylation of ionic oxide surfaces, *J. Chem. Soc., Faraday Trans. 1: Phys. Chem. Condens. Phases* 80 (1984) 2609–2617.
- [7] Y.-L. Cheng, K.-C. Kao, G.-S. Chen, J.-S. Fang, C.-R. Sun, W.-H. Lee, Effect of annealing temperature on electrical and reliability characteristics of HfO<sub>2</sub>/porous low-k dielectric stacks, *Microelectron. Eng.* 162 (2016) 34–39.
- [8] H. Keiji, N. Makoto, U. Tomomasa, A. Hisanori, I. Sumio, A. Yoshiaki, Y. Hiroaki, N. Akhiro, Effect of self-heating on time-dependent dielectric breakdown in ultrathin MgO magnetic tunnel junctions for spin torque transfer switching magnetic random access memory, *Jpn. J. Appl. Phys.* 49 (2010), 04DD15.
- [9] M.-H. Jo, H.-H. Park, Leakage current and dielectric breakdown behavior in annealed SiO<sub>2</sub> aerogel films, *Appl. Phys. Lett.* 72 (1998) 1391–1393.
- [10] Y. Tanigaki, S. Moribe, T. Itagaki, The Effects of Annealing Ambients on Dielectric Strength of Gate Oxides with Tungsten Polycide Gate, 1988. Proceedings, Fifth International IEEE VLSI Multilevel Interconnection Conference, 1988, pp. 191–197.
- [11] T. Furukawa, A. Yuuki, K. Ono, Recovery of time dependent dielectric breakdown lifetime of thin oxide films by thermal annealing, *J. Appl. Phys.* 82 (1997) 3462–3468.
- [12] L. Kumari, W.Z. Li, C.H. Vannoy, R.M. Leblanc, D.Z. Wang, Synthesis, characterization and optical properties of Mg(OH)<sub>2</sub> micro/nanostructure and its conversion to MgO, *Ceram. Int.* 35 (2009) 3355–3364.
- [13] X.D. Peng, M.A. Barteau, Dehydration of carboxylic acids on the MgO(100) surface, *Catal. Lett.* 7 (1990) 395–402.
- [14] V. Rheinheimer, C. Uhler, J. Liu, S. Ruan, J. Pan, P. Monteiro, XPS study on the stability and transformation of hydrate and carbonate phases within MgO Systems, *Materials* 10 (2017) 75.
- [15] C. Park, J.-G. Zhu, M.T. Monck, Y. Peng, D.E. Laughlin, Annealing effects on structural and transport properties of rf-sputtered CoFeB/MgO/CoFeB magnetic tunnel junctions, *J. Appl. Phys.* 99 (2006), 08A901.
- [16] J. Hayakawa, S. Ikeda, Y.M. Lee, F. Matsukura, H. Ohno, Effect of high annealing temperature on giant tunnel magnetoresistance ratio of CoFeB/MgO/CoFeB magnetic tunnel junctions, *Appl. Phys. Lett.* 89 (2006) 232510.
- [17] S. Ikeda, J. Hayakawa, Y. Ashizawa, Y.M. Lee, K. Miura, H. Hasegawa, M. Tsumoda, F. Matsukura, H. Ohno, Tunnel Magnetoresistance of 604% at 300 K by Suppression of Ta Diffusion in CoFeB/MgO/CoFeB Pseudo spin valves Annealed at High Temperature, 2008.
- [18] L. Ballells, J.I. Beltrán, C. Martínez-Boubeta, Z. Konstantinović, J. Arbiol, B. Martínez, D. T. O. H., M. F., C. J., F. D., Aging of magnetic properties in MgO films, *Appl. Phys. Lett.* 97 (2010) 252503.
- [19] B. Marchon, T. Fitchford, Y. T. Hsia, S. Gangopadhyay, The head disk interface roadmap to an areal density of 10<sup>11</sup>/in<sup>2</sup>, *Adv. Tribol.*, 2013 (2013) 8.
- [20] C. Yao, M. Ismail, A. Hao, S.K. Thattakonda, W. Huang, N. Qin, D. Iso, Annealing atmosphere effect on the resistive switching and magnetic properties of spinel Co<sub>3</sub>O<sub>4</sub> thin films prepared by a sol-gel technique, *RSC Adv.* 9 (2019) 12615–12625.
- [21] P. Liu, T. Kendelewicz, G.E. Brown, G.A. Parks, Reaction of water with MgO(100) surfaces. Part I: Synchrotron X-ray photoemission studies of low-defect surfaces, *Surf. Sci.* 412–413 (1998) 287–314.
- [22] M. Santamaría, F. Di Quarto, S. Zanna, P. Marcus, Initial surface film on magnesium metal: a characterization by X-ray photoelectron spectroscopy (XPS) and photocurrent spectroscopy (PCS), *Electrochim. Acta* 53 (2007) 1314–1324.
- [23] V.S. Birchall, S.D.F. Rocha, M.B. Mansur, V.S.T. Ciomelli, A simplified mechanistic analysis of the hydration of magnesia, *Can. J. Chem. Eng.* 79 (2001) 507–511.
- [24] S.D.F. Rocha, M.B. Mansur, V.S.T. Ciomelli, Kinetics and mechanistic analysis of caustic magnesia hydration, *J. Chem. Technol. Biotechnol.* 79 (2004) 816–821.
- [25] Y. Kato, N. Yamashita, K. Kobayashi, Y. Yoshizawa, Kinetic study of the hydration of magnesium oxide for a chemical heat pump, *Appl. Therm. Eng.* 16 (1996) 853–862.
- [26] D.I. Kushner, M.A. Hickner, Water sorption in electron beam evaporated SiO<sub>2</sub> on QCM crystals and its influence on polymer thin film hydration measurements, *Langmuir* 33 (2017) 5261–5268.
- [27] J.H. Lee, J.H. Eun, S.G. Kim, S.Y. Park, M.J. Lee, H.J. Kim, Hydration behavior of MgO single crystals and thin films, *J. Mater. Res.* 18 (2003) 2895–2903.
- [28] J.A. Mejias, A.J. Berry, K. Reison, D.G. Fraser, The kinetics and mechanism of MgO dissolution, *Chem. Phys. Lett.* 314 (1999) 558–563.

## BIOGRAPHY

Mr. Mongkol Kongtungmon was born on August 24, 1980 in Udon Thani Province, Thailand. He received his bachelor's degree in science (materials science) from Chiangmai University in 2004. After graduation, he has been employed under the position of process engineer by Udon Garment Factory Co., Ltd. He served in position of scientist at Faculty of science, Chiangmai University in 2007. During his working, he continued with his graduate studies in the materials science program, Chiangmai university in 2008 and got master's degree in 2012. After working at Chiangmai University for 8 years, he resigned and started his Ph.D. study in materials engineering program at Suranaree University of Technology in 2016. He interests in the field of materials science including electro ceramics preparation, as well as micro-micro composite ceramics by a solid-state mixed oxide method. His expertise includes characterization of the ceramics phase formation by XRD technique, microstructure by SEM and TEM analysis, electrical and mechanical properties. He also expert on the field of EDS, XPS and XRF quantitative analysis which is an important for trace element analysis. During his study period, he had done two publications with international journal. The 1st publication is in the title of "Dissolution mechanism of MgO thin film shielding layer in tunneling magnetoresistance hard disk drive read head" which published with Materials Today journal. The 2nd publication is in the title of "Effect of annealing atmosphere on hydration behavior of MgO thin film in tunneling magnetoresistance sensor".